WAVE PROPAGATION STUDY USING FINITE ELEMENT ANALYSIS

BY

YUHUI LIU

B.E., Tsinghua University, Beijing, 1999
M.S., University of Illinois at Urbana-Champaign, 2002

THESIS

Submitted in partial fulfillment of the requirements
for the degree of Master of Science in Electrical Engineering
in the Graduate College of the
University of Illinois at Urbana-Champaign, 2005

Urbana, Illinois

To my parents and my brother.

ACKNOWLEDGMENTS

I would like to thank my research adviser, Professor William D. O'Brien, for his patience, encouragement, and guidance throughout my research. I am also very grateful to Dr. Xiangtao Yin for his help with starting this project. Finally, I sincerely thank all the students and members of the Bioacoustics Research Laboratory for always being helpful.

I also acknowledge the United States Air Force Office of Scientific Research (US/AFOSR) (award number F49620-03-1-0188) for the financial support of the project and the National Center for Supercomputing Applications (NCSA) for providing the computer resources.

TABLE OF CONTENTS

LIST OF TABLES

TABLE **PAGE**

LIST OF FIGURES

FIGURE **PAGE**

LIST OF SYMBOLS

Symbols used in theoretical solutions:

a = radius of cylinder or sphere

r = radial distance from the center of cylinder or sphere

c_1 = speed of compressional waves in the scatterer

c_2 = speed of shear waves in the scatterer

c_3 = speed of sound in the fluid surrounding the scatterer

ρ_1 = density of the scatterer

ρ_3 = density of the fluid surrounding the scatterer

$k_1 = \omega/c_1$

$k_2 = \omega/c_2$

$k_3 = \omega/c_3$

E = Young's modulus

σ = Poisson's ratio

$j_m()$ = spherical bessel function of the first kind

$J_m()$ = Bessel function of the first kind

$n_m()$ = spherical bessel function of the second kind

$N_m()$ = Bessel function of the second kind

$h_m()$ = spherical hankel function of the second kind

$H_m()$ = Hankel function of the second kind

p_{inc} = incident plane wave

p_{sca} = scattered wave

P_0 = amplitude of pressure in incident wave

$P_n(cos\theta)$ = Legendre polynomial

t = time

f = frequency

$\omega = 2\pi f$ = angular frequency

$$\varepsilon_m = \begin{cases} 1 & \text{if } m = 0 \\ 2 & \text{if } m > 0 \end{cases}$$

Symbols used in finite-element analysis:

ρ_0 = mean fluid density

k = bulk modulus of fluid

$P = P(x, y, z, t)$, acoustic pressure

f = center frequency of the incident wave (kHz)

T = period of the incident wave

c = sound speed in the medium (m/s)

λ = wavelength in the medium (m)

ρ = material density (kg/m^3)

E = Young's modulus (GPa)

σ = Poisson's ratio

a = cylinder radius / shell outer radius /sphere radius (3D) (m)

d = shell thickness (m)

BOUND = FEA absorbing boundary radius (m)

φ_{inc} = incident angle, the angle between incident wave and +x axis (degree)

X_{inc} = incident wave position (m)

P_{inc} = incident wave pressure amplitude (Pa)

DPW = number of mesh divisions per wavelength

LSS = Load step size

ITS = integration time step size

CHAPTER 1

INTRODUCTION

1.1 Motivations: NIHL, HPDs, and the Failure of HPDs

1.1.1 Noise-induced hearing loss (NIHL)

Hearing is a serial of events in which a special organ inside the inner ear, known as the "cochlea", is stimulated and through the hair cells of the organ of Corti in the cochlea, the sound wave is changed into electrical signals which are carried to the brain by the auditory nerve, where they are understood as sounds. Exposure to harmful sounds causes damage to the sensitive hair cells of the cochlea as well as the hearing nerve and thus causes hearing loss [1], [2]. Noise-induced hearing loss (NIHL) has been an important issue for many decades. The level of damage to hearing is dependent on the intensity of sound, duration of exposure, repeated exposure and individual susceptibility.

There are two typical harmful noises: loud continuous/intermittent noise and loud impact/impulse noise. Continuous noise exposures above 85 dB(A) are considered to be a hazard and above 115 dB(A) are not permissible for any length of time. Table 1.1 lists the permissible noise exposures to different level of continuous and intermittent noise according to the Occupational Safety and Health Administration (OSHA). For impact or impulse noise exposure, such as a gunshot or explosion, the peak sound pressure level must not exceed 140 dB(A).

NIHL is divided into three categories: acoustic trauma, nosie-induced temporary threshold shift (NITTS), and noise-induced permanent threshold shift (NIPTS). Acoustic trauma is usually caused by a single exposure or relatively few exposures at very high sound levels. For example, an explosion may rupture the eardrum, damage the ossicles, and destroy the auditory sensory cells. Usually acoustic trauma results in some degree of permanent hearing loss. NITTS results in an elevation of hearing levels following noise exposure. The temporary threshold shift is reversible and largely disappears 16 to 48 h after exposure. NIPTS results in a nonreversible threshold shift which remains throughout a lifetime. Permanent threshold shifts may

Table 1.1 Permissible continuous and intermittent noise exposures

Sound Pressure Level (SPL)	Permissible Time
80 dB(A)	32 h
85 dB(A)	16 h
90 dB(A)	8 h
95 dB(A)	4 h
100 dB(A)	2 h
105 dB(A)	1 h
110 dB(A)	30 min
115 dB(A)	15 min
120 dB(A)	7.5 min
125 dB(A)	3.8 min
130 dB(A)	1.9 min

result from acoustic trauma or may be produced by the cumulative effect of repeated noise exposures over periods of many years [3].

1.1.2 Hearing protection devices (HPDs)

Hearing protection device (HPD) is a personal safety product that is worn to reduce the harmful auditory or annoying subjective effects of sound ([4], p. 967). Basically, HPDs can be divided into two types: passive and active. Passive protectors give a constant attenuation of the external sound levels, such as ear muffs, ear plugs and helmets, which are the conventional HPDs. These passive HPDs are valued for their relatively high attenuation (10 to 45 dB) of the external sound levels over a broad frequency range. However, the conventional passive HPDs are ineffective at low frequencies and against impact/impulse noise. Active HPDs are modified conventional HPDs with incorporating electronics system. There are two types of active HPDs: active sound transmission HPDs and active noise reduction (ANR) HPDs. Active sound transmission HPDs offer a viable alternative for use in intermittent noises, especially those with impulse-type or short-duration on-segments; however, the effectivity of these HPDs can be compromised in continuous, high-level noise. ANR HPDs, which are based on the principle of destructive interference

to cancel noise, are most effective against repetitive or continuous noises that are relatively invariant in spectrum or level. They are effective and limited to the reduction of low-frequency noise below about 1 kHz, with maximum attenuation of 20 - 25 dB occurring below 300 Hz [3–6].

1.1.3 Failure of the current HPDs

It has been reported that when individuals are exposed to severe noise environments, such as that generated by aircraft engines and military weapons that approach and even exceed a sound pressure level (SPL) of 150 dB, even if they wear passive hearing protection equipment, they may be subject to hearing damage. Furthermore, NIHL at low frequencies (125 Hz and less) are even more challenging.

For the normal hearing process, air-borne acoustic signals enter the human ear through the auditory canal, and arrive at the organ of Corti where they are transduced. The failure of conventional passive protection equipment thus brings up a reasonable question: besides the normal acoustic propagation path through the auditory canal to the organ of Corti, are there any alternative acoustic propagation paths existing to the organ of Corti?

Therefore, in order to improve the current hearing protections, there is a desire to understand the human hearing process, specifically the propagation pathways of the sound to reach the cochlea. The overall goal of this research is to develop a computational finite-element model of a detailed human head, as well as its torso and arms, if necessary, based on real human data, and conduct acoustic finite-element analysis (FEA) on the computational model to track an air-borne incident acoustic wave propagated around, into, and in the human head. This acoustic propagation model will serve as a valuable tool to understand the acoustic wave propagation around, into, and inside the human head, and specifically to identify different pathways that the acoustic wave energy has taken to reach the cochlea, and furthermore to evaluate these pathways in terms of the acoustic pressure level that reach the cochlea through each pathway.

1.2 Background: Human Ear and the Pathways to the Cochlea

1.2.1 Human ear

The human ear (Figure 1.1 [1]) consists of the outer ear (pinna and auditory canal), the air-filled middle ear (three bones: malleus, incus, and stapes), and the liquid-filled inner ear (labyrinth). The eardrum (tympanic membrane) separates the outer and middle ears. Acoustic signals entering the auditory canal perturb the eardrum connected to the middle ear's malleus. The malleus communicates to the stapes through the incus. The stapes is connected to the oval window membrane structure that separates the middle ear from the inner ear. The three middle ear bones (ossicles) work in concert to impedance transform the airborne acoustic signal from the outer ear to the liquid-filled inner ear. The inner ear consists of the vestibule, the semicircular canals, and the cochlea. The vestibule connects with the middle ear through two openings, the oval window and the round window. Both of these windows are sealed to prevent the escape of the liquid filling the inner ear; the oval window by the stapes and its support, and the latter by a thin membrane. With these two exceptions, the entire inner ear is surrounded by bone.

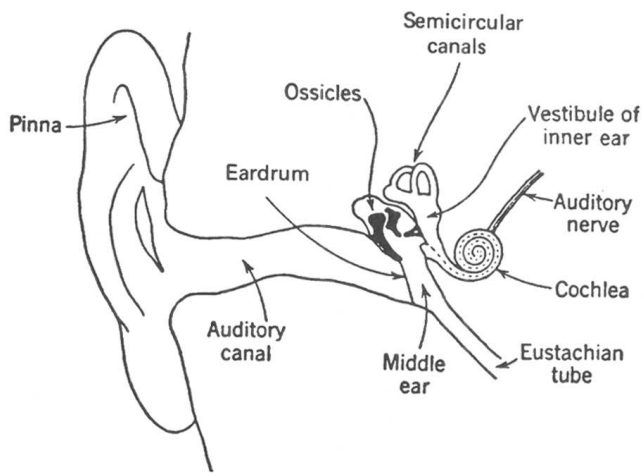

Figure 1.1 Sketch of the ear [1].

The cochlea is a tube of roughly circular cross section, wound in the shape of a snail shell, divided into three chambers (scala vestibuli, scala media, scala tympani). Figure 1.2 shows a cross section of one of the turns of the cochlea [1]. The bony

ledge projects from the central portion of the shell-like structure into the liquid-filled tube and carries the auditory nerve. At the termination of the bony ledge the nerve fibers enter the basilar membrane. Attached to the top of the basilar membrane is the organ of Corti that contains four rows of hair cells. The whole cochlea is located in a cavity in the petrous temporal bone of the skull.

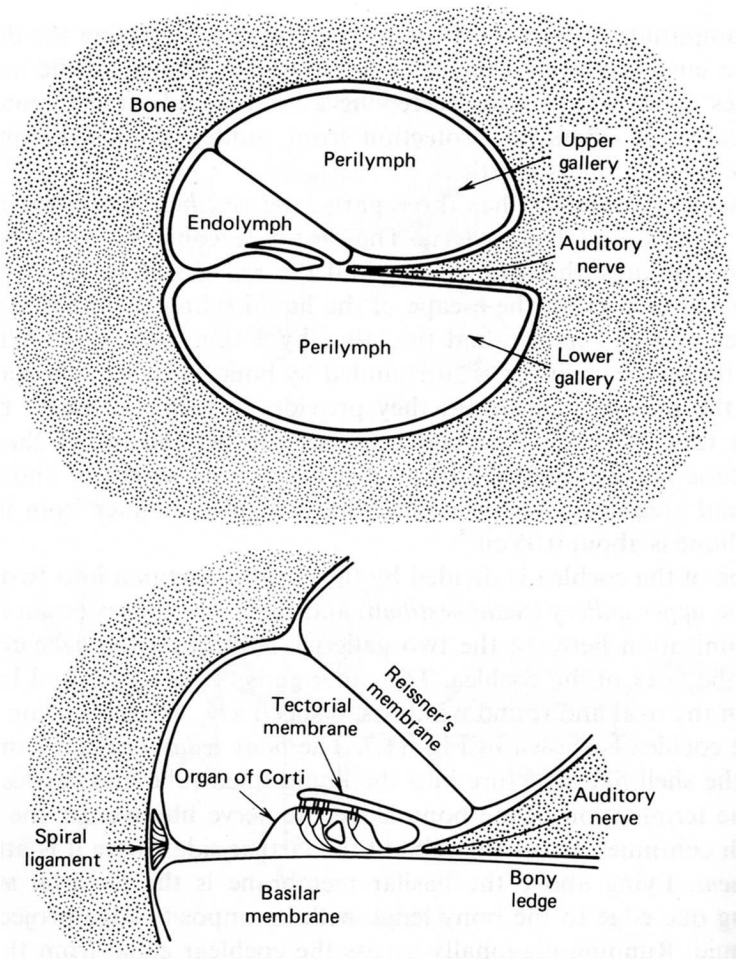

Figure 1.2 Cross section of the cochlea duct [1].

1.2.2 The conduction pathways to the cochlea

Normal air conduction (AC) pathway. The air conduction pathway is a well-studied and admitted major pathway to the cochlea. For the normal hearing process, air-borne acoustic signals enter through the ear canal to the eardrum. The eardrum

vibrates and causes the three small bones of the middle ear to vibrate. The acoustic stimulation results from movement of the stapes footplate into and out of the scala vestibuli chamber at the oval window. A compressive wave travels through two and one-half turns of the scala vestibuli of the cochlea to its apex. The compressive wave is then reversed by the round window membrane and energy is sent back through the two and one-half turns of the scala tympani. The action of the inward movement of the stapes footplate moves the pressure-release round window membrane outward, a 180° phase difference between the oval and round windows. The traveling compression wave sends a corresponding wave motion along the basilar membrane which lies in the scala media. These motions flex the hair cells of the organ of Corti, thereby exciting the nerve endings attached to the hair cells into producing electrical impulses which are carried to the brain, where they are understood as sounds [1, 7].

Bone conduction (BC) pathways. Other than the normal air conduction pathway, researchers also believed that the bone conduction pathways also contributed to the cochlea response. The bone conduction pathways are largely unknown although a few bone conduction pathways have been proposed. It is proposed that when the skull is subjected to vibrations caused by the acoustic field surrounding the head, there are two modes of bone conduction: inertial and compressional bone conduction. In the inertial mode of bone conduction, a relative motion is set up (1) between the temporal bone and the ossicular chain, and (2) between the cochlear shell and the cochlear fluid content. The former results in the displacement of the stapes which leads to cochlear stimulation in much the same way as that by air-conducted sound, and the latter causes the cochlear fluid displacement which induces the displacement of the basilar membrane, exciting the cochlea. In the compressional mode of bone conduction, the skull vibrations are propagated to the temporal bone and cause distortion of the cochlear shell and thus cause fluid displacements in and out of the cochlear windows, exciting the cochlea with the basilar membrane displacement [8–11]. It was stated that inertial effects dominate low-frequency bone conduction hearing and compressional effects dominate high-frequency bone conduction hearing [8].

In addition to these osseous mechanism above, recently some research work showed evidence that there is another possible conduction pathway for cochlear excitation that is non-osseous. The skull bone vibrations are hypothesized to induce audio-frequency sound pressures in the brain and cerebrospinal fluid, which are

conducted to the fluids of inner ear through fluid channels (e.g., vestibular and cochlear aqueducts, perineural and perivascular channels) [12–14].

There are also other various possible secondary pathways of bone conduction. Some of them are [9], [10]:

1. The vibrations of the skull may radiate sound into the surrounding air, and some of this sound may find its way into the external ear canal. Alternatively, the vibrations may pass to the walls of the meatus and here produce aerial waves. In either case the sound thereafter acts on the drum membrane like any other aerial stimulus, named the osseotympanic route.

2. The vibrations may pass to the walls of the tympanic cavity and set up waves in its contained air. These waves act on the tympanic membrane more effectively than those waves that enter the round window directly in the normal ear.

3. The movements communicated to the walls of the external meatus and tympanic cavity may move the tympanic membrane through its annulus or move the ossicles, especially the incus, through their suspensions.

4. Another form of inertia stimulation is based on the idea that as the skull moves, the lower jaw remains relatively stationary and effectively produces an alternating compression of the external auditory meatus.

These secondary pathways are either not evaluated or lack quantitative support, and are considered to be of minor importance. In a word, the mechanisms of bone conduction are quite complex and still need further study.

The final cochlea response. Although the stimulation mode of bone conducted stimulation can be very different from air conducted stimulation, the final inner ear response in bone conduction is initiated by the same transduction mechanism as in air conduction [10], [15], [16]. Thus, the final stimulus transferred to the cochlea is a vectorial integration of all the conduction pathways, including the air conduction pathway, different bone conduction pathways and any other potential alternative pathways. Its excitation will depend on the vectorial summation of all pathways, depending on their relative magnitudes and phases. It is possible that each of these pathways is more effective at different frequencies [9], [10], [13].

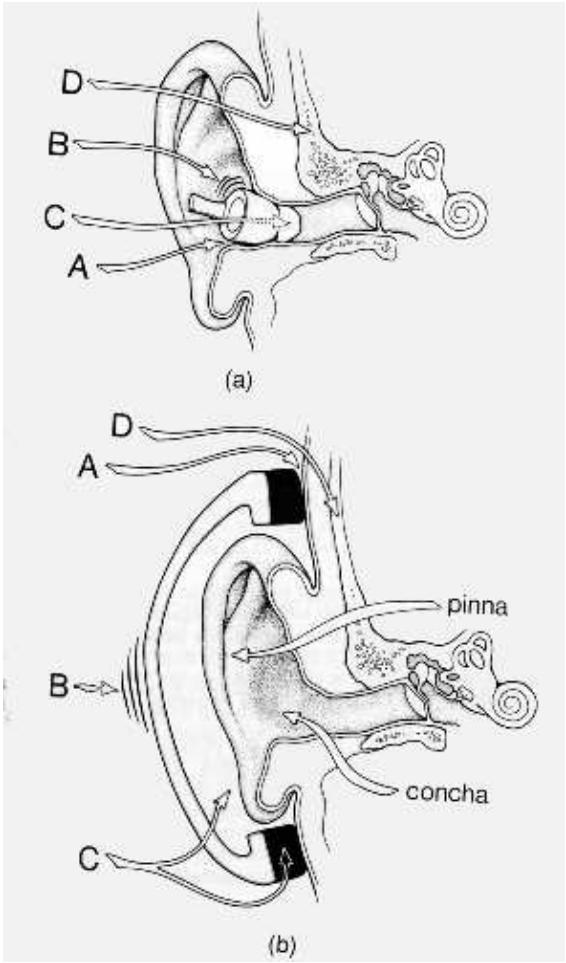

Figure 1.3 The four paths by which sound reaches the inner ear when hearing protection devices ((a) earplug; (b) earmuff) are worn [3].

Sound transmission to the occluded ear with HPDs. When the ear canal of an individual is blocked by a HPD, the AC and BC pathways discussed in the previous sections are modified. Sound may reach the inner ear along the four distinct pathways as shown in Figure 1.3 [3]:

1. Air leaks (A): For maximum protection, the earplugs must make a tight seal with the canal and the earmuffs must take a tight seal with the side of the head. If the inserts are not accurately fit the contours of the ear canal and earmuff cushions are not accurately fit the areas surrounding the external ear, air leaks happen. Air leaks can typically reduce the attenuation by 5-15 dB over a broad

frequency range, varying with the size of the air leak and with frequency. The primary reduction is at low frequencies.

2. Vibration of the HPD (B): Due to the flexibility of the ear canal flesh, ear plugs can vibrate in a pistonlike manner within the ear canal. This limits their low frequency attenuation. The earcups of earmuffs can vibrate against the head as a mass/spring system, with an effective stiffness governed by the flexibility of the muff cushion and the flesh surrounding the ear, as well as the air volume entrapped under the cup. For ear muffs, premolded inserts and foam inserts these limits of attenuation at 125 Hz are approximately 25 dB, 30 dB and 40 dB, respectively.

3. Transmission through the material of the HPD (C): Sound is transmitted through the HPD materials. This reduction in attenuation is usually more significant for earmuffs than earplugs because of the much larger surface areas involved with earmuffs, which normally is significant only at frequencies above 1000 Hz.

4. Bone conduction (D): HPDs are designed to effectively block sound by air conduction pathways, not the bone conduction pathways. Bone conduction may become a significant factor for the protected ear

There are several possible reasons why conventional HPDs fail under severe noisy circumstances and for certain frequencies: (1) the noise exposure may exceed the protection offered by HPDs, either because of insufficient attenuation of HPDs or the reduction in attenuation due to path 1, 2, and 3 described above; (2) the bone conduction pathways are enhanced relative to the unoccluded ear at frequencies below 2 kHz, which is known as "occlusion effect" [3], [7], [17]; and (3) other alternative pathways may become a significant factor for the protected ear.

1.3 Approach: Acoustic Finite-Element Analysis (FEA) on Human Head Model

1.3.1 Pros and cons of finite-element analysis (FEA)

The human head is an inhomogeneous scatterer (bone, fat, soft tissues within the skull) with multiple openings (ears, eyes, nose, mouth), irregular geometry, and

various coatings (skin layer, hairs). The analysis of acoustic wave propagation around and in the human head requires a flexible analysis tool capable of representing the complex geometries with propagation speed and density variations as well as frequency-dependent attenuation mechanisms. As a result, over the past decades many computer-based, numerical formulations have been developed in an effort to extend the analytical wave equations to more complex modeling configurations both in the time and frequency domains.

Among the many integral and differential formulations, the finite-element method (FEM) has proved to be more versatile in terms of accounting for density variations, even within the scattering centers, as well as modeling anisotropic and absorption phenomena. Therefore, the complicated geometry of the human head can be modeled in detail in FEA. FEA is capable of calculating strains, stresses, deformations in a solid structure, and pressure and particle velocity in a fluid. In FEA, the computational domain is divided into discrete volumes, called *elements*. Each element is assigned a size and a constitutive behavior that describe the material acoustic properties to which the element belongs [18].

However, FEA suffers from the inability to deal with open field problems because it does not implicitly impose the radiation boundary condition. One of the solutions is to use an artificial outer boundary and an absorbing boundary condition (ABC) is applied to this contour such that the scattered wave appears only outgoing through the boundary and artificial reflections due to the domain truncation are minimized [19].

Furthermore, FEA is preferred over experiments on manikins or humans for a number of reasons. First and foremost, with FEA it is possible to see responses that are difficult or impossible to characterize experimentally. With FEA it is expected that phenomena will be recognized that might otherwise be missed, and that questions will be discovered that might not have been with experiments alone. "What-if" types of analysis can be done readily, and the approach and the study focus can be further refined as more is learned about the problem from the simulations. If experiments are appropriate in future work, then FEA will help design the experiments, either on manikins or human subjects.

1.3.2 Acoustic finite-element analysis in ANSYS

The acoustic analysis available in ANSYS (ANSYS, Inc., Canonsburg, PA), an industry standard used for FEA, can model the fluid-solid structures and study the pressure distribution in the fluid and the vibration of structures at different frequencies. With a well-built FEA model and a properly validated code, it is possible to track an air-borne incident acoustic wave to the cochlea, to identify different propagation pathways, and furthermore to evaluate these pathways in terms of the acoustic pressure levels that reach the cochlea through each pathway. All the studies in this work are conducted using the ANSYS acoustic FEA module.

1.4 Organization of This Thesis

This thesis presents the research accomplished at the Bioacoustics Research Laboratory located at the University of Illinois at Urbana-Champaign to develop computational acoustic wave propagation model of the human head. This work is supported by US/AFOSR (award number F49620-03-1-0188).

Chapter 2 describes the finite-element formulas used in ANSYS acoustic analysis and some basic theoretical solutions of sound pressure distribution for sound scattered by simple geometries such as the 2D cylinder and 3D sphere. Chapter 3 describes the finite-element harmonic analysis on some simple models such as the 2D rigid cylinder, 2D rigid and elastic shell cylinder, 3D rigid sphere, and 3D elastic sphere. Chapter 4 describes the finite-element transient analysis on simple geometry models such as the 2D cylinder and 3D sphere. Chapter 5 describes the FEA conducted on a simplified human head model developed with a complete digital image database of a human head. Both 2D and 3D scenarios are studied. Chapter 6 introduces the methodologies used to reconstruct wavefronts and trace the acoustic propagation path based on the computed results in the finite-element analysis. Finally, the summary of what has been accomplished and suggestions for future work are presented in Chapter 7.

CHAPTER 2

THEORETICAL FUNDAMENTALS

This chapter describes the finite-element formulation of the wave equation used in ANSYS and the theoretical solutions for the scattered and transmitted fields by simple geometries such as the 2D cylinder and 3D sphere.

2.1 Finite-Element Formulas in ANSYS

In acoustical fluid-structure interaction problems, both the acoustic wave equation and the structural dynamics equation need to be coupled to each other.

In deriving the discretized acoustic wave equation, there are some necessary assumptions [1], [20]:

- The fluid is compressible, but only relatively small pressure changes with respect to the mean pressure are allowed.
- The fluid is inviscid (no viscous dissipation).
- There is no mean flow of the fluid.
- The mean density and mean equilibrium pressure are uniform throughout the fluid.
- No gyroscopic or Coriolis nonlinearities are included in a structural analysis

The acoustic wave equation is given by

$$\frac{1}{c^2}\frac{\partial^2 P}{\partial t^2} - \nabla^2 P = 0 \tag{2.1}$$

where

c = speed of sound in fluid medium ($\sqrt{\frac{k}{\rho_0}}$)

ρ_0 = mean fluid density

k = bulk modulus of fluid

$P = P(x, y, z, t)$, acoustic pressure

$t =$ time

The discretized wave equation is written in finite-element matrix notation by

$$[M_e^P]\{\ddot{P}_e\} + [K_e^P]\{P_e\} = 0 \tag{2.2}$$

where

$[M_e^P] = \frac{1}{c^2}\int_{vol}\{N\}\{N\}^T d(vol) =$ fluid mass matrix

$[K_e^P] = \int_{vol}\{B\}^T\{B\}d(vol) =$ fluid stiffness matrix

$[B] = \{L\}\{N\}^T$

$\{N\} =$ element shape function for pressure

$\{L\} = \nabla(), \{L\} = \nabla \cdot ()$

$\{P_e\} =$ nodal pressure vector

$vol =$ volume of domain

In the fluid-structure interaction problem, a natural boundary condition along the interface needs to be included. For the simplifying assumptions made, the fluid momentum equations yield the following relationship between the pressure gradient of the fluid and the normal acceleration of the structure at the fluid-structure interface:

$$\{n\} \cdot \{\nabla P\} = -\rho_0\{n\} \cdot \frac{\partial^2\{u\}}{\partial t^2} \tag{2.3}$$

where

$\{u\} =$ displacement vector of the structure at the interface

$\{n\} =$ unit normal at the fluid boundary

Including the fluid-structure interface condition to the wave equation and writing it in finite-element matrix notation, Equation (2.2) becomes

$$[M_e^P]\{\ddot{P}_e\} + [K_e^P]\{P_e\} + \rho_0[R_e]^T\{\ddot{u}_e\} = 0 \tag{2.4}$$

where

$\rho_0[R_e] = \rho_0\int_S\{N\}\{N\}^T\{N'\}^T dS =$ fluid-structure coupling mass matrix

$\{N'\} =$ element shape functions to discretized the displacement components u_x, u_y and u_z (obtained from the structural element)

$\{u_e\} = \{u_{xe}\}, \{u_{ye}\}, \{u_{ze}\} =$ nodal displacement component vectors

$S =$ surface where the derivative of pressure normal to the surface is applied (a natural boundary condition)

In order to account for the dissipation of energy due to damping, if any, present at the fluid boundary, a dissipation term is added to Equation (2.4):

$$[M_e^P]\{\ddot{P}_e\} + [C_e^P]\{\dot{P}_e\} + [K_e^P]\{P_e\} + \rho_0[R_e]^T\{\ddot{u}_e\} = 0 \tag{2.5}$$

where

$[C_e^P] = \frac{\beta}{c}\int_S\{N\}\{N^T\}d(S)$ = fluid damping matrix

β = boundary absorption coefficient

$\{\dot{P}_e\} = \{\frac{\partial P_e}{\partial t}\}$

In order to account for the fluid-structure interaction, the fluid pressure load acting at the fluid-structure interface, F_e^{pr}, is added to the structural dynamic equation and gives

$$[M_e]\{\ddot{u}_e\} + [C_e]\{\dot{u}_e\} + [K_e]\{u_e\} = \{F_e\} + \{F_e^{pr}\} \tag{2.6}$$

where

$\{F_e^{pr}\} = [R_e]\{P_e\}$ = the fluid pressure load vector at the interface.

Equations (2.5) and (2.6) describe the finite-element discretized equations for the fluid-structure interaction problem and are written in assembled form as

$$\begin{bmatrix} [M_e] & [0] \\ [M^{fs}] & [M_e^P] \end{bmatrix} \begin{Bmatrix} \{\ddot{u}_e\} \\ \{\ddot{P}_e\} \end{Bmatrix} + \begin{bmatrix} [C_e] & [0] \\ [0] & [C_e^P] \end{bmatrix} \begin{Bmatrix} \{\dot{u}_e\} \\ \{\dot{P}_e\} \end{Bmatrix} + \begin{bmatrix} [K_e] & [K^{fs}] \\ [0] & [K_e^P] \end{bmatrix} \begin{Bmatrix} \{u_e\} \\ \{P_e\} \end{Bmatrix} = \begin{Bmatrix} \{F_e\} \\ \{0\} \end{Bmatrix} \tag{2.7}$$

where

$[M^{fs}] = \rho_0[R_e]^T$

$[K^{fs}] = -[R_e]$

2.2 Theoretical Solutions for the Acoustic Sound Field around the Cylinder and Sphere Scatterer

This section summarizes the theoretical solutions for calculating the sound field around the solid cylinder and sphere scatterers based on [21–24].

2.2.1 Solid cylinder scatterers

The following equations compute the scattering, by a solid cylinder of radius a, of a plane wave traveling in a direction perpendicular to the cylinder's axis (Figure 2.1). The cylinder is made of solid material which support shear waves in addition to compressional waves [22], [23].

$$p_{inc} = P_0 e^{ik_3(r\cos\theta - ct)} = P_0 \sum_{m=0}^{\infty} \varepsilon_m i^m \cos(m\theta) J_m(k_3 r)] e^{-i\omega t} \tag{2.8}$$

$$p_{sca} = \sum_{m=0}^{\infty} A_m \cos(m\theta)[J_m(k_3 r) + iN_m(k_3 r)] e^{-i\omega t} \tag{2.9}$$

$$A_m = -\varepsilon_m P_0 i^{m+1} e^{-i\gamma_m} \sin(\gamma_m) \tag{2.10}$$

where γ_m, the phase-shift angle of the nth scattered wave, is defined by

$$\tan\gamma_m = \tan\delta_m(k_3 a)\frac{\tan\Phi_m + \tan\alpha_m(k_3 a)}{\tan\Phi_m + \tan\beta_m(k_3 a)} \tag{2.11}$$

The intermediate scattering phase angles are defined by

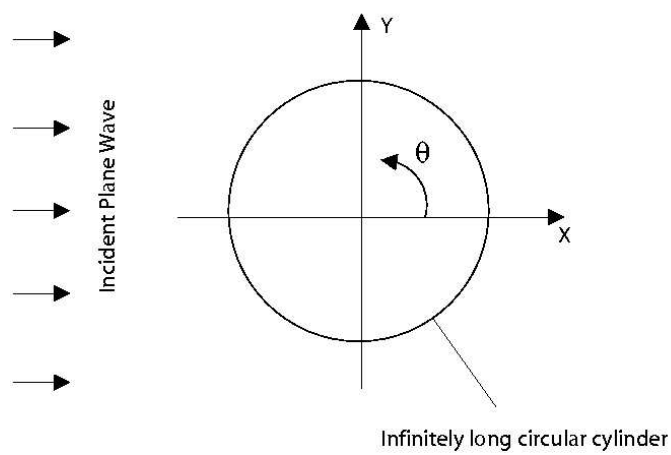

Figure 2.1 Cylindrical coordinate system.

$$\tan(\delta_m(ka)) = \frac{-J_m(ka)}{N_m(ka)} \tag{2.12}$$

$$\tan(\alpha_m(ka)) = ka\frac{-J_m^{'}(ka)}{J_m(ka)} \tag{2.13}$$

$$\tan(\beta_m(ka)) = ka\frac{-N_m^{'}(ka)}{N_m(ka)} \tag{2.14}$$

The angle Φ_m, which is a measure of the boundary impedance at the surface of the scatterer, is given by

$$\tan(\Phi_m) = (-\rho_3/\rho_1)\tan(\xi_m(k_1a,\sigma)) \tag{2.15}$$

where

$$\tan(\xi_m(k_1a,\sigma)) = \frac{-(k_2a)^2}{2}\frac{\frac{k_1aJ_m^{'}(k_1a)}{k_1aJ_m^{'}(k_1a)-J_m(k_1a)} - \frac{2m^2J_m(k_2a)}{m^2J_m(k_2a)-k_2aJ_m^{'}(k_2a)+(k_2a)^2J_m^{''}(k_2a)}}{\frac{\frac{\sigma}{1-2\sigma}(k_1a)^2[J_m(k_1a)-J_m^{''}(k_1a)]}{k_1aJ_m^{'}(k_1a)-J_m(k_1a)} + \frac{2m^2[k_2aJ_m^{'}(k_2a)-J_m(k_2a)]}{m^2J_m(k_2a)-k_2aJ_m^{'}(k_2a)+(k_2a)^2J_m^{''}(k_2a)}} \tag{2.16}$$

Hence, the total pressure at the surface of the cylinder at an angle θ from the x-axis is simply the sum of the incident wave and the scattered wave:

$$p_{total} = p_{inc} + p_{sca} \tag{2.17}$$

For rigid, immovable cylinders, the phase-shift angle γ_m is simplified as [22]

$$\tan\gamma_0 = -\frac{J_1(ka)}{N_1(ka)}, \tan\gamma_m = \frac{J_{m-1}(ka) - J_{m+1}(ka)}{N_{m+1}(ka) - N_{m-1}(ka)} \tag{2.18}$$

which is the same as the solution by Morse [22]. In this case the total pressure at the surface of the cylinder at an angle θ is [22]

$$p_{total} = p_{inc} + p_{sca} = \frac{4P_0}{\pi ka}e^{-i\omega t}\sum_{m=0}^{\infty}\frac{\cos(m\theta)}{E_m}e^{i[-\gamma_m+(\pi m/2)]} \tag{2.19}$$

where E_m is the radiation amplitude for a cylinder, defined as:

$$\begin{array}{lll} E_0 \approx \sqrt{\frac{8}{2\pi ka}} & E_{m>0} \approx \sqrt{\frac{2}{\pi ka}} & ka \gg m+1/2 \\ E_0 \approx \frac{4}{\pi ka} & E_{m>0} \approx \frac{m!}{2\pi}\left(\frac{2}{ka}\right)^{m+1} & ka \ll m+1/2 \end{array} \tag{2.20}$$

2.2.2 Scattering by solid spheres

This section gives the equations used to compute the scattering of an incident plane wave by a solid sphere of radius a (Figure 2.2). The sphere is made of solid materials which support shear waves in addition to compressional waves [22], [23].

The expression for an incident plane wave traveling along the $+z$ axis is

$$p_{inc} = P_0 e^{ik_3(r\cos\theta - ct)} = P_0 \sum_{m=0}^{\infty} (2m+1) i^m P_m(\cos\theta) j_m(k_3 r) e^{-i\omega t} \tag{2.21}$$

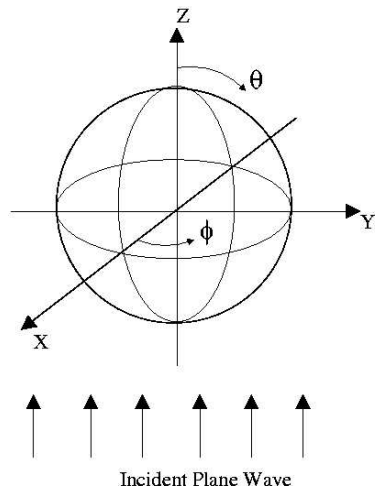

Figure 2.2 Spherical coordinate system.

The expression for the wave scattered from the sphere of radius a centered at the polar origin is

$$p_{sca} = -P_0 \sum_{m=0}^{\infty} (2m+1) i^m e^{-i\gamma_m} \sin\delta_m P_m(\cos\theta)[j_m(k_3 r) + i n_m(k_3 r)] e^{-i\omega t} \tag{2.22}$$

where γ_m, the phase-shift angle of the nth scattered wave, is defined by

$$\tan\gamma_m = \tan\delta_m(k_3 a) \frac{\tan\Phi_m + \tan\alpha_m(k_3 a)}{\tan\Phi_m + \tan\beta_m(k_3 a)} \tag{2.23}$$

The intermediate scattering phase-angles are defined by

$$\tan(\delta_m(ka)) = \frac{-j_m(ka)}{j_m(ka)} \tag{2.24}$$

$$\tan(\alpha_m(ka)) = ka\frac{-j_m^{'}(ka)}{j_m(ka)} \tag{2.25}$$

$$\tan(\beta_m(ka)) = ka\frac{-n_m^{'}(ka)}{n_m(ka)} \tag{2.26}$$

The angle Φ_m, which is a measure of the boundary impedance at the surface of the scatterer, is given by

$$\tan(\Phi_m) = (-\rho_3/\rho_1)\tan(\xi_m(k_1a,\sigma) \tag{2.27}$$

where

$$\tan(\xi_m(k_1a,\sigma)) = \frac{-(k_2a)^2}{2}\frac{\frac{k_1aj_m^{'}(k_1a)}{k_1aj_m^{'}(k_1a)-j_m(k_1a)} - \frac{2(m^2+m)j_m(k_2a)}{(m^2+m-2)j_m(k_2a)+(k_2a)^2j_m^{''}(k_2a)}}{\frac{\frac{\sigma}{1-2\sigma}(k_1a)^2[j_m(k_1a)-j_m^{''}(k_1a)]}{k_1aj_m^{'}(k_1a)-j_m(k_1a)} + \frac{2(m^2+m)[k_2aj_m^{'}(k_2a)-j_m(k_2a)]}{(m^2+m-2)j_m(k_2a)+(k_2a)^2j_m^{''}(k_2a)}} \tag{2.28}$$

Hence, the total pressure at the surface of the cylinder at an angle θ from the x-axis is simply the sum of the incident wave and the scattered wave:

$$p_{total} = p_{inc} + p_{sca} \tag{2.29}$$

The total pressure at a point on the sphere with an angle θ from the polar axis turns out to be [22]

$$p_a = P_0\sum_{m=0}^{\infty}(2m+1))i^mP_m(\cos\theta)[j_m(k_3r) - \frac{1}{2}(1+R_m)h_m(k_3r)] \tag{2.30}$$

where

R_m = reflection coefficient, defined by $1+R_m = 2\frac{j_m^{'}(k_3a)+i\beta_mj_m(k_3a)}{h_m^{'}(k_3a)+i\beta_mh_m(k_3a)}$

β_m = effective admittance, defined by $\beta_m = i\frac{\rho_3c_3}{\rho_1c_1}\left[\frac{j_m^{'}(k_1a)}{j_m(k_1a)}\right]$

For rigid, immovable spheres with size small compared with the wavelength, a simpler solution for the total pressure at an angle θ from the polar axis turns out to be [22]

$$\begin{aligned} p_a &= (p_{inc}+p_{sca})_{r=a} \\ &= P_0(k_3a)^{-2}\textstyle\sum_{m+0}^{\infty}\frac{2m+1}{B_m}P_m(\cos\theta)e^{-i(\gamma_m-\pi m/2-\omega t)} \\ &\approx (1+\tfrac{3}{2}ik_3a\cos\theta)P_0e^{-i\omega t} \qquad k_3a \ll 1 \end{aligned} \tag{2.31}$$

CHAPTER 3

HARMONIC ACOUSTIC FINITE-ELEMENT ANALYSIS ON SIMPLE GEOMETRY MODELS

In this chapter and in Chapter 4, the feasibility of acoustic FEA in ANSYS is evaluated on some well-understood geometry models such as spheres and 2D solid and shell cylinders in both frequency-domain and time-domain, i.e., harmonic analysis and transient analysis.

Harmonic analysis requires fewer computer resources and has sufficient theoretical solutions to compare with the computational results. Thus, it serves as a good start to help develop the code properly to carry out finite-element analysis in ANSYS. In this chapter, the general basic procedure for ANSYS acoustic analysis is described in detail. Then harmonic analysis on various simple geometry models is conducted. The computation results are compared with the theoretical solutions, and good agreement is obtained.

3.1 Basic Procedure for an Acoustic Analysis in ANSYS

In general, an ANSYS acoustic analysis consists of three main steps:

1. Build the model.
2. Apply loads and obtain the solution.
3. Review the results.

3.1.1 Build the model

The ultimate purpose of an FEA is to recreate mathematically the behavior of an actual physical system. In other words, the analysis must be an accurate mathematical model of a physical prototype. This model comprises all the nodes, elements, material properties, real constants, boundary conditions, and other features used to represent the physical system. Thus, model generation in this discussion will

mean the process of defining the geometric configuration of the model's nodes and elements. There are three approaches for model generation:

1. Creating a geometry model within ANSYS: Describe the geometric boundaries of the model, establish controls over the size and desired shape of the elements, and then instruct the ANSYS program to generate all the nodes and elements automatically.

2. Using direct generation: Determine the location of every node and the size, shape, and connectivity of every element prior to defining these entities in the ANSYS model.

3. Importing a model created in a computer-aided design (CAD) system.

Solid modeling is generally more appropriate for large or complex models, especially 3D models of solid volumes. As a complex model like human head is involved, solid modeling is chosen as the main approach for model generation in this work.

Model generation is a very important step for conducting an analysis. A number of decisions need to be made to determine how to mathematically simulate the physical system: What are the objectives of the analysis? How much detail will be included in the model? What kinds of elements should be use? How dense should the finite-element mesh be? In general, model generation attempts to balance computational expense (CPU time, etc.) against precision and accuracy of results. A good FEA model should be able not only to mathematically represent the physical system as accurate as possible but also to avoid unnecessary computational cost as much as possible. The generation of different FEA models in various case studies will be described in detail throughout the thesis.

3.1.2 Apply loads and obtain the solution

The main goal of an FEA is to examine how a structure or component responds to certain loading conditions. Therefore, specifying the proper loading conditions is also a key step in the analysis. The loading conditions in this discussion not only include the applied external load, such as a harmonic (sinusoidal varying) load for harmonic analysis and a time-dependent (not necessarily sinusoidal varying) load for transient analysis, but also include certain boundary conditions, such as zero degrees

of freedom (DOFs) constraints for rigid solid components. Here the term *rigid* is defined as immovable.

In the solution phase of the analysis, the computer takes over and solves the simultaneous set of equations that the finite-element method generates. Several methods of solving the system of simultaneous equations are available in the ANSYS program: sparse direct solver, frontal direct solver, Jacobi conjugate gradient (JCG) solver, incomplete Cholesky conjugate gradient (ICCG) solver, and preconditioned conjugate gradient (PCG) solver. JCG, ICCG, and PCG solvers are iterative solvers. Direct solvers (such as the frontal and sparse direct solvers) provide robustness and produce very accurate solutions. Frontal solver is for smaller model size (DOFs $\leq$ 50 000) while sparse solver is for larger model size (10 000 $\leq$ DOFs $\leq$ 500 000 DOFs). A JCG solver (iterative solver) is preferred for single-field problems (thermal, magnetics, acoustics, and multi-physics) with model size of 50 000 to 1 000 000+ DOFs. An ICCG solver (iterative solver) is used more in multiphysics applications and handles models that are harder to converge in other iterative solvers (nearly indefinite matrices). It can handle models of 50 000 to 1 000 000+ DOFs. A PCG solver (iterative solver) is especially well suited for large models with solid elements and recommended for structural analysis.

The problem in the present research is a coupled-field acoustic problem. There are no explicit recommendations in ANSYS manual regarding choosing the solver for this type of problem. Based on a review of the literature [18], [25], two solvers, sparse solver and ICCG solver, are possibly suitable for the present research. Both solvers demand large memory and can handle unsymmetrical matrices. A sparse solver is more preferred because it is more robust and accurate, especially when iterative solvers are slow to converge for ill-conditioned matrices, such as poorly shaped elements which surly exist in our model. Furthermore, both solvers are checked using the 2D rigid cylinder model. Sparse solver gives more accurate results when comparing with the theoretical solution. Therefore, sparse solver is used in all the analysis in this work.

3.1.3 Review the results

The results include nodal DOF values, which form the primary solution, and derived values, which form the element solution. In harmonic acoustic analysis the pressure distribution in the fluid/structure model is calculated due to a harmonic

(sinusoidal varying) load while in transient acoustic analysis the pressure distribution in the fluid/structure model is calculated at each time step due to a time-dependent load (not necessarily sinusoidal varying).

3.2 Two-Dimensional Rigid Cylinder

In this section, acoustic analysis is conducted on a rigid solid circular cylinder under the incidence of an air-borne plane wave. The model generation is described in detail as a prototype example for all the case studies on simple geometries.

3.2.1 Model development

Figure 3.1 shows the discretized FEA model for 2D cylinder developed in ANSYS.

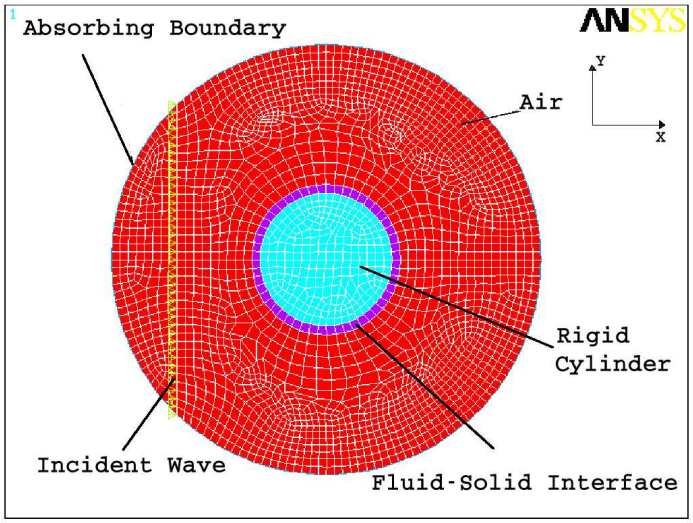

Figure 3.1 FEA model for 2D rigid circular cylinder.

Geometry description. The complete computational domain is a circular region filled with air. The target cylinder is submerged in air at the center of the computational domain which is recommended by ANSYS. A second-order absorbing boundary condition is applied on the domain boundary to simulate the infinite space. The circular shape for the computation domain is mandatory in ANSYS for applying the absorbing boundary condition. The incident acoustic plane wave is excited at a

plane parallel to the cylinder's axis and travels in a direction perpendicular to the cylinder's axis (Figure 3.1).

One question that arises in this step is where to put the absorbing boundary and the incident wave. ANSYS recommends that the enclosed circular boundary is placed at a distance of at least 0.2λ from the boundary of any structure submerged in the fluid, where $\lambda = c/f$ is the dominant wavelength of the pressure wave. In this specific case, the propagation of a plane wave is simulated. Generally, the larger the domain is, the closer to the plane wave condition is, and the more accurate the solution will be. However, larger computation domain also means larger meshed model and thus higher computational cost. Therefore, the only way to determine the appropriate model is to perform analysis using different parameters and compare the results with known accurate analytical solutions. The models that give more accurate results are preferred over the models that give less accurate results. For the models of the same accuracy, smaller size model is preferred over the larger size model in order to minimizing the computation cost.

Mesh generation. Mesh generation is also called the domain discretization. In this step, the geometry domain developed previously is subdivided into a number of small subdomains, which are usually referred as elements. Each element has certain shape and number of nodes, depending on the property of the analysis. For example, the elements are often short line segments for a 1D domain and usually small triangles and rectangles for the 2D domain; a linear line element has two nodes, whereas a linear triangular element has three nodes. Nodes and elements are the basic entities that the mesh consists of. The discretization of the domain is perhaps the most important step in any finite element analysis because the generated mesh affects the computer storage requirements, the computation time, and the accuracy of the numerical results. In ANSYS, the procedure for generating a mesh of nodes and elements consists of three main steps:

1. Set the element attributes.

2. Set mesh controls (size, shape etc.).

3. Generate the mesh.

Before generating a mesh of nodes and elements, the appropriate element attributes are defined for different components in the model. In this model, three types of elements are used as following:

1. Solid cylinder

   - Element type: PLANE42, 2D 4-node structural solid (Figure 3.2)
   - Element description: PLANE42 is used for 2D modeling of solid structures. The element has four nodes with two DOFs at each node: translations in the nodal x and y directions. The element has plasticity, creep, swelling, stress stiffening, large deflection, and large strain capabilities.

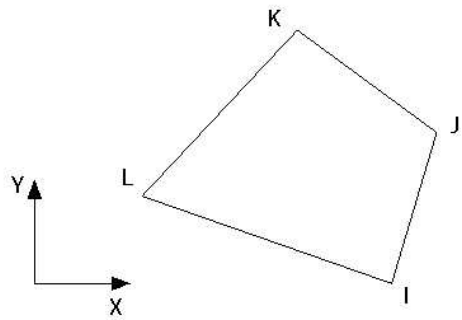

Figure 3.2 Two-dimensional four-node structural solid element PLANE42.

   - Element material proprieties: The solid cylinder is made of homogeneous skull-like materials. The human skull's material properties are assigned to this element: density: 1412 kg/m^3; Young's modulus: 6.5 GPa; Poisson's ratio: 0.22; compressive wave speed: 2292.5 m/s; shear wave speed: 1373.5 m/s [26].

2. Surrounding medium

   - Element type: FLUID 29, 2D acoustic fluid (Figure 3.3)
   - Element description: In ANSYS, FLUID29 is the only one choice to model 2D acoustic fluid fields. This 2D four-node acoustic fluid element is used to mesh the surrounding air medium. The element has four corner nodes

with four DOFs per node: translations in the nodal x, y directions and pressure. The translations, however, are applicable only at nodes that are on the interface. For irregular shapes, the triangle option is used.

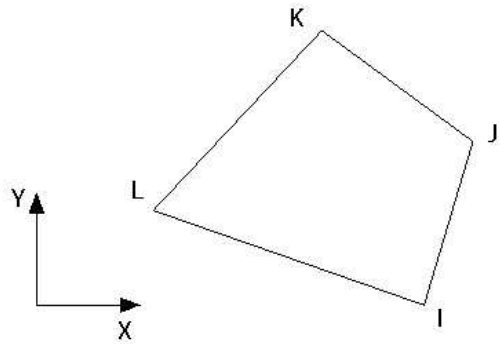

Figure 3.3 Two-dimensional four-node acoustic fluid element FLUID29.

- Element material properties: The material properties of air are assigned to this element: speed: 340 m/s; density: 1.2 kg/m^3.

3. Absorbing boundary

- Element type: FLUID129, 2D infinite acoustic (Figure 3.4)

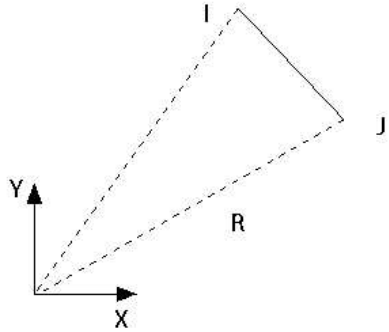

Figure 3.4 Two-dimensional infinite acoustic element FLUID129.

- Element description: FLUID129 is a companion element to the previous 2D acoustic fluid element, FLUID29. It is used as an envelope to a model

made of the 2D acoustic fluid finite elements. It simulates the absorbing effects of a fluid domain that extends to infinity beyond the boundary of the finite element domain. A second-order absorbing boundary condition is realized using this element so that an outgoing pressure wave reaching the boundary of the model is "absorbed" with minimal reflections back into the fluid domain. In this case, the element is used to model the boundary of 2D fluid regions, and as such, it is a line element. It has two nodes with one pressure degree of freedom per node. The absorbing boundary meshes are generated along all the nodes located on the absorbing boundary.

After defining the element attributes, the next step is to determine the appropriate mesh density. In a FEA, there are no definitive rules other than some general guidelines to decide the mesh density to obtain reasonably good results. For all wave propagation models, the mesh should be fine enough to resolve the wave. A general guideline is to have at least 20 elements per wavelength along the direction of the wave [18], [19]. An initial analysis is first performed using a mesh based on the general guidelines and the results of this preliminary analysis is compared with known analytical solutions. If the discrepancy between known analytical solutions and calculated results is too great, the meshes are refined. Keep refining meshes until the refinement gives nearly identical accurate results. When the two meshes give nearly the same accurate results, then the coarser model is preferred considering that the computation cost is less. In this case study after a few preliminary analyses, 20 elements per air wavelength are used for all the regions in the model, and good agreement is obtained between the calculated results and theoretical solutions, as shown in Section 3.2.4.

3.2.2 Apply the loads and obtain the solutions

A harmonic analysis, by definition, assumes that the applied load varies harmonically (sinusoidally) with time. To completely specify a harmonic load, three pieces of information are required: the amplitude, the phase angle, and the forcing frequency. Figure 3.5 shows the incident plane wave with frequency of 3 kHz, phase angle of 0° and amplitude of 1 Pa.

3.2.3 Summarize the parameters

Here is a list of the parameters used in 2D rigid cylinder model:

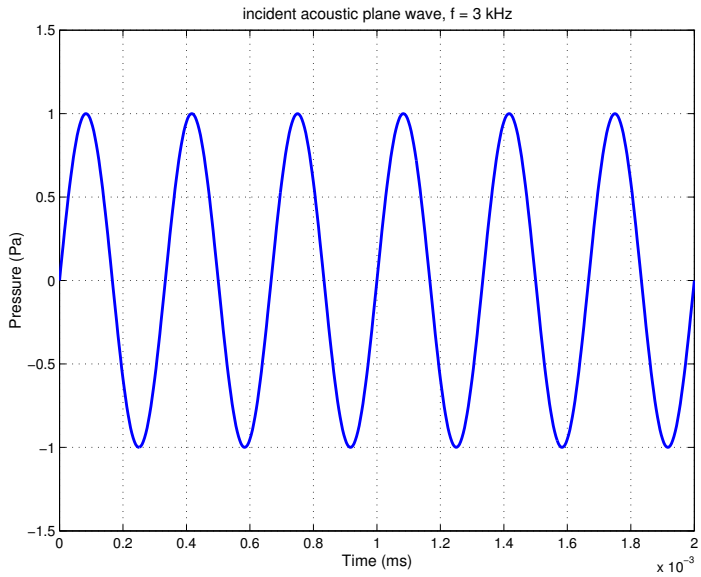

Figure 3.5 Incident acoustic plane wave ($f = 3$ kHz).

$f = 3$ kHz
$c_{air} = 340$ m/s
Cylinder: $\rho_{cylinder} = 1412$ kg/m^3, $E = 6.5$ GPa; $\sigma = 0.50$
Air: $\lambda_{air} = 340/3000 = 0.113$ m, $\rho_{air} = 1.2$ kg/m^3
$a = 0.4\lambda_{air} = 0.0452$ m
BOUND $= a + 0.9\lambda_{air} = 0.1473$ m
$\varphi_{inc} = 0^o$;
$X_{inc} = -(a + 0.5\lambda_{air}) = -0.1020$ m
$P_{inc} = 1$ Pa
DPW = 20

3.2.4 Compare the simulation results and the theoretical solution

Scattering by a 2D infinite rigid, immovable cylinder is a well-studied case and theoretical results are available (refer to Section 2.2). When a plane wave strikes the rigid cylinder in its path, in addition to the undisturbed plane wave there is a scattered wave, spreading out from the cylinder in all directions, distorting and interfering with the plane wave, which results in the total acoustic field. The FEA simulation results for the total acoustic field are compared with the analytical

solutions given in Section 2.2.1, and good agreement is found. Both the simulation results and the analytical solution for the total pressure distribution on the cylinder surface and along the $+x$ axis are plotted in Figure 3.6. The corresponding cylinder coordinate system is illustrated in Figure 3.7, where θ is the angle between the $+x$ axis and the observation position vector, measured counterclockwise.

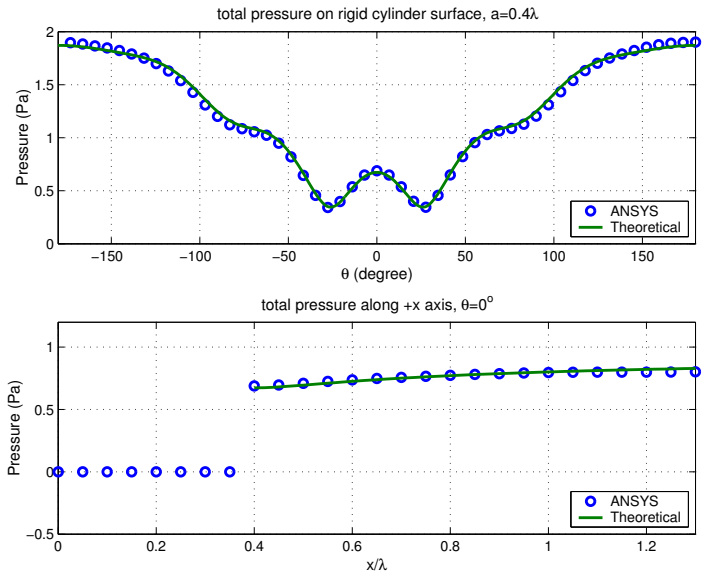

Figure 3.6 The rigid cylinder ($a = 0.4\lambda$) simulation results vs. analytical solutions. Top: total acoustic pressure on cylinder surface Bottom: total acoustic pressure along $+x$ axis.

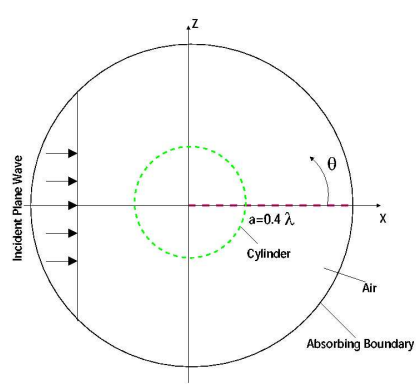

Figure 3.7 The corresponding cylinder coordinate system.

3.3 Two-Dimensional Shell Cylinder

3.3.1 FEA model description

In this case study, a 2D shell cylinder structure is submerged in air medium. The geometry and other parameters used in the FEA model (Figure 3.8) are as following:

$f = 3$ kHz;

Interior medium: water ($c = 1500$ m/s, $\rho = 1000$ kg/m^3)

Outer medium: air ($c = 340$ m/s, $\rho = 1.2$ kg/m^3, $\lambda_{air} = 340/3000 = 0.113$ m)

Shell: thickness $= 0.15\lambda_{air}$, $\rho_{shell} = 1412$ kg/m^3, $E = 6.5$ GPa, $\sigma = 0.50$

$a = 0.4\lambda_{air} = 0.0452$ m

BOUND $= a + 0.9\lambda_{air} = 0.1473$ m

$\varphi_{inc} = 0^o$

$X_{inc} = -(a + 0.5\lambda_{air}) = -0.1020$ m

$P_{inc} = 1$ Pa

DPW $= 20$

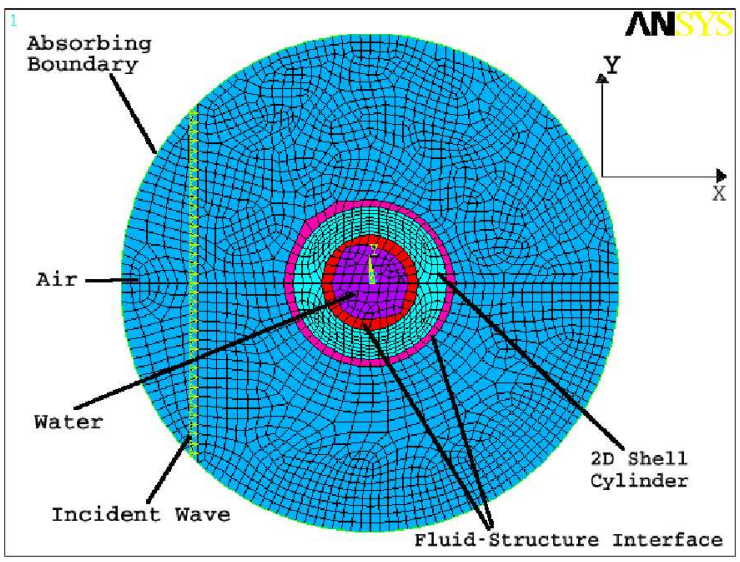

Figure 3.8 FEA model for 2D rigid shell cylinder.

3.3.2 Two-dimensional rigid shell cylinder

A 2D infinite rigid, immovable shell cylinder has the same boundary conditions along the outer shell surface as that of a 2D infinite rigid, immovable cylinder. In both

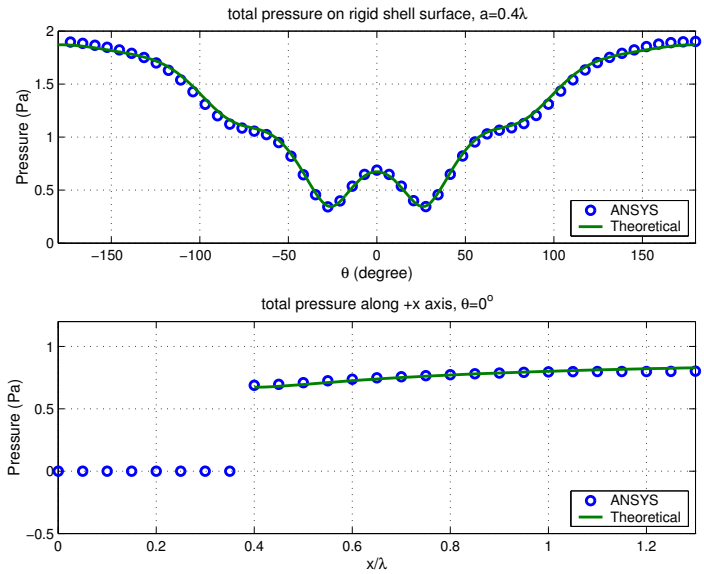

Figure 3.9 The rigid shell simulation results vs.analytical solutions. Top: total acoustic pressure on shell surface; Bottom: total acoustic pressure along $+x$ axis.

cases, the incident wave does not propagate into the inside of the cylinder and thus the sound pressure distribution solely depends on the size of the cylinder scatterer. Using the formula given in Section 2.2.1, the simulation results are compared with the analytical solutions for the total pressure distribution on the cylinder surface and along the $+x$ axis. Both are plotted in Figure 3.9. The coordinate system is the same as in Figure 3.7.

3.3.3 Two-dimensional elastic shell cylinder

In the previous case, the shell cylinder is rigid, immovable; that is, sound waves are not allowed to penetrate the scatterer. However, the human head is not perfectly rigid; thus, it allows sound waves to propagate into and through it, which is a fluid-solid-fluid structure. To simulate the fluid-solid-fluid structure, the target shell cylinder in this study is made of elastic material with the properties of human skull and the inside of the shell is filled with water. The FEA model for elastic shell cylinder is the same as the rigid shell cylinder as in Figure 3.8 except that the shell cylinder is assigned with different material properties and free to have displacements. Table 3.1 lists the material properties used for the shell cylinders.

Other parameters used in the FEA model are the following:

Table 3.1 Material properties for the shell cylinder

Model	Density	Young's modulus	Poisson's ratio	c_l	c_s
	(kg/m^3)	(Pa)		(m/s)	(m/s)
Rigid Shell	1412	6.5e9	0.50	Inf	1238.7
Elastic Shell #1	1412	6.5e9	0.22	2009.8	1373.5
Elastic Shell #2	2000	2e8	0.05	1585.4	218.2
Elastic Shell #3	1900	14e9	0.43	4019.6	1605.1

$f = 3$ kHz

Interior medium: Water ($c = 1500$ m/s, $\rho = 1000$ kg/m^3)

Outer medium: Air ($c = 340$ m/s, $\rho = 1.2$ kg/m^3, $\lambda_{air} = 340/3000 = 0.113$ m)

Shell: thickness $= 0.15\lambda_{air}$

$a = 0.4\lambda_{air} = 0.0452$ m

BOUND $= a + 0.9\lambda_{air} = 0.1473$ m

$\varphi_{inc} = 0^o$

$X_{inc} = -(a + 0.5\lambda_{air}) = -0.1020$ m

$P_{inc} = 1$ Pa

DPW = 20

Harmonic analysis is conducted on three elastic shell cylinders with different acoustic properties as listed in Table 3.1. The pressure contour for each case is plotted in Figure 3.10 together with the rigid shell cylinder case described in Section 3.3.2. In the rigid shell cylinder case (Figure 3.10(a)), the sound pressure inside of the shell is uniformly zero, which demonstrates the sound wave does not propagate into the rigid shell. In the elastic shell cylinder cases, the force on the shell cylinder applied by the incident sound wave causes the deformation of the elastic shell and thus the penetration of the sound wave into the elastic shell. Furthermore, under same level of incidence elastic shell cylinder #3 (Figure 3.10(d)) has the least deformation (represented by DMX) due to the large Poisson ratio, and on the contrary elastic shell cylinder #2 (Figure 3.10(c)) has the largest deformation.

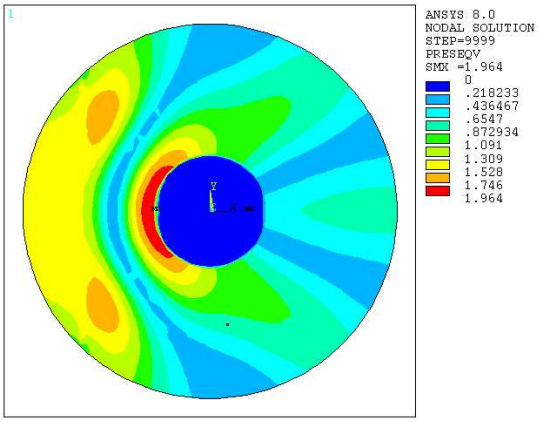

(a) Rigid shell

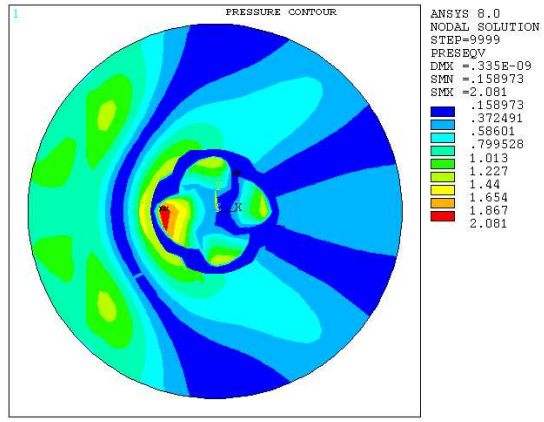

(b) Elastic shell 1

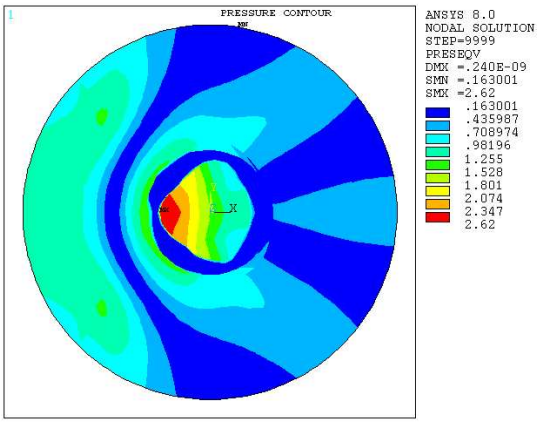

(c) Elastic shell 2

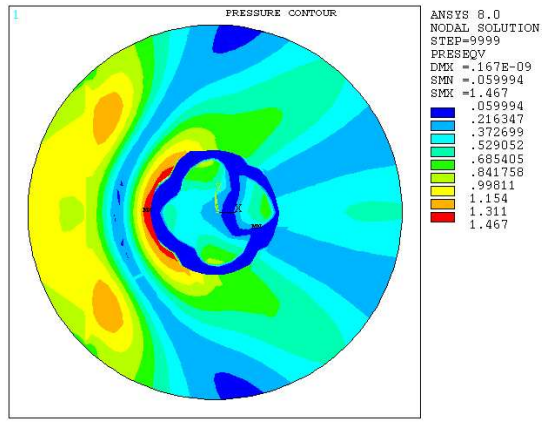

(d) Elastic shell 3

Figure 3.10 The pressure contours for rigid and elastic shell cylinders.

3.4 Three-Dimensional Rigid Sphere

In the 3D scenario, the finite-element harmonic analysis is carried out on the simplest geometry: the sphere. The 3D sphere case study is of considerable practical importance because many scattering objects are more or less spherical. In this case study, a rigid, immovable sphere of radius a, centered at the origin, is submerged in the air medium. Building a 3D FEA model is very similar to building a 2D FEA model as described in Section 2.2.2 except that 3D elements are used instead of 2D elements. A few 3D elements widely used in 3D acoustic FEA are described next.

3.4.1 Three-dimensional elements

1. SOLID45: 3D eight-node structural solid. This element (Figure 3.11) is used for the 3D modeling of solid structures. The element has eight nodes with three DOFs at each node: translations in the nodal x, y, and z directions. The element has plasticity, creep, swelling, stress stiffening, large deflection, and large strain capabilities.

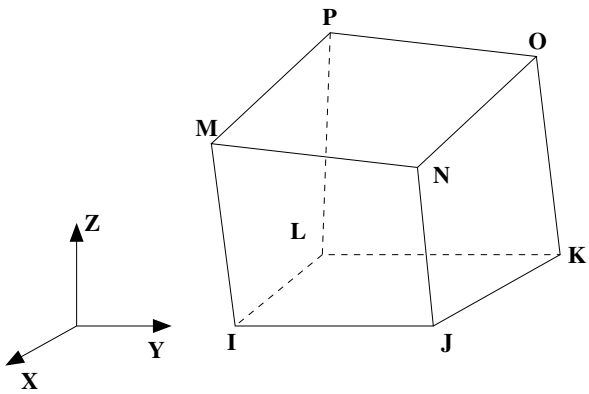

Figure 3.11 Three-dimensional eight-node structural element SOLID45.

2. SOLID 92: 3D 10-node tetrahedral structural. This element (Figure 3.12) has 10 nodes (including midside nodes) with three DOFs at each node: translation in the nodal x, y and z directions. It has a quadratic displacement and the curved shape with the midside node makes this element well suited to model irregular shapes, such as the human head.

3. FLUID30: 3D acoustic fluid. This element is the only one choice to model the 3D acoustic fluid field. The element has eight corner nodes with four DOFs per node: translations in the nodal x, y, and z directions and pressure. The translations, however, are applicable only at nodes that are on the interface. For irregular shapes, the tetrahedral option is used as in Figure 3.13.

4. FLUID130: 3D infinite acoustic. This element is a companion element to the previous 3D acoustic fluid element FLUID30. It is used as an envelope to a model made of the 3D acoustic fluid finite elements. It simulates the absorbing effects of a fluid domain that extends to infinity beyond the boundary of the

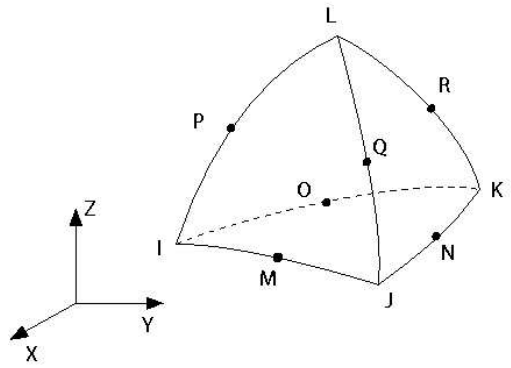

Figure 3.12 Three-dimensional 10-node tetrahedral structural element SOLID92.

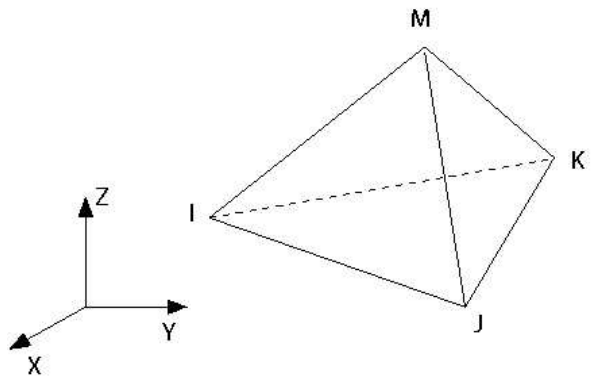

Figure 3.13 Three-dimensional eight-node tetrahedral fluid element FLUID30.

finite element domain. A second-order absorbing boundary condition is realized using this element so that an outgoing pressure wave reaching the boundary of the model is "absorbed" with minimal reflections back into the fluid domain. In this case the element is used to model the boundary of 3D fluid regions and as such, it is a plane surface element (Figure 3.14). It has four nodes with one pressure DOF per node.

3.4.2 Three-dimensional rigid sphere model

Figure 3.15(a) shows the FEA model for the 3D rigid sphere case; and (b) gives an illustration of the cross section view. In this FEA model, 3D rigid sphere meshes are completely made of SOLID45, the air medium domain meshes are made of FLUID30, and element FLUID130 is used for the absorbing boundary. Following is a list of

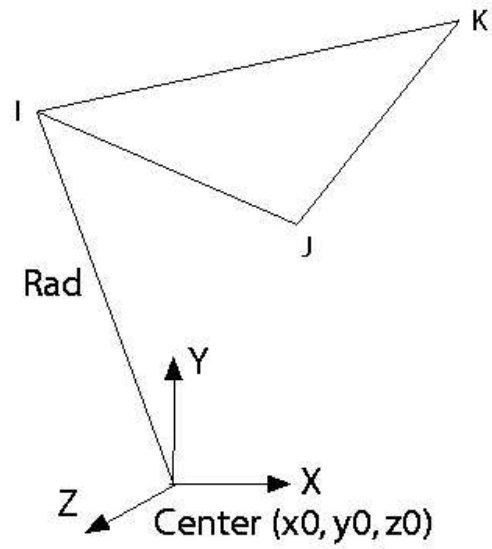

Figure 3.14 Three-dimensional infinite acoustic element FLUID130.

the parameters, including element material properties assigned to different elements. Notice that the mesh size is 10 elements per wavelength which is lower than required. This is due to the element limitation of the current ANSYS Research/Faculty/Student Version.

Parameters:

$f = 3$ kHz

Sphere: $\rho_{sphere} = 1412$ kg/m^3, $E = 6.5$ GPa, $\sigma = 0.22$

Air: $c = 340$ m/s, $\rho = 1.2$ kg/m^3, $\lambda_{air} = 340/3000 = 0.113$ m

$a = 0.4\lambda_{air} = 0.0452$ m

BOUND $= a + 0.9\lambda_{air} = 0.1473$ m

$\varphi_{inc} = 0^o$

$X_{inc} = -(a + 0.5\lambda_{air}) = -0.1020$ m

$P_{inc} = 1$ Pa

DPW $= 10$

3.4.3 Review the results

Scattering by 3D rigid sphere is also a well-studied case and theoretical results are available. Because the incident wave approaches along the $+z$ axis, which is the axis

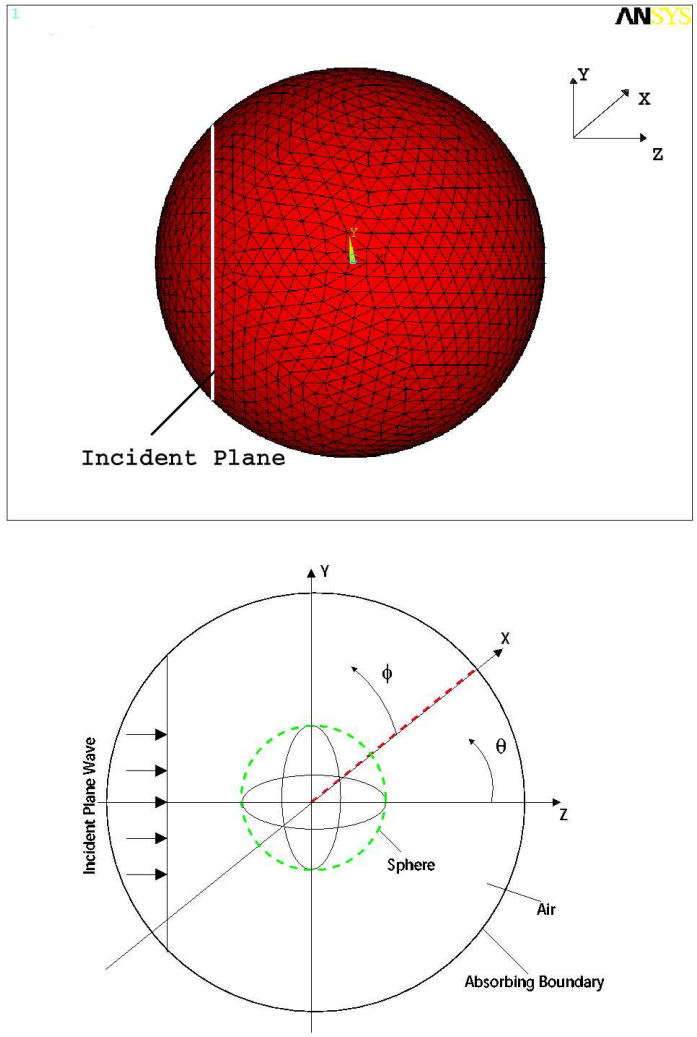

Figure 3.15 (a) Rigid sphere FEA model with the incident wave applied on the circular cross face (shown as the line in figure.) (b) Illustration of the cross section view.

of ϕ in the spherical coordinates, there is no dependence on ϕ. Therefore, it is logical to review the computational results of the pressure distribution along one constant-ϕ cross section. In Figure 3.16, the ANSYS simulation results of the distribution-in-angle (θ) of the total pressure field on the sphere surface at $\phi = 90^o$ are compared with the analytical solutions in Section 2.2.2. Furthermore, the total pressure along +z axis is also compared with the theoretical solutions. Over all average error of about 13% is found. As expected, the accuracy in 3D scale is impaired by the coarse

meshes (DPW = 10) due to the current ANSYS license limits on the number of elements and nodes.

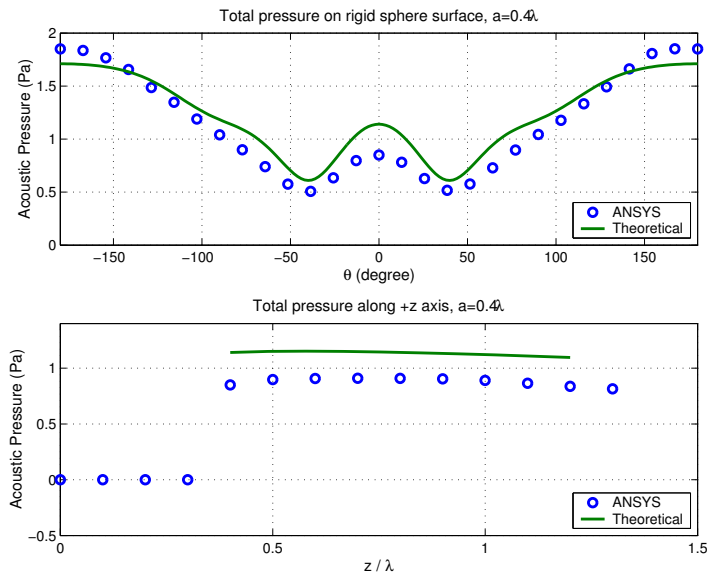

Figure 3.16 The rigid sphere simulation results vs. analytical solutions. Top: total acoustic pressure on sphere surface; Bottom: total acoustic pressure along $+z$ axis.

3.5 Three-Dimensional Nonrigid Sphere

For the perfectly rigid case the propagated wave does not enter the object. However, the real objects are usually nonrigid. Therefore, harmonic analysis procedure is conducted using a 3D nonrigid sphere in this case study. This case is of considerable practical importance because may scattering objects are more or less spherical. The FEA model for the 3D elastic sphere is the same as the rigid sphere case as in Figure 3.15, except that different material properties are assigned to the elements for the sphere. Here the nonrigid sphere's density and speed are assumed to be twice those of air. The air-borne incident harmonic wave propagates in the $+x$ axis direction.

Parameters:

$f = 3$ kHz

Sphere: $c_{sphere} = 680$ m/s, $\rho_{sphere} = 2.4$ kg/m^3

Air: $c = 340$ m/s, $\rho = 1.2$ kg/m^3, $\lambda_{air} = 340/3000 = 0.113$ m

$a = 0.4\lambda_{air} = 0.0452$ m

BOUND $= a + 0.9\lambda_{air} = 0.1473$ m

$\varphi_{inc} = 0^o$

$X_{inc} = -(a + 0.5\lambda_{air}) = -0.1020$ m

$P_{inc} = 1$ Pa

DPW $= 10$

Scattering by 3D elastic sphere is also a well-studied case, and theoretical results are available. In Figure 3.17, the ANSYS simulation results of the pressure distribution on the elastic sphere surface are compared with the analytical solutions in Section 2.2.2. When the propagating wave meets the nonrigid spherical target, acoustic pressure is distributed around the spherical surface, and also enters into the sphere. Reasonable agreements are found.

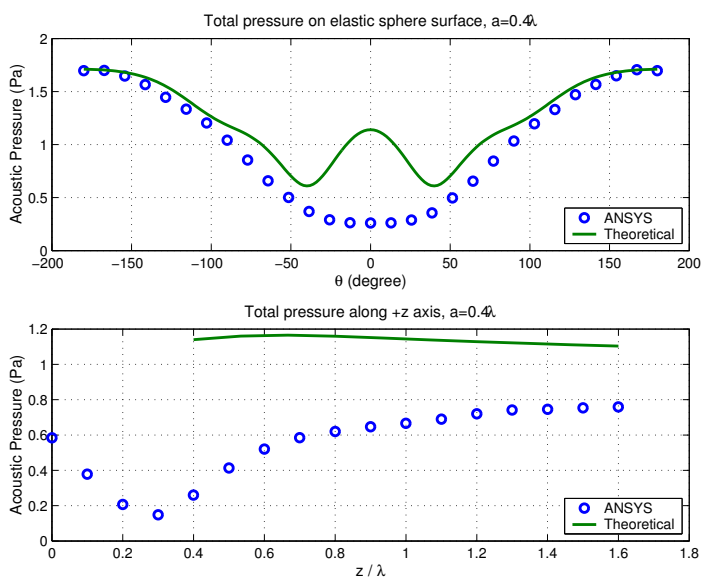

Figure 3.17 The elastic sphere simulation results vs. analytical solutions. Top: total acoustic pressure on sphere surface; Bottom: total acoustic pressure along $+z$ axis.

3.6 Summary

In this chapter, the ANSYS general harmonic analysis procedure is introduced. The air-borne acoustic wave (sinusoid plane wave) is incident on the geometric models such as 2D rigid cylinders, 2D rigid/elastic shell cylinders, and 3D water spheres. The

computational solutions of acoustic pressure distribution agrees well with the analytic solutions.

CHAPTER 4

TRANSIENT ACOUSTIC FINITE-ELEMENT ANALYSIS ON SIMPLE GEOMETRY MODELS

In this chapter, the feasibility of acoustic FEA in ANSYS is evaluated on some well-understood geometry models such as spheres and 2D solid and shell cylinders in the time-domain, i.e., transient analysis.

Transient analysis is more meaningful for the hearing protection project compared with harmonic analysis because in the real environment most severe hearing damages are caused by time varying noises rather than continuous noises [2]. It is the main interest of the current research to understand how the human head reacts to the time varying noise.

Transient analysis simulates the time-varying pulse propagation scenario and is more involved than a harmonic analysis because it requires more computer resources and more of *our* resources, in terms of the "engineering" time involved. To save a significant amount of these resources, preliminary studies are conducted to understand further the physics of the problem for validation purposes, that is, analyzing a simpler model provides better insight into the problem at minimal cost.

In this chapter, the basic procedure for a transient acoustic analysis in ANSYS is introduced and then several case studies using simple geometry models such as cylinders and spheres are described.

4.1 Acoustic Transient Analysis in ANSYS

Conducting an acoustic transient analysis in ANSYS follows the basic procedure for an acoustic analysis described in Section 3.1 and differs from a harmonic analysis in the following aspects:

1. A transient analysis, by definition, involves loads that are functions of time. To specify such loads, the load-versus-time curve is divided into suitable load steps. For each load step, both load values and time values are specified.

2. The finite-element discretized equations are solved at discrete time points. The Newmark time integration method [27] is used to solve the equations at those time points. The accuracy of the transient dynamic solution directly depends on the integration time step (ITS), which is the time increment between successive time points: the smaller the time step, the higher the temporal accuracy. However a time step size that is too small will waste computer resources.

To help develop the correct code for an acoustic transient analysis, several case studies are conducted in both two and three dimensions.

4.2 Acoustic Wave Propagation in Homogeneous Air Medium

A complete acoustic model for the propagation of an air-borne sound wave into the human head involves different media with different acoustic propagation properties. Table 4.1 lists the properties for different materials involved in the future air-head model [28–30]. Among all of them, sound speed in air is the lowest and thus the wavelength in air is the shortest. Therefore, for the FEA model, the smallest elements used are based on propagation in air. In the other words, to achieve good computation resolution for the mixed-property model, the optimal parameters for simulating propagation in air are determined.

In this case study, one-cycle sinusoid wave with the center frequency of 3 kHz is propagated in homogeneous lossless air medium in a 2D scenario. It serves as the simplest example for conducting an acoustic transient analysis and helps find the optimized parameters for more complicated analyses later. Furthermore, this 2D air transient analysis is evaluated to determine whether the computation domain space introduces artifacts.

4.2.1 Model generation

A simple geometry model in Figure 4.1 is used that is similar to the 2D cylinder harmonic analysis model except that the 2D cylinder is air. The locations A (-0.9λ, 0), B (-0.65λ, 0), C (0.4λ, 0), H (0, 0.4λ) (in Figure 4.1) denote where the acoustic pressure waveforms are plotted in the next section to evaluate the parameters DPW (division per wavelength), LSS (load step size), ITS (integration time step), and BOUND (FEA absorbing boundary). Here is a list of the other parameters:

$f = 3$ kHz

Table 4.1 Acoustic properties of different media and tissues

Material	Speed of Sound (m/s)	Density (kg/m^3)
Air	340	1.2
Water	1500	000
Soft tissues	1520-1580	980-1010
Lipid-based tissues	1400-1490	920-940
Collagen-based tissues	1600-1700	1020-1100
Aqueous humor	1002-1006	1500
Vitreous humor	1090	1530
Blood	1580	1040-1090
Brain-grey	1532-1550	1039
Brain-white	1532-1550	1043
Skull-compact inner and outer tables	2600-3100	1900
Skull-spongy diploe	2200-2500	1000
Long bone-outer layer	2600-3100	1900
Long bone-inner layer	1700-2000	1100
Teeth	3500-4000	2200

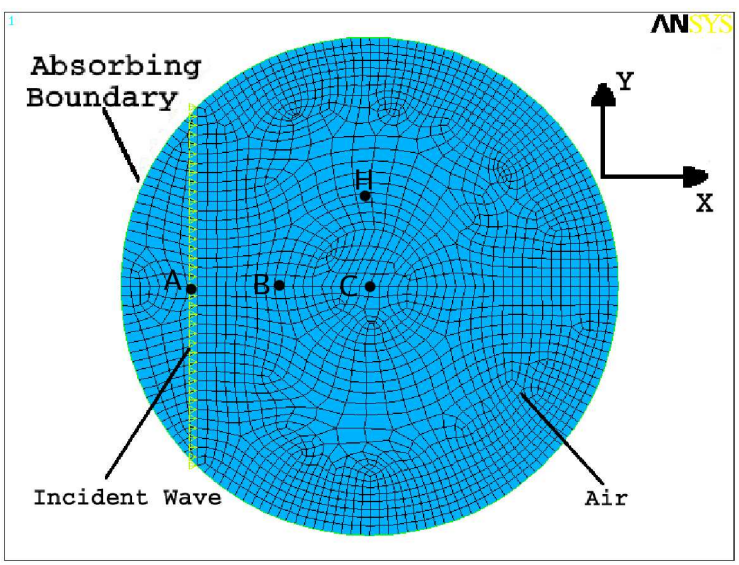

Figure 4.1 FEA model for sound propagation in air.

$T = 1/f = 0.33$ ms
$c_{air} = 340$ m/s
Air: $\lambda_{air} = 340/3000 = 0.113$ m; $\rho_{air} = 1.2$ kg/m^3
$X_{inc} = -(0.9\lambda_{air}) = -0.1020$ m
$P_{inc} = 1$ Pa
Computational length = 3 T

4.2.2 Apply the loads and review the results

Different from the harmonic analysis, one-cycle sinusoid wave with the center frequency of 3 kHz (Figure 4.2) is excited at the incident plane instead of a harmonic wave, and propagates in the $+x$ direction. The load is applied with certain LSS, 1/20 T in Figure 4.2, and ramped between adjacent load steps. LSS and ITS (especially ITS) are two unique parameters for transient analysis only, and they play an important role in the temporal accuracy. Intuitively the smaller the LSS, the better the load-versus-time curve is resolved; the smaller the ITS, the higher the temporal resolution. However, an ITS that is too small will waste computer resources and exceedingly small numbers can cause numerical difficulties. To choose a suitable value for ITS, there are a few guidelines ([18], "Transient Dynamic Analysis"):

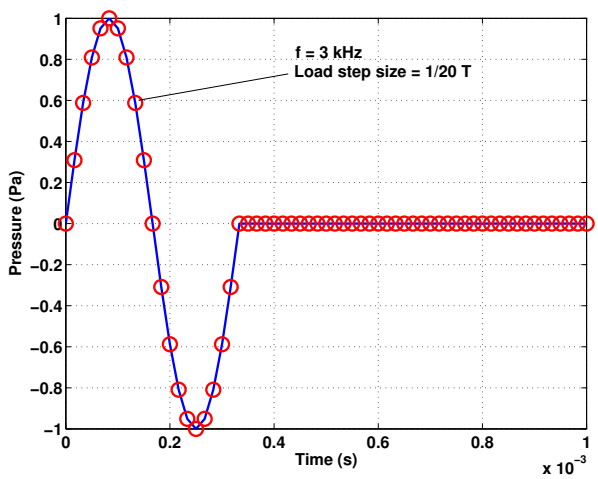

Figure 4.2 The incident one-cycle sinusoid wave, center frequency at 3 kHz.

1. Resolve the response frequency: For the Newmark time integration scheme, it has been found that using approximately 20 points per cycle of the frequency of

interest results in a reasonably accurate solution. That is, if f is the frequency (in cycles/time), the ITS is given by ITS = 1/20 T.

2. Resolve the applied load-versus-time curve: The time step should be small enough to "follow" the loading function. ITS should be no bigger than the smallest LSS to follow the loads.

3. Resolve the wave propagation: The time step should be small enough to capture the wave as it travels through the elements, i.e., ITS $\leq T/$DPW, where $T = 1/f$, f is the center frequency of the incident pulse wave, and DPW is the number of the elements per wavelength.

Same as the harmonic analysis, DPW affects the spatial resolution, and BOUND affects the degree of the incident wave's distortion along the circular boundary of the computation domain because the incidence plane is located left of the center plane in the computation domain. In general, the mesh must be fine enough to resolve the largest dominant frequency. A general guideline is to have at least 20 elements per wavelength along the propagation direction, that is, DPW = 20 ([18], "Modeling and Meshing Guide"). The acoustic absorbing boundary should be located at least 0.2λ from the target object ([18], "Coupled-Field Analysis Guide").

Table 4.2 Transient analysis of the propagation in air medium

Test	BOUND (a+)	DPW	LSS/T	ITS/T
1	0.9λ	10	1/20	1/20
2	0.9λ	10	1/40	1/40
3	0.9λ	20	1/20	1/20
4	0.9λ	20	1/20	1/40
5	0.9λ	20	1/40	1/40
6	0.9λ	20	1/60	1/60
7	0.9λ	30	1/60	1/60
8	1.4λ	20	1/20	1/20
9	1.4λ	20	1/20	1/60
10	1.4λ	20	1/60	1/60

Ten combinations of DPW, LLS, ITS, and BOUND (Table 4.2) are evaluated in Figures 4.3 and 4.4. The pressure waveforms at four locations, A, B, C, and H, which are indicated in Figure 4.1, are plotted. It was observed that, in general, larger

BOUND greatly enhances the computational accuracy (Test 8 $\sim$ 10 vs. Test 1 $\sim$ 7) while larger DPW and smaller ITS and LLS yield insignificant improvements. For future transient-analysis cases, DPW = 20, ITS = $T/20$, and LLS = $T/20$ will be considered to be sufficient and BOUND will be further evaluated in next section.

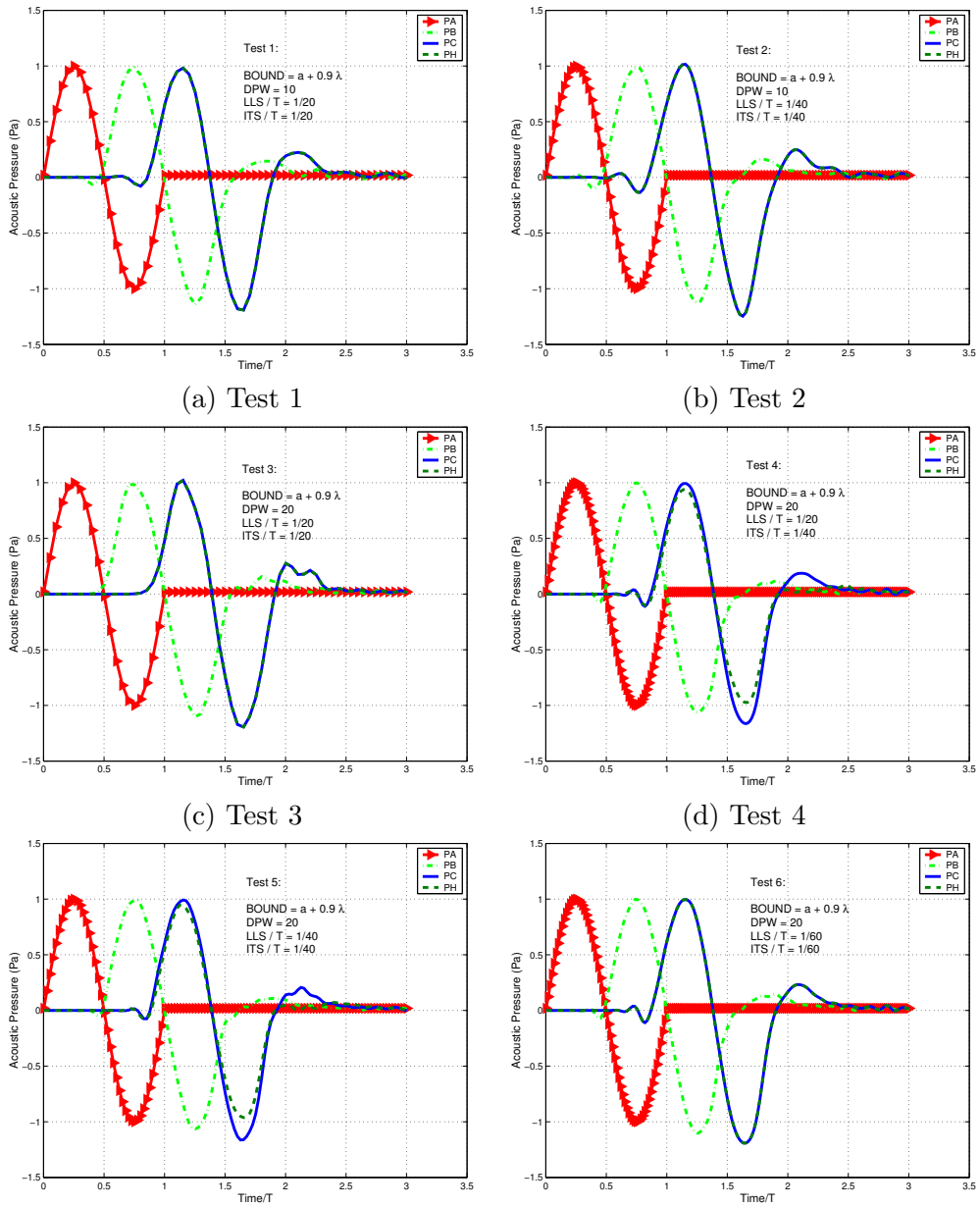

(a) Test 1 (b) Test 2

(c) Test 3 (d) Test 4

(e) Test 5 (f) Test 6

Figure 4.3 Sound propagation in air: Acoustic pressure vs. time, Test 1 $\sim$ 6.

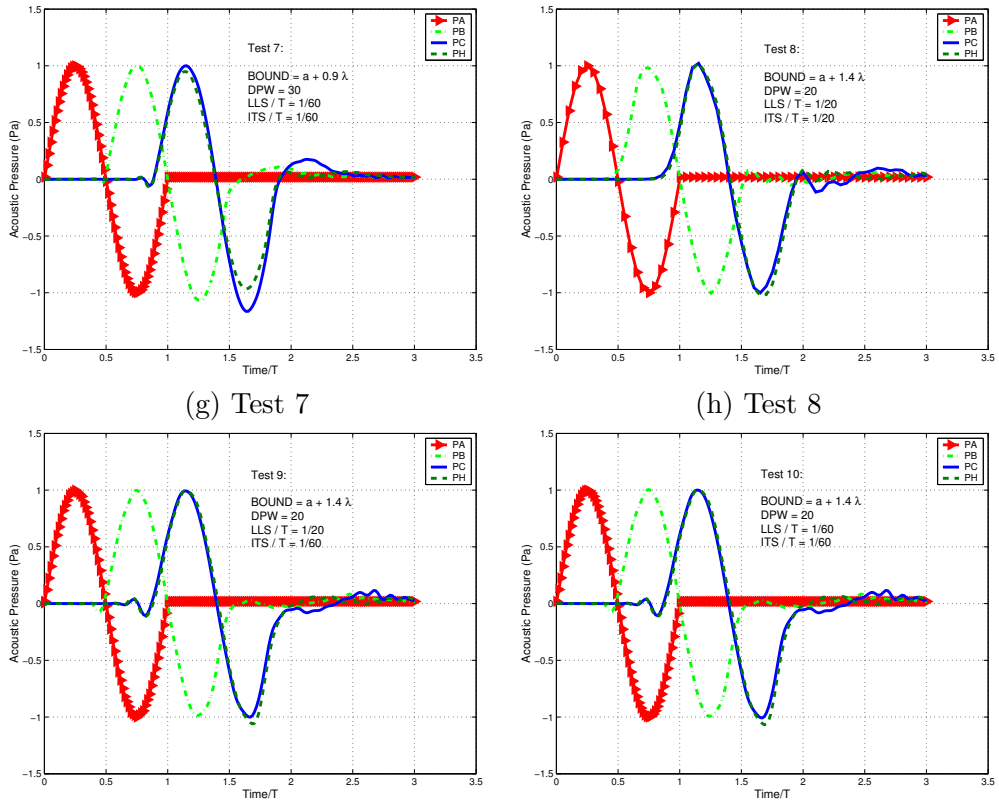

(g) Test 7 (h) Test 8

(i) Test 9 (j) Test 10

Figure 4.4 Sound propagation in air: Acoustic pressure vs. time, Test 7 $\sim$ 10.

4.3 Transient Analysis on Two-Dimensional Elastic Shell Cylinder

4.3.1 FEA model for two-dimensional elastic shell cylinder

A transient analysis on a 2D elastic cylinder shell is evaluated that includes property values of typical tissue (Table 4.1). Figure 4.5 shows the 2D soft (elastic) shell geometry used in the simulations. In this case study, the effect of BOUND is further evaluated in object spaces of different sizes. Here is a list of the parameters used in this case study:

$f = 3$ kHz

Interior medium: Water ($c = 1500$ m/s, $\rho = 1000$ kg/m^3)

Outer medium: Air ($c = 340$ m/s, $\rho = 1.2$ kg/m^3, $\lambda_{air} = 340/3000 = 0.113$ m)

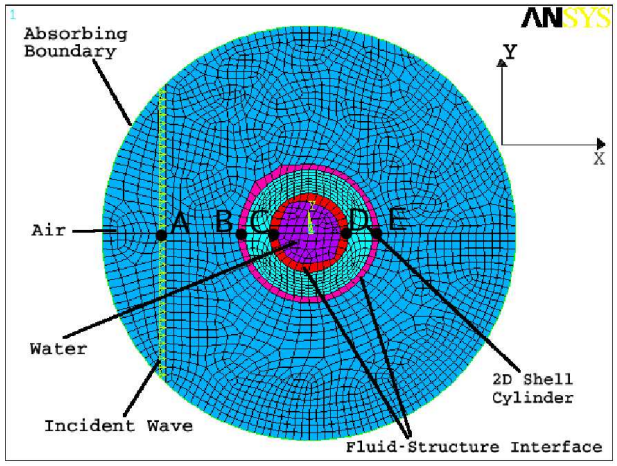

Figure 4.5 FEA model for 2D elastic shell cylinder.

Soft Shell: thickness = $0.15\lambda_{air}$, $c = 2800$ m/s, $\rho = 1900$ kg/m^3
$\varphi_{inc} = 0^o$
$P_{inc} = 1$ Pa
DPW = 30
LSS = ITS = 1/30 T
Computational length = 5 T
BOUND = variable
X_{inc} = variable

4.3.2 Review the results

Two 2D cylinder shell tests were carried out with different FEA absorbing boundary on the same target object (Table 4.3).

Table 4.3 Small 2D Shell Transient Analysis

Parameters	Test 1	Test 2
Shell inner radius (a)	$0.1\lambda_{air}$	$0.1\lambda_{air}$
Shell thickness (d)	$0.025\lambda_{air}$	$0.025\lambda_{air}$
BOUND	$a + d + 0.5\lambda_{air}$	$a + d + 2.5\lambda_{air}$
Incident wave position	$-(a + d + 0.2\lambda_{air})$	$-(a + d + 1.2\lambda_{air})$
Distance between B and E (Figure 4.5)	$0.57\lambda_{air}$	$2.56\lambda_{air}$

Figure 4.6 shows x-axis acoustic pressure waveforms at locations A, B, C, and D (Figure 4.5). The circular shape of the absorbing boundary causes distortion of the propagated wave along the boundary, and thus induces additional artificial incident waves along non $+x$ axis direction. When the absorbing boundary is positioned at a greater distance from the object, less undesirable interference reaches the target object in the same computational length scale. The distance between B and E (E is at the absorbing boundary; Figure 4.5) in Table 4.3 provides a rough estimate of the shortest possible time required for the interference wave to reach B from the absorbing boundary. Comparing the first period of the pressure waveform at B, the waveform in Test 2 is more symmetric than in Test 1. A reasonable explanation is that it requires about 0.5 T for the interference wave at E to reach B in Test 1 whereas it requires about 2.5 T in Test 2. It is also suspected that the significant variation of the pressure waveform shape at C in Test 1 at about 1 T after the incident wave reaches C is due to the interference wave from the absorbing boundary reaching the target shell cylinder by that time. In Test 2, this interference is smaller, but still present, because it takes longer for the interfering waves at a further absorbing boundary location to reach the shell cylinder.

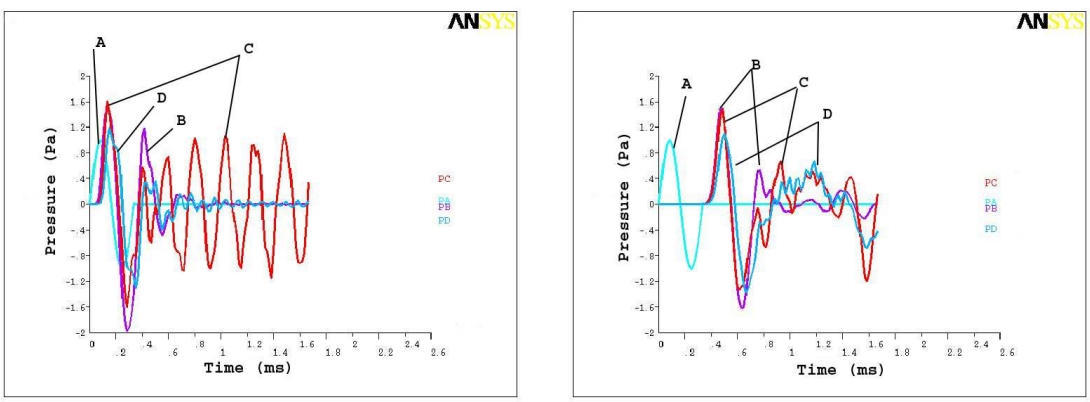

(a) Test 1 (b) Test 2

Figure 4.6 Acoustic pressure waveforms in Test 1 (a) and Test 2 (b).

To further demonstrate this observation, two large 2D shell cylinder tests were carried out with different FEA absorbing boundary (Table 4.4). In Test 3, the absorbing boundary is located the same distance from the shell cylinder as in Test

1. And in Test 4, the absorbing boundary is moved further away than in Test 3 but not as far as in Test 2.

Table 4.4 Large 2D Shell Transient Analysis

Parameters	Test 3	Test 4
Shell inner radius (a)	$0.58\lambda_{air}$	$0.58\lambda_{air}$
Shell thickness (d)	$0.09\lambda_{air}$	$0.09\lambda_{air}$
BOUND	$a + d + 0.5\lambda_{air}$	$a + d + 1.0\lambda_{air}$
Incident wave position	$-(a + d + 0.2\lambda_{air})$	$-(a + d + 0.4\lambda_{air})$
Distance between B and E (Figure 4.5)	$0.81\lambda_{air}$	$1.34\lambda_{air}$

Figure 4.7 shows x-axis acoustic pressure waveforms at locations A, B, C, and D (Figure 4.5). In Test 4, an abnormal peak pressure amplitude occurs at C about 1 T after the incident wave reaches this position, which is not observed in the other tests. Again it is very likely due to the interfering waves coming from the absorbing boundary. Similar to the previous small shell cylinder case, more symmetric pressure waveforms for the first period are found in Tests 3 and 4. In both Tests 3 and 4, significant variations of the pressure waveform shape at B, C, and D are observed about 1 T after the incident wave reaches that position, which implies the absorbing boundary is not sufficiently further away from the shell cylinder.

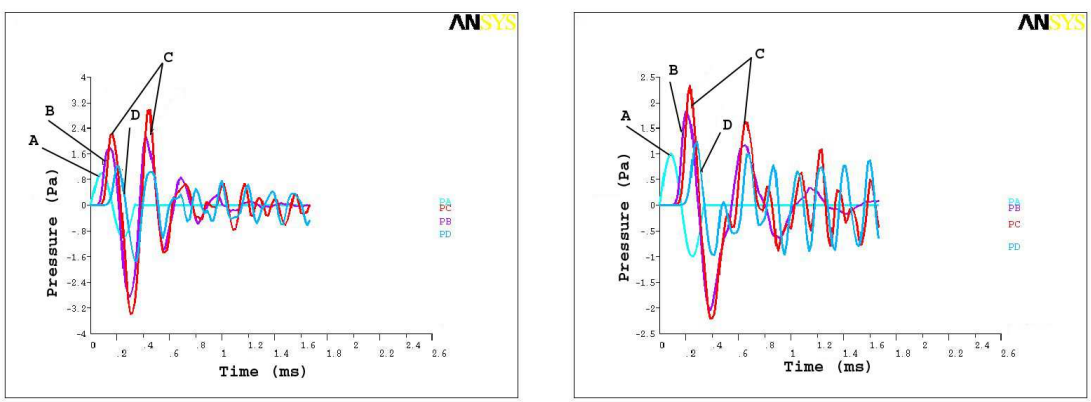

(a) Test 3 (b) Test 4

Figure 4.7 Acoustic pressure waveforms in Test 3 (a) and Test 4 (b).

Based on the observations above, it is concluded that in our studies, FEA absorbing boundary has a significant impact on the computation accuracy and larger BOUND is preferred to decrease the interference due to the circular absorbing boundary and to better simulate the incident plane wave.

4.4 Transient Analysis on Two-Dimensional Rigid Cylinder

In this case study, transient analysis is conducted using a 2D rigid cylinder and different visualization methods of the FEA results are evaluated.

4.4.1 FEA model for two-dimensional rigid cylinder

Using the same FEA model in Section 3.2 (Figure 4.8), a one-cycle sinusoid wave as in Figure 4.2 is applied at the incident plane.

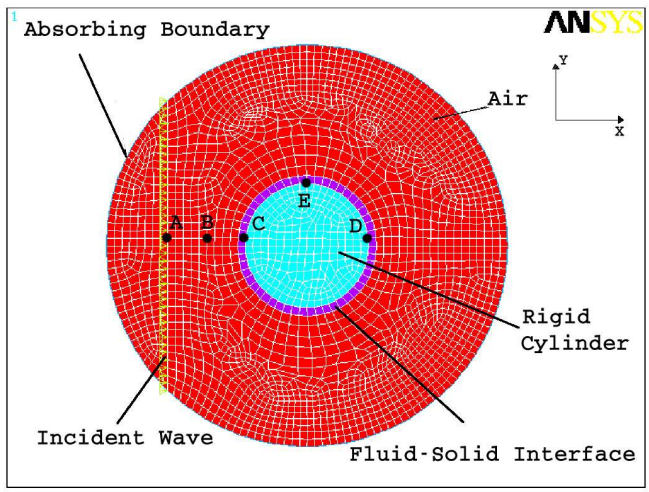

Figure 4.8 FEA model for transient analysis on 2D rigid cylinder.

Here is a list of the parameters used in this case study:
$f = 3$ kHz and 125 Hz
$T = 1/f$;
Cylinder: $\rho_{cylinder} = 1412$ kg/m^3; $E = 6.5$ GPa; $\sigma = 0.22$
Air: $c_{air} = 340$ m/s; $\rho_{air} = 1.2$ kg/m^3
$a = 0.4\lambda_{air,f=3kHz} = 0.0452$ m
BOUND $= a + 0.9\lambda_{air}$

$\varphi_{inc} = 0^o$
$X_{inc} = -(a + 0.5\lambda_{air})$
$P_{inc} = 1$ Pa
DPW = 20
LSS = ITS = 1/20 T
Computational length = 3 T

4.4.2 Visualize the results

Scientific visualization using computer techniques has long been recognized as an extremely powerful method for conveying information, because it allows for the quick interpretation and comprehension of complex phenomena. In acoustics, contour plots [31], still pictures and movies produced using schlieren photography [32], and computer animations generated in Mathematica [33] and MATLAB [34] have been used for visualizing the propagation of sound waves. Here, the FEA results are visualized in two ways:

1. The acoustic pressure at specific locations is plotted along the time axis. Five locations are chosen as indicated in Figure 4.8. They are: A (-0.9λ, 0), B (-0.65λ, 0), C (-0.4λ, 0), D (0.4λ, 0), and E (0, 0.4λ). The computed pressure data as a function of time are loaded to and plotted in MATLAB (Figure 4.9). Two cases with different center frequency (f = 125 Hz and f = 3 kHz)

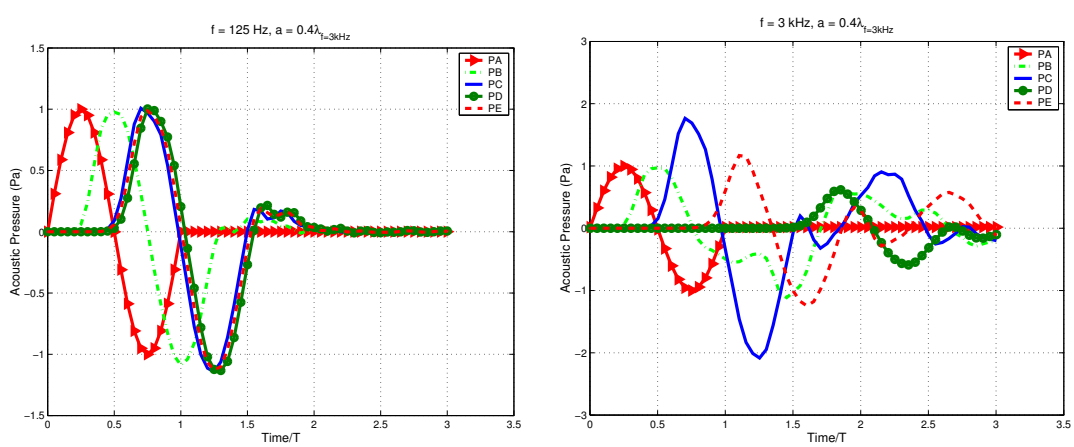

(a) f = 125 Hz (b) f = 3 kHz

Figure 4.9 Transient analysis on 2D rigid cylinder: Acoustic pressure vs.time.

are studied. It is found that in the 125-Hz case, the incident wave travels nearly undistorted while significant scattering exists in the 3-kHz case. The observations agree with the theoretical explanation: The target cylinder size is the same for both cases ($a = 0.4\lambda_{air,f=3kHz} = 0.0452$ m). Therefore in the 125-Hz case, the scatter size is significantly small comparing to the wavelength and thus the scattering by the scatter is negligible. On the other hand, in the 3-kHz case, the scatter size is comparable to the wavelength and thus significant scattering by the cylinder is observed.

2. Capture the pressure contour plot at each time step and play the frames continuously, an animation movie can be generated to show the complete propagation process of the incident wave. Figures 4.10 and 4.11 shows selected eight frames of the animation movie at time step of 5, 10, 15, 20, 25, 30, 40, and 50 respectively (center frequency is 3 kHz). With this technique, the temporal behavior of the wave propagation is clearly conveyed.

4.5 Transient Analysis on Three-Dimensional Water Sphere

4.5.1 FEA model for watersphere

In this case study, transient analysis is conducted on a 3D sphere of water that is submerged in air medium. The geometry of the model is illustrated in Figure 4.12. The parameters used in the FEA model are as the following:

$f = 3$ kHz

Watersphere: $c = 1500$ m/s, $\rho = 1000$ kg/m^3

Air: $c = 340$ m/s, $\rho = 1.2$ kg/m^3, $\lambda_{air} = 340/3000 = 0.113$ m

$a = 0.4\lambda_{air} = 0.0452$ m

BOUND $= a + 0.9\lambda_{air} = 0.1473$ m

$\varphi_{inc} = 0^o$

$X_{inc} = -(a + 0.5\lambda_{air}) = -0.1020$ m

$P_{inc} = 1$ Pa

DPW = 20

LSS = ITS = 1/20 T

Computational length = 3 T

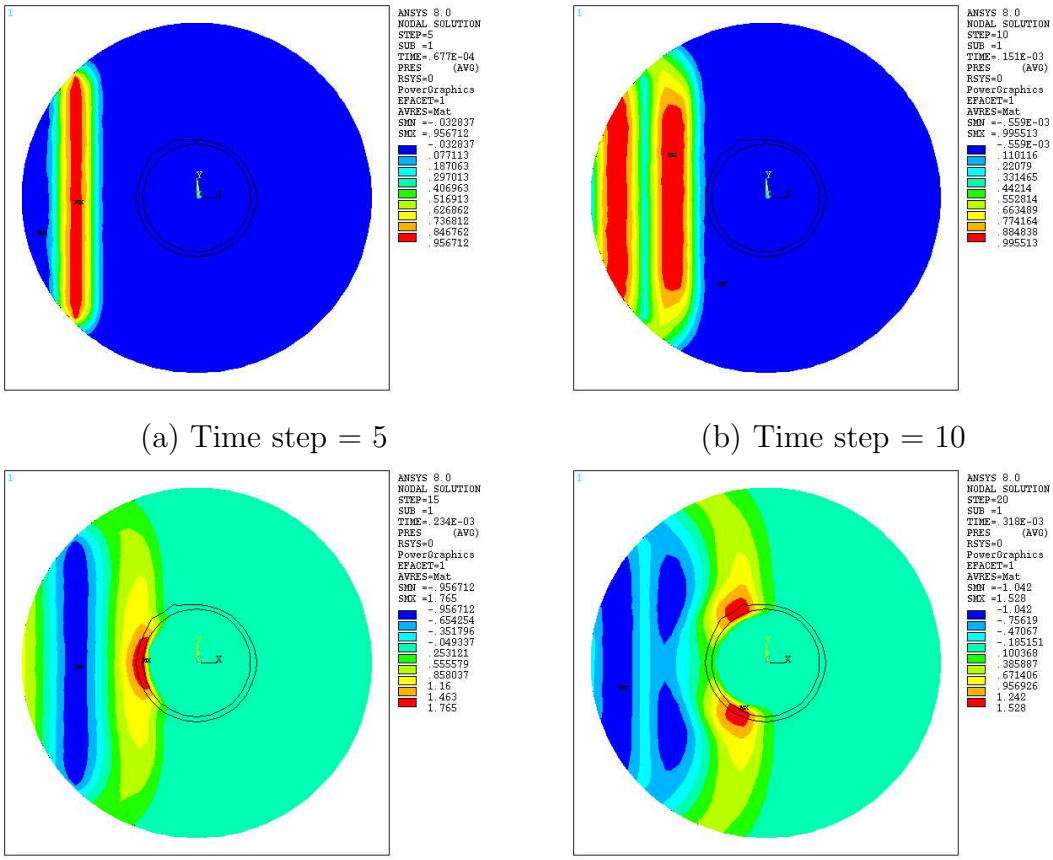

(a) Time step = 5

(b) Time step = 10

(c) Time step = 15

(d) Time step = 20

Figure 4.10 Transient analysis on 2D rigid cylinder: Pressure distribution at time step 5, 10, 15, and 20 (f = 3 kHz).

4.5.2 Review the results

The acoustic pressure waveforms at four selected locations (Figure 4.12) are plotted in Figure 4.13. The five locations are indicated in Figure 4.12. They are: A (0, 0, -0.9λ), B (0, 0, -0.4λ), C (0, 0, 0), and D (0, 0, 0.4λ). A is located on the incident plane, B and D are located on the surface of the sphere, and C is at the center of the sphere. From the pressure waveforms, it is determined that about 0.5 T is required for the incident wave to travel from A to B whereas the travel time is about 0.1 T from B to C. These travel time estimates agree with theory and thus validates the temporal accuracy of the FEA. Furthermore, the instantaneous acoustic intensity was calculated based on the FEA acoustic pressure data from

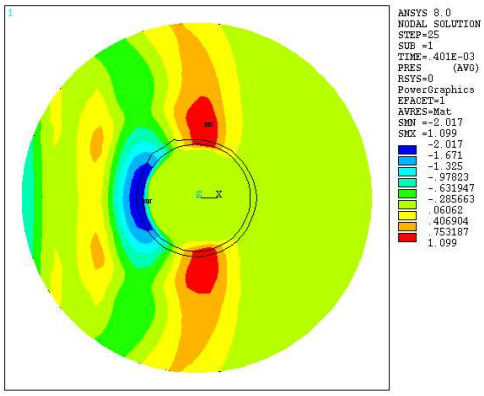

(a) Time step = 25

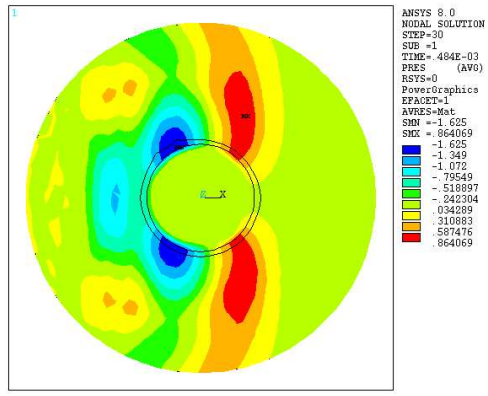

(b) Time step = 30

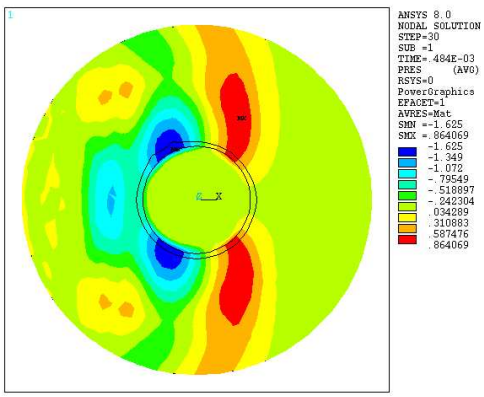

(c) Time step = 40

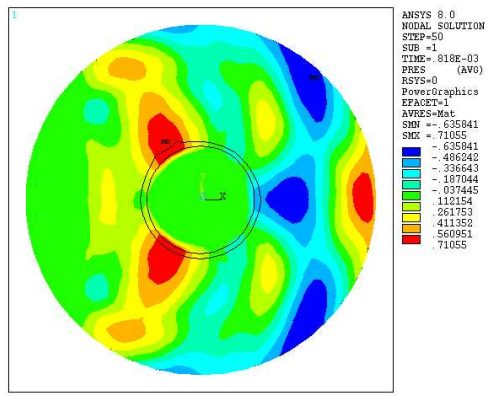

(d) Time step = 50

Figure 4.11 Transient analysis on 2D rigid cylinder: Pressure distribution at different time step 25, 30, 40, and 50 (f = 3 kHz).

$$I_A = \frac{p(t)^2}{\rho_{air} c_{air}}, I_C = \frac{p(t)^2}{\rho_{water} c_{water}} \tag{4.1}$$

where $p(t)$ are the peak values of the acoustic pressure at their respective locations. The instantaneous acoustic intensity loss from air to water was estimated from

$$Loss_{dB} = 10 log_{10} \frac{I_{peak,C}}{I_{peak,A}} \tag{4.2}$$

From the FEA data (Figure 4.13)), the intensity loss from air to water was estimated to be 34 dB, a reasonable value relative to a theoretical loss estimate (33 dB) for normal incidence at a planar air-water boundary.

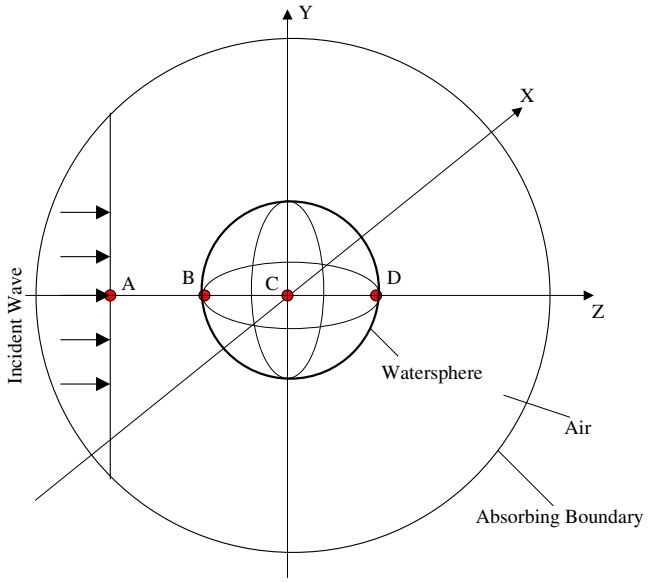

Figure 4.12 Geometry illustration for 3D watersphere model.

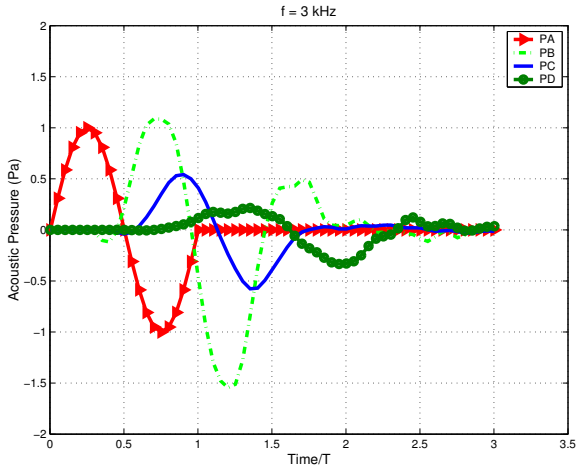

Figure 4.13 Acoustic pressure waveforms for the water sphere case at locations A, B, C, and D (Figure 4.12), $f = 3$ kHz.

4.6 Summary

In this chapter, the ANSYS general transient analysis procedure is introduced. The air-borne acoustic wave (one-cycle sine wave) is incident on the geometric models such as 2D homogeneous air medium, 2D rigid cylinders, 2D elastic shell cylinders,

and 3D water spheres. A group of parameters involved in FEA transient analysis, DPW, LLS, ITS, and BOUND, are evaluated. Furthermore, the visualization techniques are explored to capture the temporal behavior of the transient processes.

CHAPTER 5

FINITE-ELEMENT ANALYSIS ON HUMAN HEAD

In this chapter, both a 2D and a 3D FEA human head models are developed based on a complete digital image dataset of a normal adult male human head. Acoustic FEA analysis is carried out on these models.

5.1 Digital Image Dataset of Human Head

The goal of this program is to develop an acoustic propagation model that tracks an air-born acoustic wave that is incident on the human head. Thus a human head model built with real human head data is required for finite-element analysis. One of the sources for real human head data is digital image dataset in different modes, such as magnetic resonance images (MRI), computed tomography (CT) images, and anatomical images. There are a few human head image datasets available. For example, National Library of Medicine's (NLM's) Visible Human Project (http:www.nlm.nih.govpubsfactsheetsvisible_human.html) provides complete image dataset for both male and female human body. The Visible Human Male dataset consists of MRI, CT, and anatomical images. Axial MRI images of the head were obtained at 4 mm intervals. The MRI images are 256 pixel by 256 pixel resolution with each pixel having 12 bits of gray scale resolution. The CT data consists of axial CT scans of the entire body taken at 1-mm intervals at a resolution of 512 pixels by 512 pixels with each pixel made up of 12 bits of grey tone. The axial anatomical images are 2048 pixels by 1216 pixels, with each pixel defined by 24 bits of color. The anatomical cross sections are at 1-mm intervals to coincide with the CT axial images. There are 1871 cross-sections for both CT and anatomy. The Visible Human Female dataset has the same characteristics as the The Visible Human Male with one exception, the axial anatomical images were obtained at 0.33-mm intervals. Figure 5.1 shows one sample image of the male human head for each mode.

Based on these 2D human head images, it is possible to reconstruct a detailed 3D

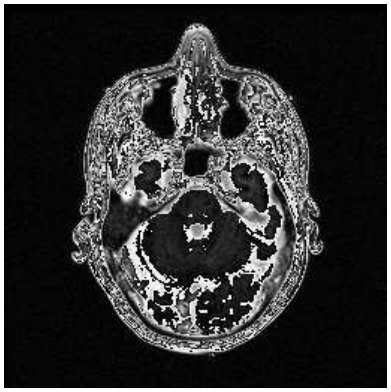

(a) MRI mode

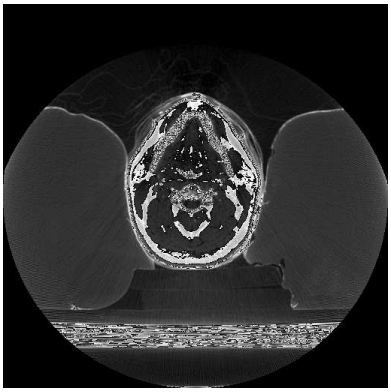

(b) CT mode

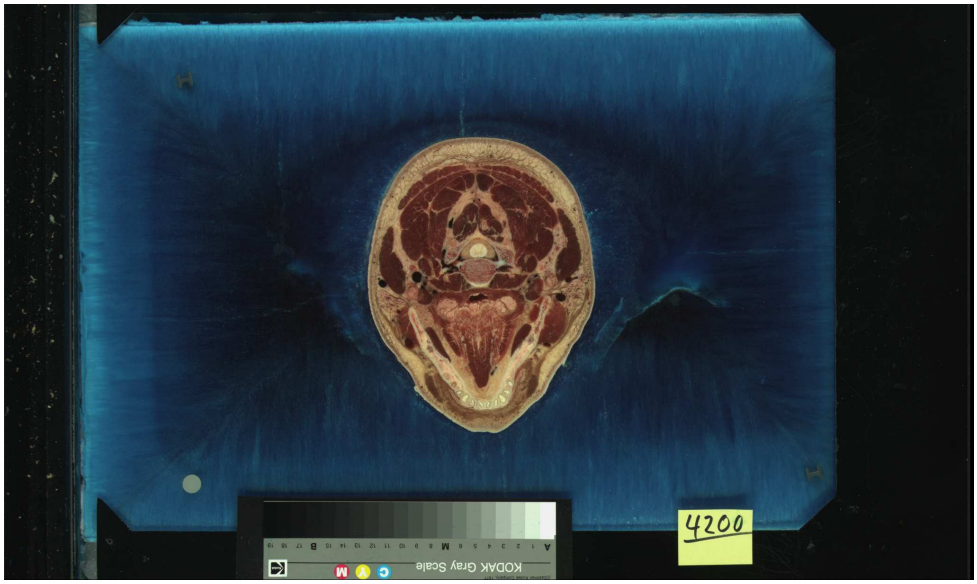

(c) Anatomical mode

Figure 5.1 Two-dimensional medical images of a male human head.

volume model for the human head. This process includes organizing the 2D image files into three-dimensions, using color thresholding to segment different objects within the head volume, such as brain, skin, etc., and generating a head object map. Then the next challenging step is to convert the model to a solid model in a format that can be imported into ANSYS, i.e., IGES (initial graphics exchange specification) format. Developing 3D FEA human head model based on 2D raster image datasets will be described in details later in Section 5.3. Here first a simplified 2D human head FEA model is developed based on the raster image.

5.2 Analysis on Two-Dimensional Human Head

Starting with a contour slice of the 3D human head anatomic image dataset, a simplified 2D human head FEA model is developed to study the wave propagation into and through the head in 2D scenario.

5.2.1 Two-dimensional human head modeling

Figure 5.2(a) shows one trimmed slice from the anatomic image dataset. The problem is simplified by considering the head to consist of two main parts: skull and brain. The head size is approximately 15.01 cm × 20.03 cm. The 2D head geometry model is developed in the following steps which are illustrated in Figure 5.2:

1. Trace the outer contour of the human head using an edge detection technique in Matlab's image processing toolbox (Figure 5.2(b)).

2. The outer contour of human head is converted into IGES format in software MAYA and then imported into ANSYS.

3. Based on the head contour geometry, a skull inner surface is created by simply scaling the outer surface with 1 cm thickness (Figure 5.2(c)).

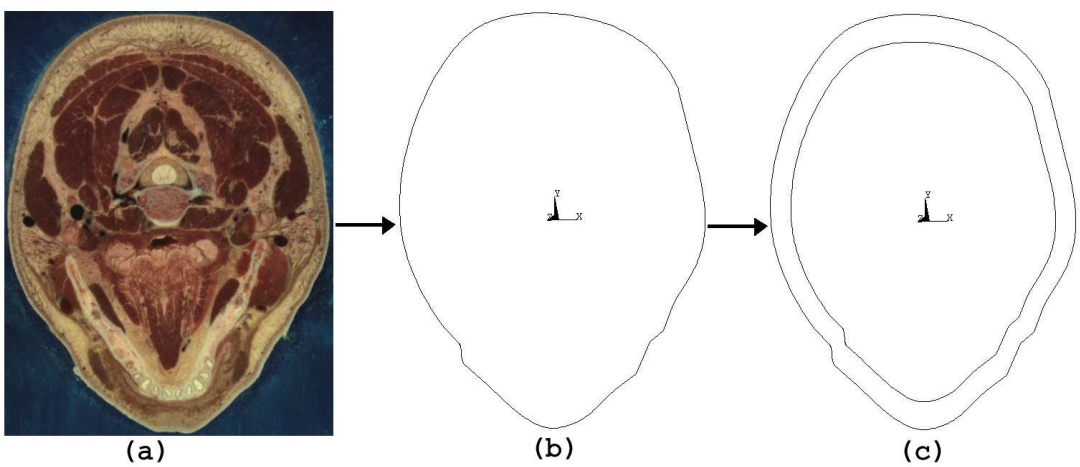

Figure 5.2 Develop two-dimensional geometry model of human head based on anatomic image: (a) original 2D anatomic image, (b) 2D contour of human head, and (c) a simplified 2D human head with skull,

5.2.2 The complete human head computation model

The development of a FEA model for 2D human head follows the basic procedures described in Section 3.1. The simple 2D human head is placed in a circular region filled with homogeneous lossless air. A cycle of sinusoid acoustic wave or an plane wave with certain center frequency is propagating along the x axis. Different elements are used to mesh different region (air, skull, and brain) and the corresponding material properties are assigned to these elements. The basic complete computational model for 2D human head is in Figure 5.3. The material properties used in the FEA model are as follows:

Outer medium: air ($c_{air} = 340$ m/s, $\rho_{air} = 1.2$ kg/m^3)

Inner medium: brain ($c_{brain} = 1500$ m/s, $\rho_{brain} = 1000$ kg/m^3)

Human skull: $\rho_{skull} = 1412$ kg/m^3, $E = 6.5$ GPa, $\sigma = 0.22$, compressive wave speed = 2292.5 m/s, shear wave speed = 1373.5 m/s

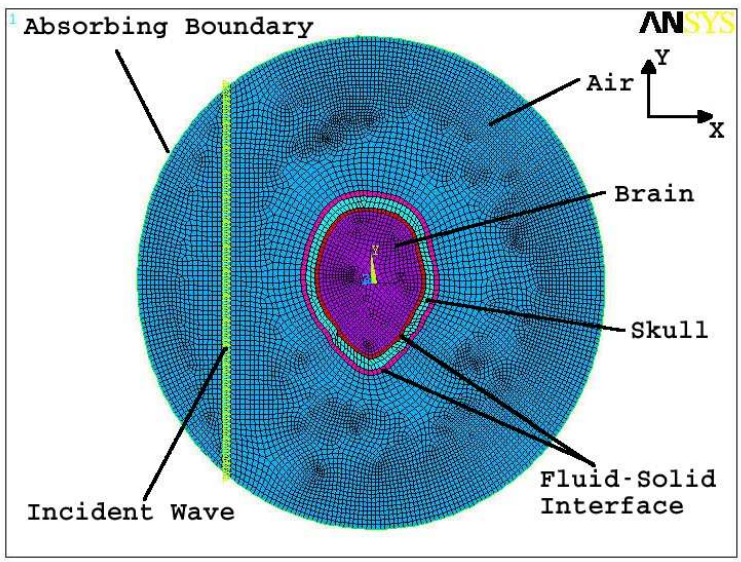

Figure 5.3 Two-dimensional FEA human head model.

Here assume the brain is water-like fluid and the property values for skull come from Sauren and Classens [26].

The other parameters used are the following:

$f = 3$ kHz

$T = 1/f = 0.33$ ms

$lambda_{air} = c_{air}/f$
Head size: $\approx$ 15.8 cm $\times$ 20.2 cm
$X_{inc} = -(0.75 \text{ m} + 0.5\lambda_{air})$
$\varphi_{inc} = 0^o$
$P_{inc} = 1$ Pa
BOUND = 0.75m $+0.9\lambda_{air}$
DPW = 20

5.2.3 Transient acoustic analysis on two-dimensional human head

A series of acoustic analyses with the incident pulse wave at different frequency and different incident angle are conducted on the 2D FEA human head. The parameters for each test are listed in Table 5.1.

Table 5.1 Frequency and incident angle used in transient analysis on 2D human head

Test	Frequency	Incident Angle
1	125 Hz	0°
2	125 Hz	45°
3	1 kHz	0°
4	1 kHz	45°
5	3 kHz	0°
6	3 kHz	45°
7	10 kHz	0°
8	10 kHz	45°

For all tests except Tests 7 and 8, the following general guidelines based on previous experience are followed to develop the FEA model:

1. The incident wave (X_{inc}) is 0.5 λ_{air} away from the target.
2. The absorbing boundary (BOUND) is 0.9 λ_{air} away from the target.
3. The mesh density (DPW) is 20 elements per wavelength in air.
4. The load step size (LSS) is 1/20 T, where $T = 1/f$.
5. The integration step size (ITS) is 1/20 T, where $T = 1/f$.

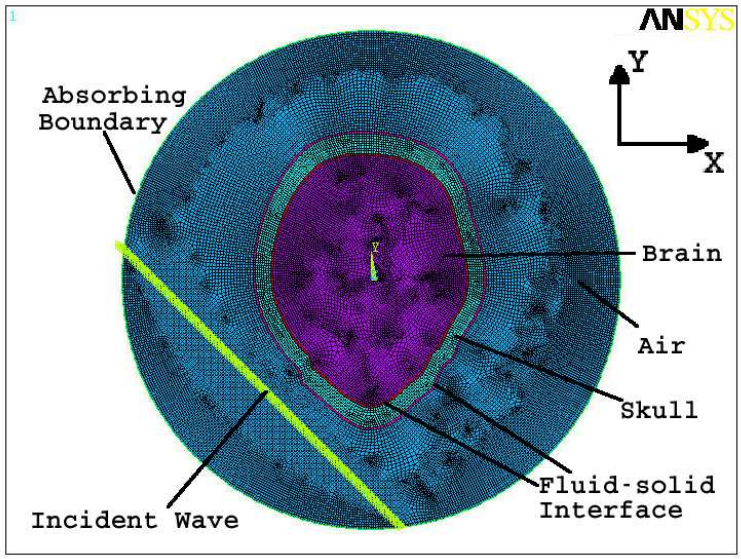

Figure 5.4 Two-dimensional FEA human head model for Test 8 in Table 5.1.

Figure 5.3 shows the FEA model for Test 5, with an incident wave at 3 kHz and an incident angle of 0°. In Tests 7 and 8, the position of incident wave and the absorbing boundary are adjusted to be 1.6 λ_{air} and 3.5 λ_{air}, respectively, away from the target due to the small λ_{air} at 10 kHz. Figure 5.4 shows the FEA model for Test 8 in Table 5.1, with an incident wave of 10 kHz and an incident angle of 45°. Comparing with other models, the FEA model for higher frequency involves larger numbers of elements and thus higher computation cost.

5.2.4 Simulation observations

The simulation results from different tests as listed in Table 5.1 are compared to investigate the effects of incident frequencies and incident angles. Four representative locations in the 2D FEA human head (Figure 5.5) are chosen to compare the pressure and intensity response under different incidence frequency and angle. Positions C and F are along the skull inner surface and positions A and H are about 2 mm away from the skull outer surface in the air medium.

Figure 5.6 plots the acoustic pressure and instantaneous intensity distributions at the four positions (A, C, F, and H) in Test 6 (f = 3 kHz, $\phi_{inc} = 45^o$). Here the instantaneous intensity is calculated using:

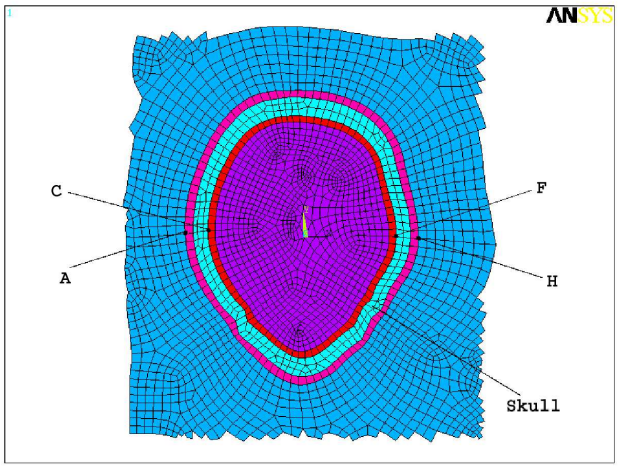

Figure 5.5 Four positions along inner and outer skull surface.

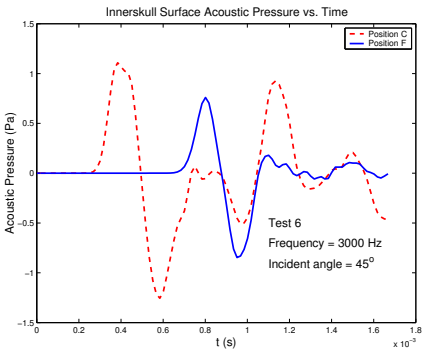

(a): Acoustic Pressure at A&H

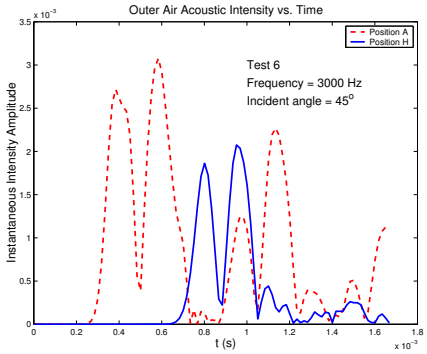

(b): Instantaneous Intensity at A&H

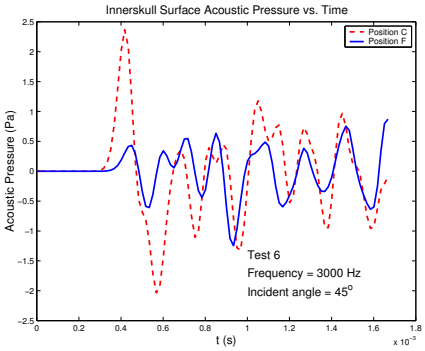

(c): Acoustic Pressure at C&F

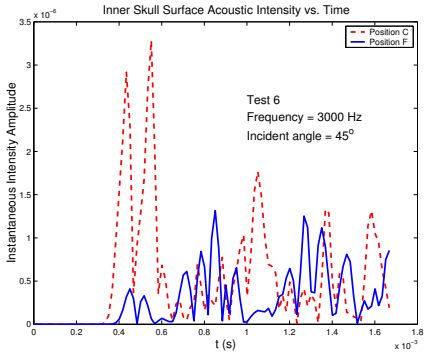

(d): Instantaneous Intensity at C&F

Figure 5.6 Test 6: Acoustic pressure and instantaneous intensity distribution ($f = 3$ kHz, $\phi_{inc} = 45^o$).

$$I_{A,H} = \frac{p(t)^2}{\rho_{air} c_{air}}, I_{C,F} = \frac{p(t)^2}{\rho_{brain} c_{brain}} \tag{5.1}$$

where $p(t)$ is the acoustic pressure, ρ is the fluid density and c is the fluid sound speed.

Validation of the process is accomplished by estimating the acoustic intensity loss across the skull from the instantaneous acoustic pressure waveforms on each side of the skull (one location in air and the other location in water). The acoustic loss across the skull was estimated from

$$dB = 10 \log(\frac{I_{peak,brain}}{\frac{P_{inc}^2}{\rho air c_{air}}}) \tag{5.2}$$

The acoustic loss across the skull analysis is conducted for all the eight tests in Table 5.1. The estimation results are listed in Table 5.2, and the instantaneous intensity distribution at positions (A, C, F, and H) are plotted in Figures 5.7 and 5.8. For all the eight tests, the acoustic loss across the skull is estimated to be 19 $\sim$ 29 dB, reasonably consistent with theoretical estimates (33 dB) considering this is a 2D analysis.

Table 5.2 Acoustic loss across the skull for Test 1-8

Test	Frequency	Incident Angle	Acoustic Loss across the Skull
1	125 Hz	0°	23.62 dB
2	125 Hz	45°	24.62 dB
3	1 kHz	0°	26.31 dB
4	1 kHz	45°	26.67 dB
5	3 kHz	0°	26.32 dB
6	3 kHz	45°	28.73 dB
7	10 kHz	0°	24.89 dB
8	10 kHz	45°	19.26 dB

Comparing the odd number tests and the even number tests, it is observed that it takes longer for the incident wave to propagate to the four locations in the oblique incidence ($\phi_{inc} = 45^o$) than in the normal incidence ($\phi_{inc} = 0^o$), which can be

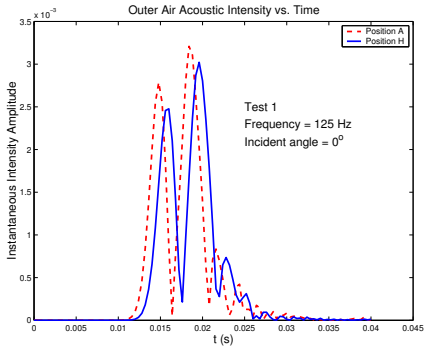

1(a): Instantaneous Intensity at A&H

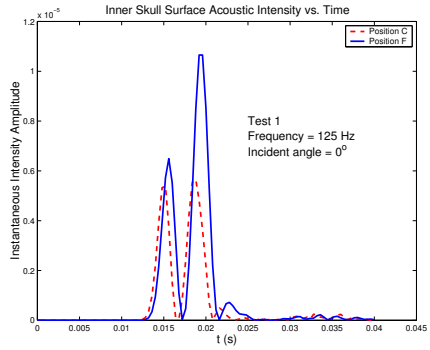

1(b): Instantaneous Intensity at C&F

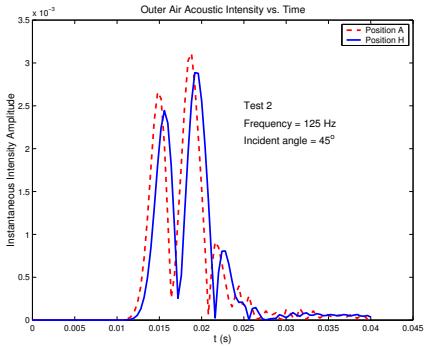

2(a): Instantaneous Intensity at A&H

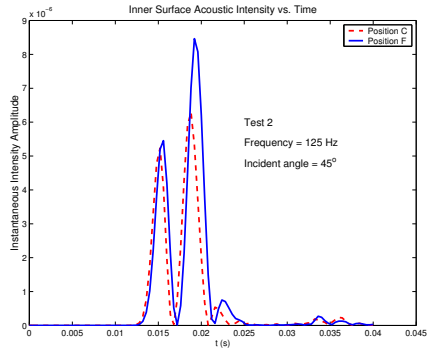

2(b): Instantaneous Intensity at C&F

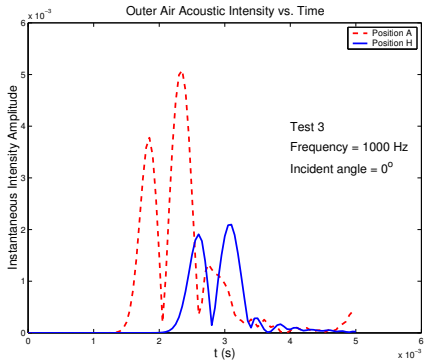

3(a): Instantaneous Intensity at A&H

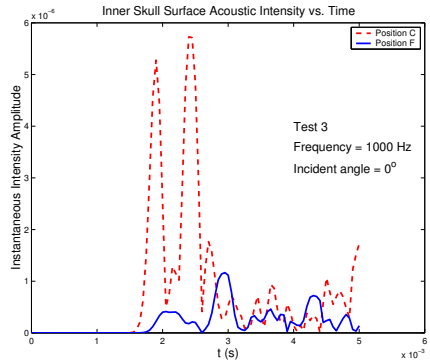

3(b): Instantaneous Intensity at C&F

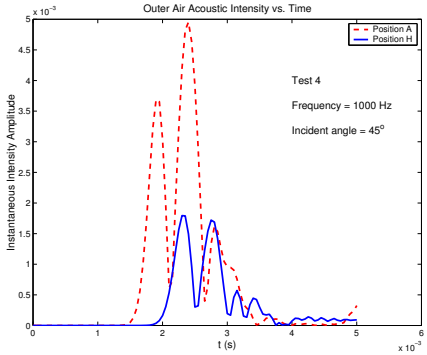

4(a): Instantaneous Intensity at A&H

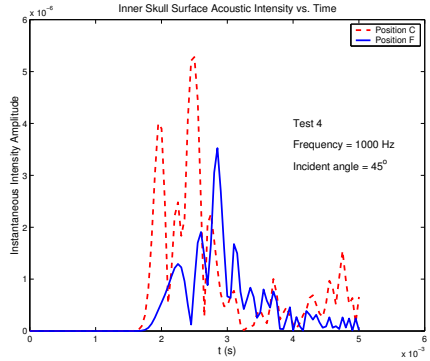

4(b): Instantaneous Intensity at C&F

Figure 5.7 Acoustic instantaneous intensity at A, C, F, and H in Test 1 $\sim$ 4.

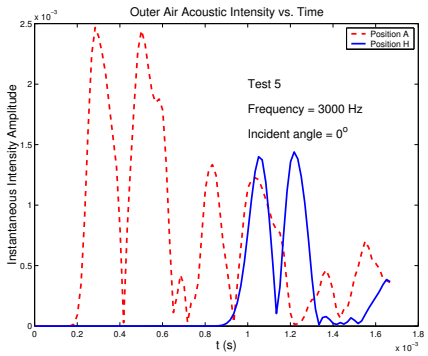

5(a): Instantaneous Intensity at A&H

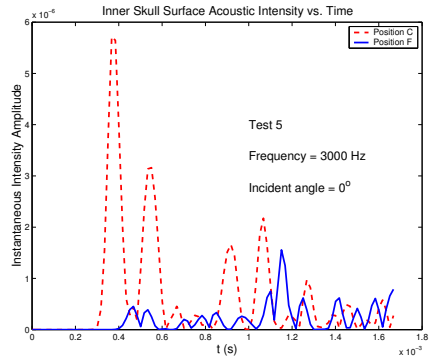

5(b): Instantaneous Intensity at C&F

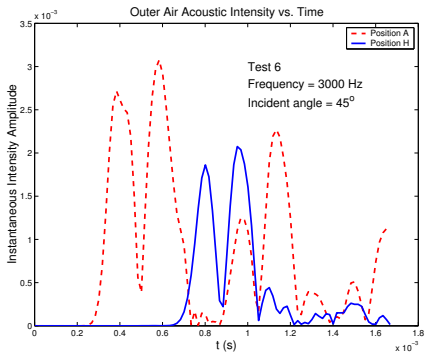

6(a): Instantaneous Intensity at A&H

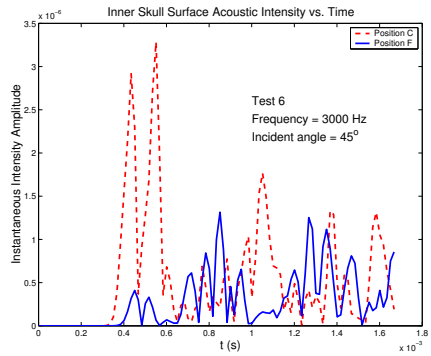

6(b): Instantaneous Intensity at C&F

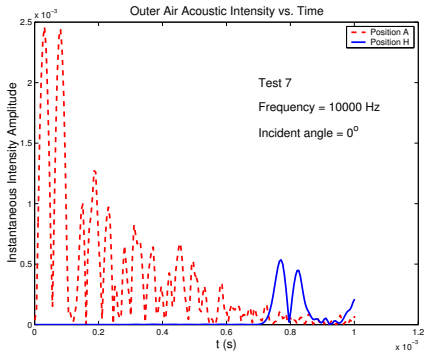

7(a): Instantaneous Intensity at A&H

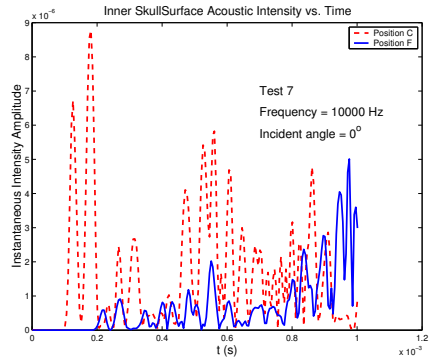

7(b): Instantaneous Intensity at C&F

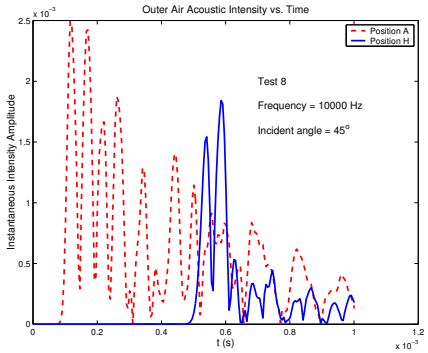

8(a): Instantaneous Intensity at A&H

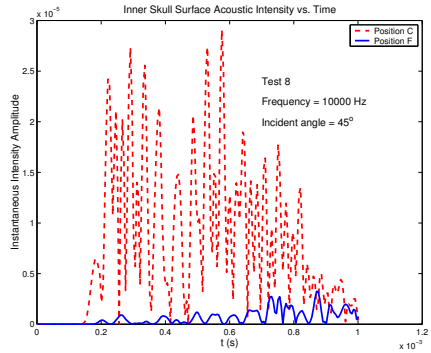

8(b): Instantaneous Intensity at C&F

Figure 5.8 Acoustic instantaneous intensity at A, C, F, and H in Test 5 $\sim$ 8.

explained by the distance difference from the four locations to the incident plane for different incident angles. It is also observed that the incident angle affects the instantaneous intensity level at the four locations although not significantly.

It is also observed that at 125 Hz, the acoustic intensity level does not drop as significantly as in higher frequencies after passing through the head (A vs. H). The explanation is that, at 125 Hz, the wavelength in air is 2.72 m (radius of the head is about 9 cm) and ka is 0.21, in other words, the obstacle is very small compared with the wavelength of the incident wave, thus brings negligible interference wave to the incident wave. Furthermore, at 125 Hz and 10 kHz, the larger instantaneous intensity level is observed inside of the head (C and F). Although it is lack of the physical explanation to this phenomenon at this stage, it agrees with the 125Hz-observation in reality as addressed by the Air Force researchers in Chapter 1 and the greater threshold shift phenomenon produced by the higher frequency noise [3]. All the observations suggest us the incidence frequency plays an important role in noise induced hearing loss.

5.3 Analysis on a Simple Three-Dimensional Human Head

Based on the previous experience, a simple 3D ANSYS FEA model is further developed based on the raster images of human head for conducting acoustic analysis. The finite-element analysis follows the basic procedure described in Chapter 3 and 4. The real challenge for this study is to develop the 3D human head FEA model from the images, which thus will be the focus of this section.

5.3.1 Develop the geometry model

As mentioned earlier, a geometry model in ANSYS refers to a geometric description of the object. There are two steps in this task: build a 3D human head geometric model outside of ANSYS and then import the model into ANSYS.

Build 3D model. ANSYS uses vector data format (such as IGES files) to describe geometries. Two possible approaches were proposed to build a 3D human head geometric model with vector description:

1. Convert a human head digital raster image dataset into a vector format file.

2. Use a 3D scanner to measure real human head geometry and save it in a vector format file.

Attempts have been made using both approaches. The first approach was finally chosen mainly because the human head digital raster image dataset includes complete information of the human head, whereas the 3D scanner only gives the outline shape of the human head. Studying a complete human head is the final goal and thus approach one has been chosen.

A commercial software package (Analyze, Mayo Clinic, Rochester, MN) is used in approach 1. Analyze organizes sets of 2D medical images into 3D volumes for further analysis. Starting from a 2D image datasets, the following steps are implemented in Analyze to build a solid human head model:

1. Organize the 2D image files into 3D volume.

2. Use color thresholding to segment different objects within the head volume, such as brain, skin, etc. A head object map is generated in this step.

3. Use surface modeling to convert volumetric (voxel) data into a set of geometric constructs as a stack of connected, planar line segments (contours). Applying surface modeling on different objects separately will offer a compact description of the object's surface.

4. Save the stack of surface contours of the separate objects to files in .iges format.

The first two steps are very tedious and time consuming. To save time, an available 3D MRI human head dataset in Analyze tutorial is used instead of the NLM dataset for now because this dataset has already been stacked together as a 3D volume of full human head with a simple object map of brain, skin, ventricle, lenticular, and caudate. This model contains MRI images of horizontal 2D slice cuts in 1-mm vertical intervals. The following is the detailed information of this human head dataset:

Width	= 176 mm
Height	= 236 mm
Depth	= 187 mm
Bits Per Pixel	= 8
Bytes Per Pixel	= 1
Bytes Per Image	= 41 536

Pixels Per Image	= 41 536
Voxels Per Volume	= 7 767 232
Maximum Data Value	= 255
Minimum Data Value	= 0
Voxel Depth	= 1 mm
Voxel Height	= 1 mm
Voxel Width	= 1 mm

To keep it simple at the beginning, the first 3D human head is a simple model that does not contain any inside details. Therefore, the intensity of the pixel along the skin surface is chosen as the reference threshold value to extract the outer head contour. The contour is extracted along pixels with same intensity values on the xy (transverse) plane on every single slice of 2D images and then all contours are stacked along the z direction. Figure 5.9 shows the extracted contour on slice 78 and slice 110. The extracted contours are saved to .iges files. In the .iges format, the extracted contours are represented by points and lines. The points correspond to the extracted voxels based on the reference threshold values. The lines describe the connectivity between points. The dimensions are expressed in millimeter because the original voxel size in the MRI images is 1 mm $\times$ 1 mm $\times$ 1 mm.

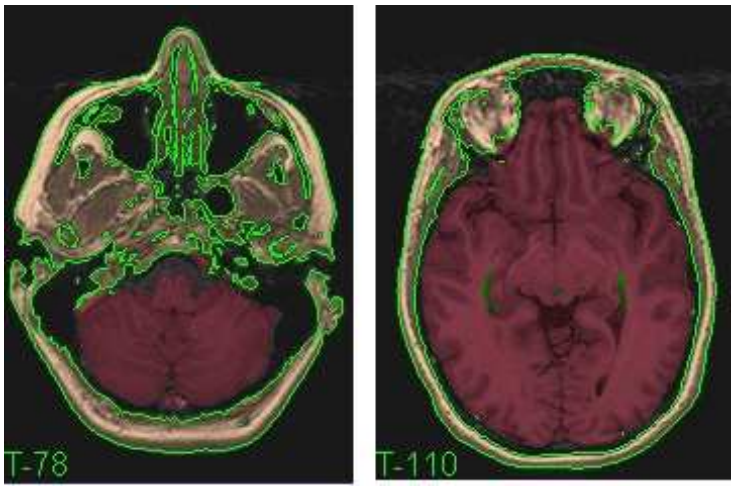

Figure 5.9 Extracted contours on slice 78 and slice 110 on xy (transverse) plane in Analyze.

Import 3D model. The geometric model of a simple human head in .iges format is imported into ANSYS directly. Figure 5.10 shows the original model after being imported into ANSYS (in yz view plane). This model consists of 184 slices of head contours (on xy plane) stacking together and contains a large number of points ($O(10^5)$). Therefore, this model is further simplified in the following steps while maintaining the original outer geometry.

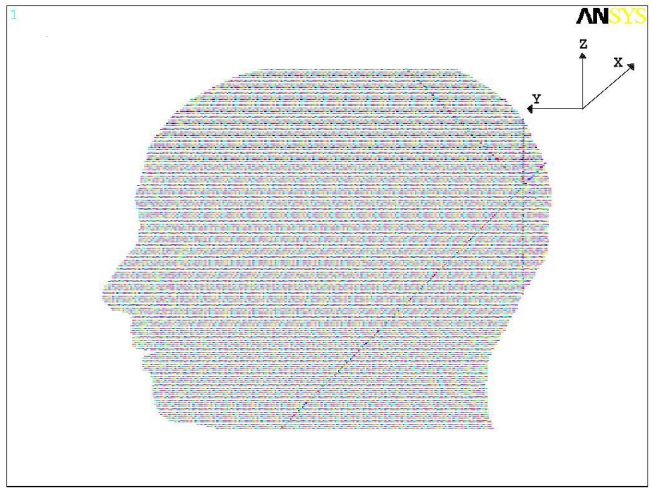

Figure 5.10 The raw head model imported into ANSYS from Analyze.

1. The raw model in Figure 5.10 contains all the 187 slices. By choosing one slice out of every four slices while keeping all the slices around local areas with complicated geometry (e.g., eyes, ears, noses), the number of slices is reduced in Figure 5.11.

2. For each slice, erase the details internal to the outer head contour (Figure 5.12(b) to (c):

3. For each slice, curve fit the points to get a smooth and simplified contour (Figure 5.12(c) to (d)).

4. Further simplify some local areas, such as the areas around ears. To keep the model simple, holes in the ears, noses and eyes areas are filled, for example, ears in Figure 5.13.

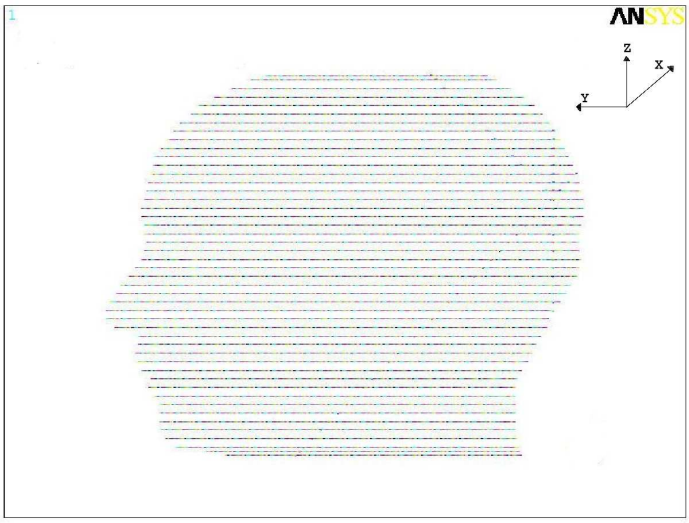

Figure 5.11 A simplified head after step 1.

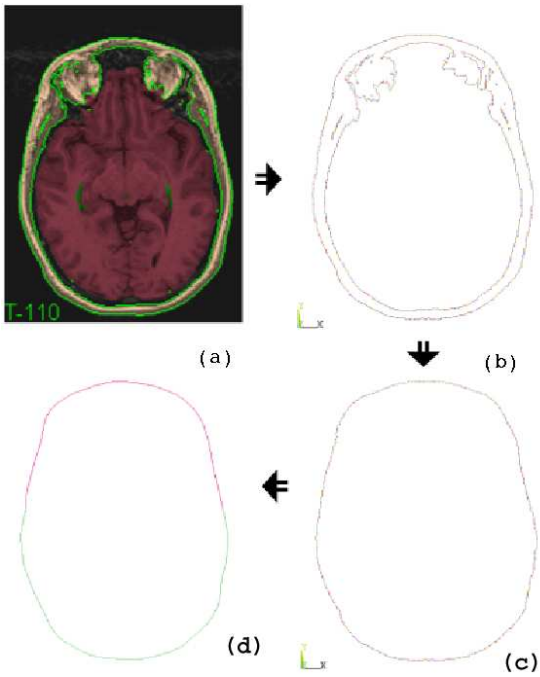

Figure 5.12 An example for slice simplification (Slice 110): (a) original MRI image, (b) contour after thresholding, (c) outer contour only, and (d) smoothed outer contour.

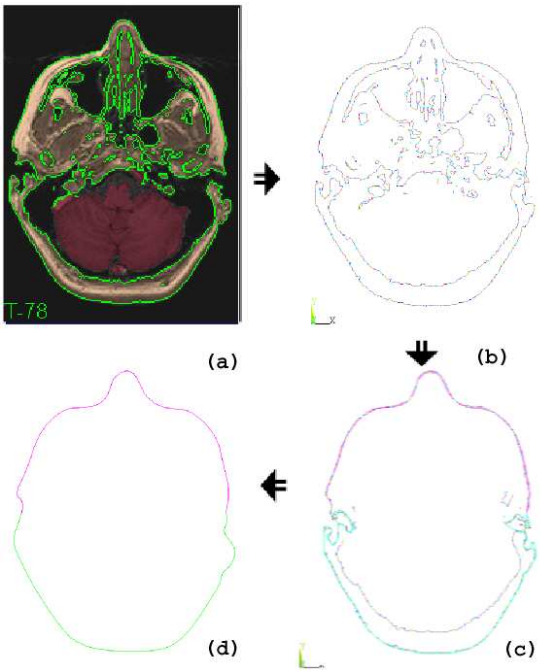

Figure 5.13 Another example for slice simplification (Slice 78): (a) original MRI image, (b) contour after thresholding, (c) outer contour with internal details partially cleaned, and (d) smoothed outer contour with holes filled.

5. Generate head surface areas by "skinning" a surface through specified guiding lines, i.e., the fitted contour curves. These lines which are generated in the previous step act as a set of "ribs" over which a surface is "stretched." The head surfaces are divided into several areas to get smoother surfaces (Figure 5.14).

6. Delete all original points and lines and define the volume surrounded by the surface areas as the solid human head.

The number of entities (points, lines, areas, volumes) now has been greatly reduced from $O(10^5)$ to $O(10)$ while maintaining the original geometry. It should be addressed that this head model does not include any details inside of the human head, and thus, is an unrealistic realization of the human head.

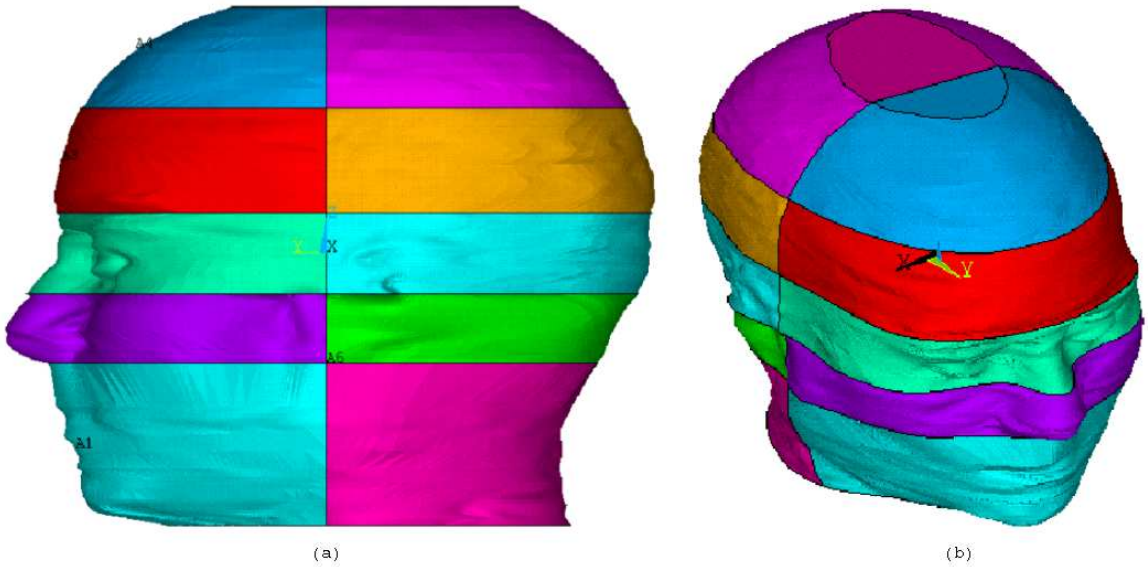

Figure 5.14 A head volume enveloped by the head surfaces: (a) sagittal view, and (b) oblique view.

5.3.2 Develop the FEA model

A complete computational model consists of the 3D human head, the outer medium surrounding the head and the sound wave source. Figure 5.15 shows the complete computational model observed from the -y axis. The human head is located in the center of a spherical domain filled with homogeneous lossless air. In the current model, the absorbing boundary is located about 0.9λ from the human head. The incident sound source is located about 0.5λ to the left of the head and propagates along the $+x$ axis. These numbers are chosen based on the previous experience in 3D harmonic and transient analysis on spheres. The material internal to the outer 3D head surface was constructed of skull material properties to demonstrate that it was feasible to quantify the sound pressure amplitude at a location within the head relative to the air-borne sound pressure amplitude.

The irregular head geometry brings extra complexity to the meshing which is already difficult for 3D scenario due to the limits on the element number and node number of the current ANSYS research version. The mesh quality profoundly affects the computation accuracy and speed; therefore, an appropriate combination of all the meshing factors (element shape, size, straight- or curved-edge, linear or higher

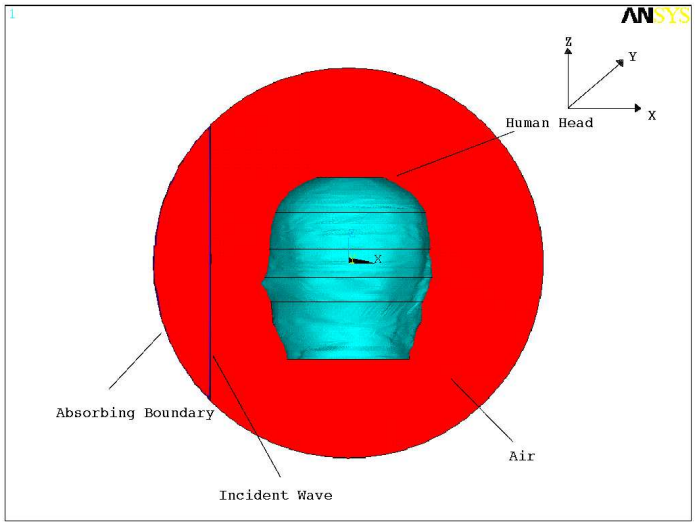

Figure 5.15 The complete computational model for 3D human head.

order, etc.) should be carefully chosen. The following mesh combination for the finite-element model is used:

1. Human head

   - Element type: Solid92, 3D 10-node tetrahedral structural solid element.
   - Element material properties: It is assumed that the head is made of homogeneous skull-like materials. Human skull material properties [26] are assigned to this element: density: 1412 kg/m^3; Young's modulus: 6.5 GPa; Poisson's ratio: 0.22; compressive wave speed: 2292.5 m/s; shear wave speed: 1373.5 m/s.
   - Element size: The shape of the real human head is far from a regular geometry shape. Some regions of the head volume are easy to divide into regular shapes and thus easily meshable parts, and other regions are geometrically complex. Thus, different mesh sizes are used for different regions of the human head to avoid poor mesh qualities and unsuccessful meshing. Denser meshes are used for those high-gradient regions such as the nose and ears to capture details while for other less critical regions, such as the interior head, which is away from the skull boundary, coarse

meshes are used. SmartSizing controlled by the SMRTSIZE command in ANSYS is used here to create reasonably shaped elements during automatic mesh generation. This specific meshing method first computes estimated element edge lengths for all lines in the areas or volumes being meshed and the edge lengths on these lines are then refined for curvature and proximity of features in the geometry. Figure 5.16 shows the meshed human head.

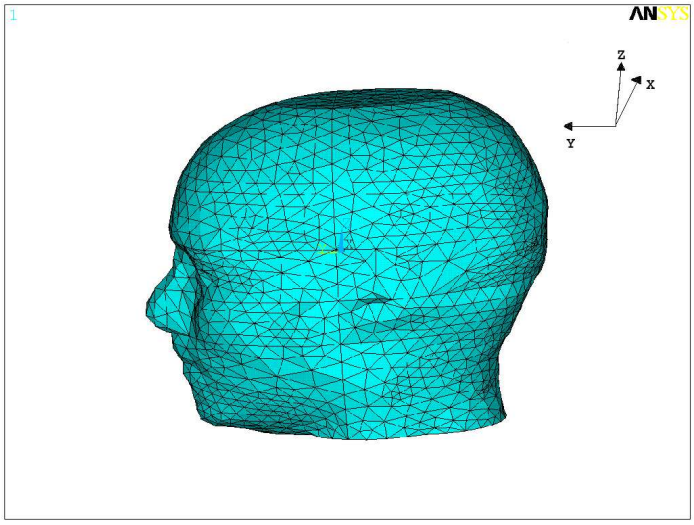

Figure 5.16 Human head meshed with SOLID92 using SmartSizing in ANSYS.

2. Surrounding medium

- Element type: Fluid 30, 3D acoustic fluid element.
- Element material properties: It is assumed that the head is surrounded by homogeneous and lossless air. The material properties of air are assigned to this element: speed: 340 m/s; density: 1.2 kg/m^3.
- Element size: Again the SMRTSIZE function in ANSYS is used to get high quality meshes which can capture the complicated geometry shape along the air-head interface. Figure 5.17 shows the surface meshes on the air sphere boundary.

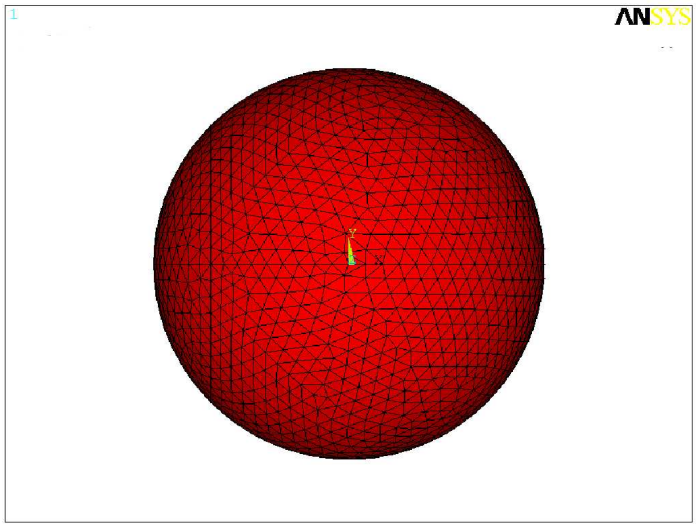

Figure 5.17 Surrounding fluid medium meshed with FLUID30.

3. Absorbing boundary

   - Element type: Fluid 130, 3D infinite acoustic element.
   - Element material properties: The material properties of air are assigned to this element: speed: 340 m/s; density: 1.2 kg/m^3.
   - Element Size: The absorbing boundary meshes are generated along all the nodes located on the absorbing boundary. It satisfies 10 elements every wavelength.

5.3.3 Three-dimensional transient analysis

After discretizing the 3D computational model with a simple human head submerged in the air medium, transient acoustic analyses are conducted. The parameters used are as follows:

$f = 3$ kHz

$T = 1/f = 0.33$ ms

Outer medium (air): $c = 340$ m/s, $\rho = 1.2$ kg/m^3, $\lambda_{air} = 340/3000 = 0.113$ m

Head: $\rho = 1412$ kg/m^3, Young's modulus = 6.5 GPa, Poisson's ratio = 0.22, compressive wave speed = 2292.5 m/s, shear wave speed = 1373.5 m/s

Head diameter: ≈ 0.18 m

Absorbing boundary radius (BOUND) = 0.09 m $+0.9\lambda_{air}$ = 0.1920 m;

$X_{inc} = -(0.09 \text{ m} + 0.5\lambda_{air}) = -0.1467$ m

$\phi_{inc} = 0^o$

$P_{inc} = 1$ Pa

LSS = ITS = 1/20 T

Computation length = 10 T = 3.3 ms

To include the coupling between the fluid and structure, a fluid-structure interface (FSI) constraint is applied at the fluid element faces on the human head surface (Figure 5.18). This interface couples the structural motion and fluid pressure at the interface and thus produces unsymmetrical element matrices.

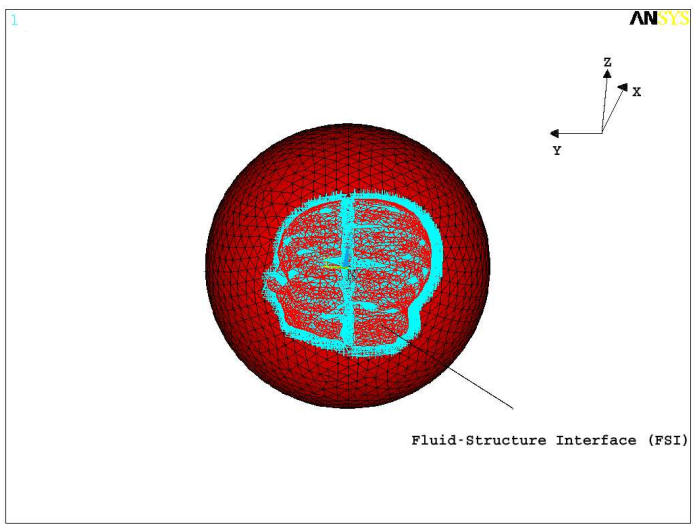

Figure 5.18 Apply FSI flag on the human head surface.

A one-cycle pulse wave with a center frequency of 3 kHz is excited on the nodes located on a plane perpendicular to the x axis (as indicated in Figure 5.15). The pulse wave propagates along $+x$ axis.

In the current model, the head is completely made of skull material and it is subjected to displacement and deformation under the incidence of the acoustic wave. Figure 5.19 shows the acoustic pressure distribution on the head surface at time step 1, 9, 14, 18, 25, and 29, respectively (step size = 1/20 T). The incident wave is excited on the plane which is 0.5λ away from the head along -x axis. Therefore, it

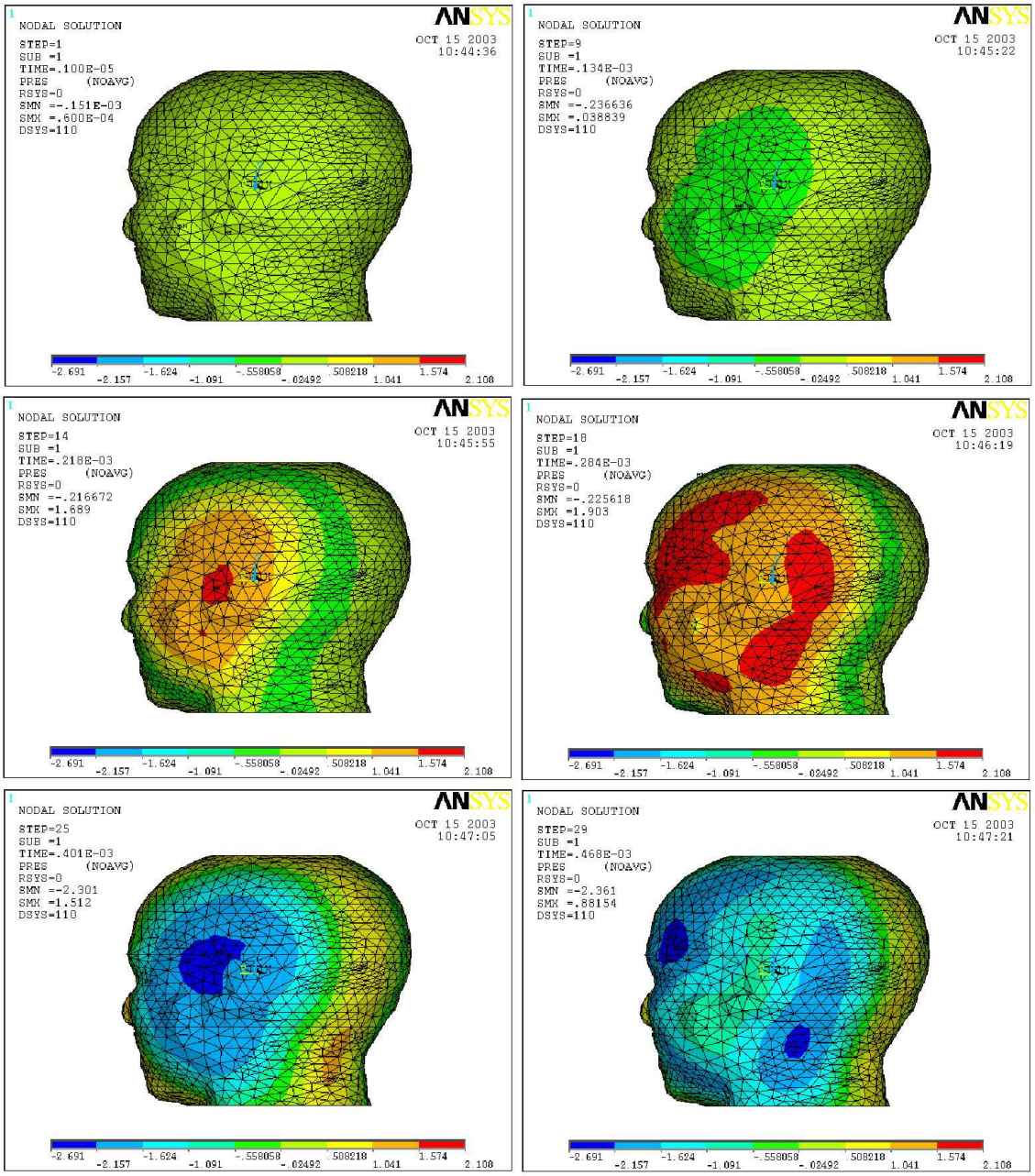

Figure 5.19 Acoustic pressure distribution on the three-dimensional rigid head surface.

takes about 10 time steps to reach the head and then propagate into the head. For the human head case, there are no theoretical solutions or experimental results for the complete pressure distribution on the head surface. These pressure contour plots

are the possible tools for visualization in the 3D scenario although they do not convey any information inside of the head.

Admittedly this is an unrealistic realization of the head but one that can be evaluated in three dimensions and allows for the evaluation quantitatively of propagation into skull material. Acoustic pressure waveforms were obtained at three locations (Figure 5.20). Location A on the incident plane, location B on the interface of air-head and location C on the other inside of human head. The instantaneous acoustic intensity peak (Eq. (4.1); Section 4.5) in air was determined to be about 2.7 mW/m^2 and the acoustic intensity in the skull bone was about 1.24 μW/m^2. The acoustic loss (Eq. (4.2); Section 4.5) across the 3D skull model surface was estimated to be approximately 32 dB, quite consistent with theoretical estimates (33 dB).

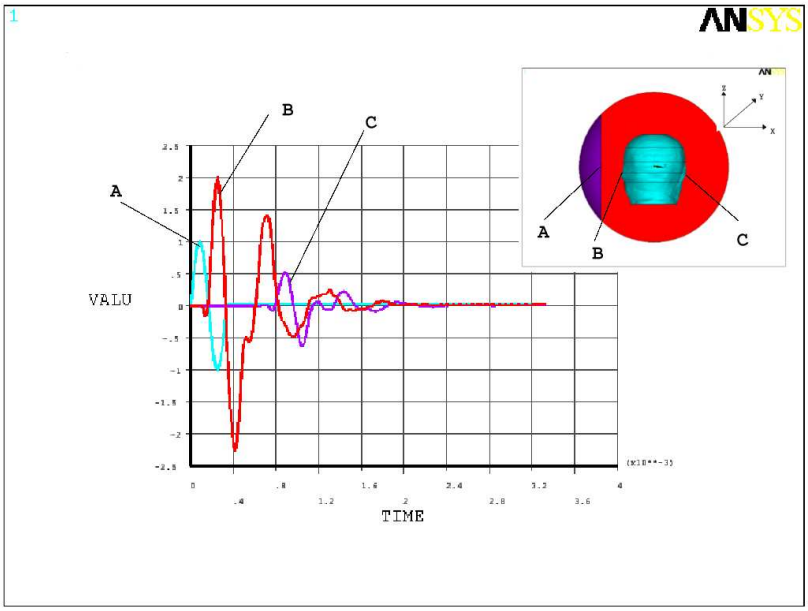

Figure 5.20 Acoustic pressure waveforms at three selected locations for the 3D FEA human head model.

5.4 Summary

In this chapter, a simplified 2D FEA human head model was constructed based on the NIH human head digital raster image dataset. Transient (one-cycle sine

wave) analyses were performed at four frequencies (0.125, 1, 3, and 10 kHz) and two incident angles (0°: toward the right side, and 45°: approximately toward the right cheek). Instantaneous acoustic pressure waveforms were recorded at 4 locations: at approximately the left and right ear locations near each side of the skull. Validation of the process was accomplished by estimating the acoustic intensity loss across the skull from the instantaneous acoustic pressure waveforms on each side of the skull (one location in air and the other location in water). Furthermore, an unrealistic 3D human head model was constructed to serves as a preliminary attempt to develop a 3D human head model based on real human head image dataset and then conduct acoustic analysis on the developed 3D head model.

CHAPTER 6

PROPAGATION PATH EVALUATION BASED ON FEA RESULTS

In previous chapters, it was demonstrated that it is feasible to develop a 3D FEA human model based on real digital image database and conduct ANSYS acoustic analysis on the model to propagate an air-borne acoustic wave around and into the human head. The pressure/intensity waveforms were plotted and compared which provide quantitative information. In order to better represent a 3D process graphically or quantitatively or both, a ray tracing approach to represent graphically and quantitatively a 3D transient process has been developed using a hemisphere model, for which the theoretical solutions are available for validation purposes.

6.1 Introduction to Ray Tracing

Ray tracing is a common procedure by which wave propagation is displayed. For example, in the study of optics, rays are used to depict the path or paths taken as a light wave travels through a lens. However, in optics, the eikonal equation can be solved because the wavelength is assumed to be zero so that propagation laws can be formulated in terms of geometry. This is also the case for geometric acoustics and is often used to solve acoustic propagation problems in the ocean [1]. However, for the case of an acoustic wave that has a wavelength comparable to the object onto which it is incident, the full wave equation must be solved because diffraction needs to be included as part of the analysis [35]. Therefore, ray paths need to be deduced from the propagated acoustic wavefront. The transient ANSYS FEA procedure yields data from which the propagated acoustic wavefront has been deduced. From the propagated acoustic wavefront, rays have been calculated by taking the normal components of the wavefront surface as a function of time. The transient FEA procedure yields data as a function of time steps, thus allowing the wavefront to be animated as a function of time. Also, from these data, as long as

the time steps are sufficiently small, ray paths can be calculated. Further, after the ray paths have been calculated, the acoustic energy can be determined from the density (number of ray paths that intersect a unit volume) of ray paths in a particular volume [36].

6.2 Hemisphere FEA Model

In this study, a hemisphere is submerged in a homogeneous lossless fluid medium and is under the incidence of a one-cycle sinusoid wave. The hemisphere and outer medium are made of fluid with different sound speed but with the same density. The shear wave is not supported in this case to minimize the problem complexity. Element size of 1/20 wavelength is used and time step size of 1/100 period is used. Figure 6.1 shows the computational model. The parameters used are:

$f = 3$ kHz

$T = 1/f = 0.33$ ms

Half-sphere radius $a = 0.09$ m

Outer medium (air): $c = 340$ m/s, $\rho = 1.2$ kg/m^3

Hemisphere: $c = 1540$ m/s, $\rho = 1.2$ kg/m^3

$\lambda = c_{outermedium}/f$

$X_{inc} = -(a + 0.5\lambda)$

$\varphi_{inc} = 0^o$

$P_{inc} = 1$ Pa

BOUND $= a + 0.9\lambda$

ITS $= 1/100\ T$

Computation length $= 2\ T$

6.3 Wavefront Reconstruction via Time-Domain Correlation

Following the basic procedure for transient analysis the FEA model is solved. The pressure distribution is calculated at each time step at each node in the model, and thus, the complete pressure waveform of the computation length is available for each node. Based on the computed nodal solution, the wavefront is reconstructed via time-domain correlation technique.

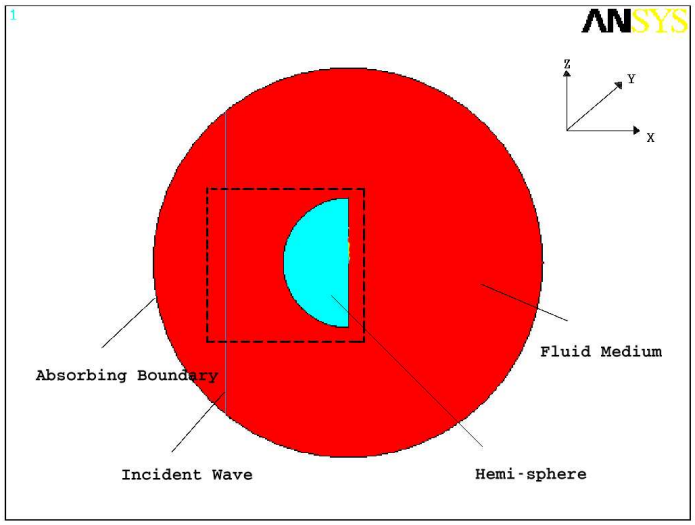

Figure 6.1 A simple hemisphere FEA model.

The time-domain correlation technique can be conceptually viewed in the following way: Assuming the fluid medium is homogeneous and at rest, the wavefronts move along the propagation direction with the speed of sound of the medium. At time $t = 0$, a cycle of sine wave is excited at the incident plane x_{inc}, and at time $t = t_0 + N \times \triangle t$, the wave is propagated to a new position x, where N is the time step and $\triangle t$ is the time step size, $\triangle t = T/100$ in this case. The wavefront is defined as "any moving surface along which a waveform feature is being simultaneously received" ([35], p. 371). According to this definition, the nodes at which the incident wave arrives at the same time step N form the wavefront at that time step. To find out at which time step the incident wave arrives at a node, the computed FEA pressure waveform is compared with a reference waveform, which is shifted by $t = t_0 + N \times \triangle t, 0 \leq N \leq L$ from the incident waveform (Figure 6.2), where L is the total number of time step computed, $L = 200$ in this case. Each reference waveform represents the waveform that the incident wave travels to after a time period of $N\triangle t$. The degree of similarity between the computed waveform and the reference waveform is assessed from the correlation of the two waveforms. If the waveforms at two nodes are maximally correlated to the same reference waveform which is shifted in time by $t = t_0 + N \times \triangle t$ from the incident wave, the wavefront reaches these two nodes at

the same time step N. As in Figure 6.3 the correlation coefficients for two nodes are plotted versus time shift of the reference waveform. The waveform for both nodes are maximally correlated to the reference waveform shifted by $67\triangle t$ from the incident waveform. Therefore, the wavefront reaches these two nodes at time step 67.

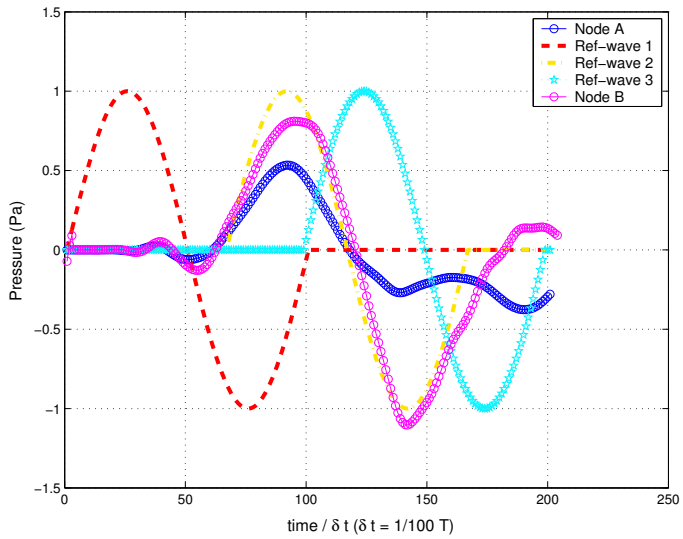

Figure 6.2 Pressure waveforms at two arbitrary nodes and the reference pressure waveforms.

Using this technique, the nodes on the same wavefront are found at each time step. By 3D interpolation of the position of these nodes the wavefront surface is reconstructed. To exclude the errors caused by the spherical absorbing boundary, the wavefront reconstruction region is further limited to a local center region as framed in Figure 6.1 ($X_{inc} \leq x \leq 0$, -0.1 $m \leq y \leq 0.1$ m, -0.1 $m \leq z \leq 0.1$ m). Furthermore, only the first 100 time steps are simulated to exclude the reflected wave from the other surface of the hemisphere. Figure 6.4 shows the wavefront surface reconstructed from the FEA data at different time step. To keep the figure readable, only wavefronts at selected time steps are shown.

6.4 Ray Tracing

Assuming that the time step size is small enough (1/100 T in this case), ray paths from one wavefront are along the normal direction of the wavefront surface, and reach the next wavefront without changing directions. Continuously connecting

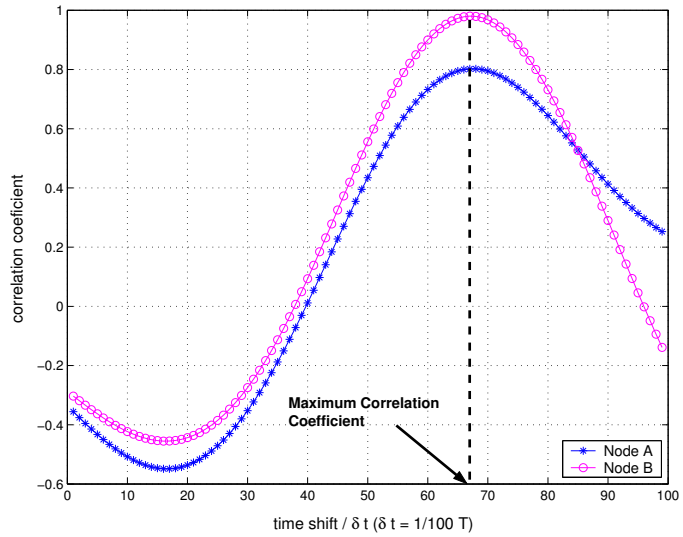

Figure 6.3 Time-domain correlation coefficients at two arbitrary nodes

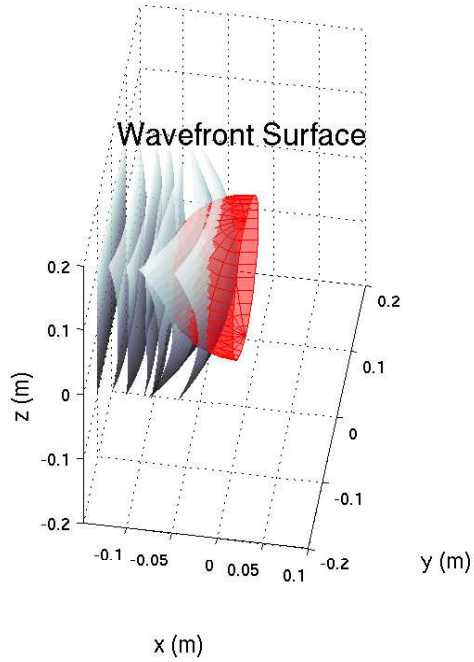

Figure 6.4 Reconstructed wavefront via time-domain correlation technique.

the ray paths from wavefront to wavefront, the complete ray paths are traced. The reconstructed ray paths in this study are plotted from two different angles of view in Figures 6.5.

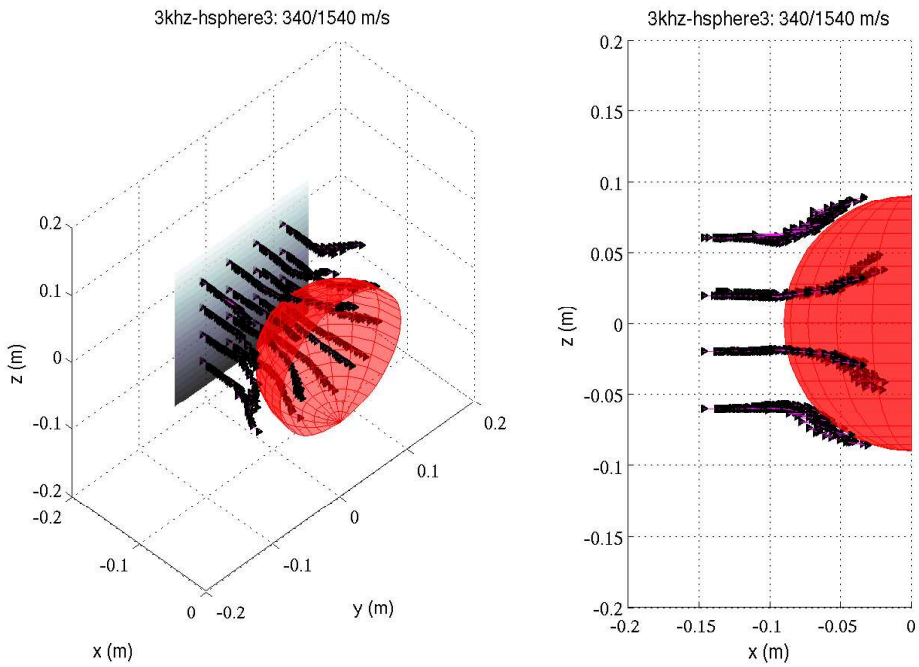

(a): 3D view (b): X-Z view

Figure 6.5 Ray paths in different view.

6.5 Method Evaluation

The ray paths originated in air and propagated into the hemisphere. Knowing the sound speed in the two different medium and the size of hemisphere, the ray tracing can be solved using theoretical solutions. Before the sound wave reaches the hemisphere, the ray is parallel to the propagation direction, $+x$ axis in this case. When the ray hits the hemisphere, the direction of the transmitted ray can be calculated using the Snell's law:

$$\frac{c_1}{\sin\theta_i} = \frac{c_2}{\sin\theta_t} \tag{6.1}$$

where c_1 is the sound speed in the outer medium and c_2 is the sound speed in the hemisphere.

Figure 6.6 plots selected ray paths both calculated theoretically and traced based on the FEA solution. Comparing the simulation results and the theoretical solutions, $0.7^o \sim 10^o$ difference is found for low-angle incidence. As the angle of incidence onto the hemisphere increased, the ray path directions into the hemisphere become progressively greater than the theoretical calculation.

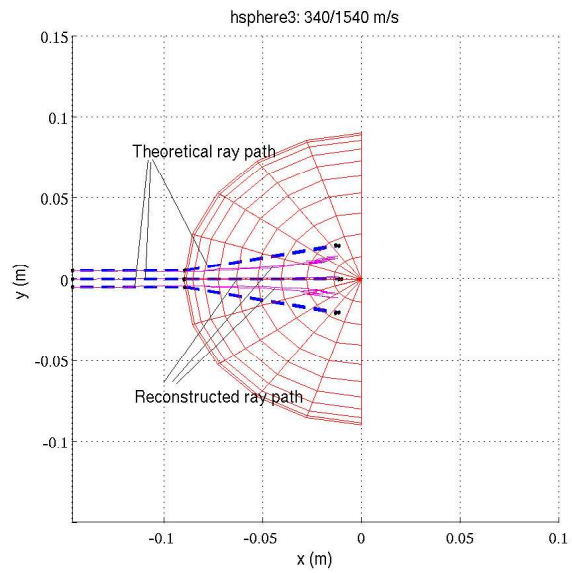

Figure 6.6 Ray paths for Hsph-3 model.

There are several possible reasons for this problem. First, diffraction phenomenon could exist because, in this case study, the wavelength in air is 11.3 cm and ka is 5.0 (radius of the hemisphere is 9 cm) based on a center frequency of 3 kHz but the frequency content of the one-cycle wave is much broader. To test the diffraction hypothesis, the transient ANSYS FEA procedure at 10 kHz is performed using the same hemisphere. However, at the high frequency of 10 kHz, the current ANSYS version limits on elements/nodes number are hit and a very coarse meshing is used in the FEA model that greatly compromised the computation accuracy.

Secondly, computational errors existing in both the 3D FEA and wavefront reconstruction process could also be causing the disagreement. As for FEA analysis, computational errors have been found in previous 3D validation studies (Section 3.4, 3.5). As for the ray tracing procedure, currently only the FEA nodal solutions are used, and thus the discontinuity between adjacent elements caused

by the gradient across elements is not addressed, which produces inaccuracy in wavefront reconstruction. The computational errors in the FEA analysis are further accumulated when the FEA solutions are used in the ray tracing process.

6.6 Summary

In this chapter, a ray tracing approach is developed and evaluated to graphically and quantitatively represent a 3D transient process. Disagreement with the theoretical calcualation is found, and the reasons that could cause the disagreement is analyzed, which suggests further evaluation and improvement on the current method are needed.

CHAPTER 7
DISCUSSION

In this chapter, the work presented in this thesis is summarized and then the recommendations regarding further development are provided.

7.1 Summary of the Current Work

Scientific researchers have shown great interest in noise-induced hearing loss (NIHL) for more than half century. People actively seek efficient hearing protective devices (HPDs) to prevent NIHL. The existence of NIHL even with HPDs implies that alternative propagation paths to the organ of Corti may exist other than the normal acoustic propagation path through the auditory canal to the organ of Corti. This project aims at studying the propagation of an airborne incident acoustic wave around and in the human head using finite-element analysis (FEA), which can serve as a computational tool to elucidate the acoustic wave propagation around, into and in the human head. Specifically, the model then determines two features: (1) alternate acoustic propagation paths to the cochlear shell that exist besides the normal air-borne acoustic propagation path (eardrum-ossical path) through the auditory canal to the cochlea and (2) quantify the sound pressure amplitude in the cochlear shell relative to the air-borne sound pressure amplitude.

Significant progress has been made toward accomplishing the goals of this project. The ANSYS FEA general processing code (ANSYS, Inc., Canonsburg, PA) for both harmonic and transient solutions has been validated using well-understood 2D and 3D models. Harmonic (continuous-wave) validation studies were conducted for (1) 2D rigid cylinders, (2) 3D rigid spheres and (3) 3D elastic spheres. Transient (one-cycle sine wave) validation studies were conducted for (1) 2D rigid cylinders, (2) 2D elastic shell cylinders, and (3) 3D water spheres. For all of the validation studies, either a harmonic or transient acoustic plane wave was initiated in air. The air-borne acoustic wave was incident on the geometric model that was either rigid, elastic or water.

Water is an ideal fluid for this study because it has acoustic propagation properties similar to those of brain and other soft tissues. In all cases, the computational solutions of acoustic pressure distribution agreed well with the analytic solutions of acoustic pressure distribution.

The transient FE analyses of the 2D NIH human head (National Library of Medicine's Visible Human Project, National Institutes of Health, Bethesda, MD) have been constructed, simplified and verified. The male anatomic dataset was used. The anatomic dataset consists of 0.33-mm-wide transverse sections of the head, with each section 2048 pixels by 1216 pixels and each pixel 8-bit RGB scale. A simplified 2D human head analysis was conducted using one of the 0.33-mm-wide transverse sections. A simplified 2D human head analysis was conducted using one of the 4-mm-wide transverse sections. The first challenge (computational, not scientific) was to convert the NIH human head digital raster image dataset into a vector format file for import to ANSYS that uses IGES-format vector data. Then the outer surface of the head was segmented to yield only the head contour. Skull was modeled as a 1-cm-thick layer immediately inside the human head contour. The interior region was modeled as water. Transient (one-cycle sine wave) analyses were performed at four frequencies (0.125, 1, 3, and 10 kHz) and two incident angles (0°: towards the right side, and 45°: approximately towards the right cheek). Instantaneous acoustic pressure waveforms were recorded at four locations: at approximately the left and right ear locations near each side of the skull. Validation of the process was accomplished by estimating the acoustic intensity loss across the skull from the instantaneous acoustic pressure waveforms on each side of the skull (one location in air and the other location in water). The acoustic loss across the 2D skull was estimated from the FEA data to be approximately 26 dB, reasonably consistent with theoretical estimates (33 dB).

The transient FE analyses of a 3D human head model derived from a 3D Analyze MRI head model (Mayo Clinic, Rochester, MN) has also been demonstrated. The Analyze human head was constructed of skull material properties to demonstrate that it was feasible to quantify the sound pressure amplitude at a location within the head relative to the air-borne sound pressure amplitude. The Analyze human head model contains a large number of points ($O(10^5)$). Therefore, this model was segmented and simplified ($O(10)$) while maintaining the original outer geometry; the head was modeled as skull material. Admittedly this is an unrealistic realization

of the head but one that can be evaluated in three dimensions and allows for the evaluation quantitatively of propagation into skull material. A transient (3-kHz one-cycle) sine wave was incident from air onto the simpler human head model. The acoustic loss across the 3D skull model surface was estimated from the FEA data to be approximately 32 dB, quite consistent with theoretical estimates (33 dB).

A ray tracing approach to represent graphically and quantitatively a 3D transient process has been developed. The full wave equation is solved in the finite-element analysis and from the computed results the propagated acoustic wavefront has been deduced from a time-domain correlation technique. From the propagated acoustic wavefront, rays have been calculated by taking the normal components of the wavefront surface as a function of time. With the assumption that the time steps are sufficiently small, ray paths are calculated. The ray tracing approach has been evaluated using a 9-cm-radius hemisphere of known propagation speeds. The ray paths originated in air and propagated into the hemisphere. For low-angle incidence, the ray path directions into the hemisphere were consistent with those calculated from Snell's law. However, as the angle of incidence onto the hemisphere increased, the ray path directions into the hemisphere became progressively greater from those expected from a Snell's law calculation.

In summary, we have (1) validated finite-element analysis (FEA) general processing code for both harmonic and transient solutions, (2) constructed, simplified and verified transient FEA analyses of the 2D NIH human head, (3) demonstrated FEA analysis of the 3D Analyze human head, and (4) developed a ray tracing approach to graphically and quantitatively represent a 3D transient process.

7.2 Challenges and Suggestions for Future Work

Through the studies that have been done, a lot of challenges are observed in various areas and thus bring the extension of this project.

7.2.1 Modeling of a detailed three-dimensional human head

In the previous work described in Chapter 5, it has been demonstrated that it is possible to segment the contour of human head and develop a simple 3D head model based on 2D MRI images using Analyze, a software distributed by Mayo Clinic. In the next stage of building a detailed head model, the three types of NLM human head

data (MRI, CT, and anatomic) from the same subject will be used. Different objects in the head can be developed separately using one of the three types of images and then combined into a complete 3D head model with careful alignment. For example, CT images will be used to develop the skull bone model, MRI images will be used to develop the skin and brain model, and anatomic images will be used to develop the detailed auditory system. Overall, it is expected to result in even larger model containing spatially decimated points from processing the original medical images. Furthermore, it will be even more difficult than before to manage the decimated model into a manageable surfaces and volumes for FEA while retaining a good geometric representation. Therefore, the development of a complete and realistic 3D human head FEA model based on the head medical image dataset will be a very challenging but must-do task in the future. It involves both advanced image-processing and solid modeling techniques. Preliminary efforts have been made towards this goal with the aid of a sophisticated software for 3D visualization and volume modeling, AMIRA. AMIRA not only provides more advanced features required for visualization, segmentation and volume modeling of 3D medical image data than Analyze, but also is able to generate a corresponding volumetric tetrahedral grids suitable for advanced 3D finite-element simulations. In addition, the quality of the resulting mesh, according to measures common in finite element analysis, can be controlled. So far the author has successfully imported a set of surface meshes of a human skull bone generated in AMIRA to ANSYS (Figure 7.1) through format conversion in AUTODESK (an AutoCad product). However, more modeling work still needs to be done before conducting FEA on this model.

7.2.2 Improve the computational accuracy

The accuracy and precision of the FEA are directly depending on the mesh qualities of the FEA model. In general, the element size of 1/20 of the wavelength ($\lambda/20$) in the corresponding medium is the minimum requirement to resolve the wave propagation in the corresponding material. The current NCSA ANSYS license (Version 8.0, university advanced) has the node limit of 128 000 and the element limit of 128 000. In the 3D scenario, such as case studies in Section 3.4, 3.5, 4.5, and 5.3, it is found that the element and node limits of ANSYS are easily exceeded and the basic mesh requirements for acoustic analysis can not be satisfied. This physical challenge degraded the computational accuracy as founded in Section 3.4 and 3.5.

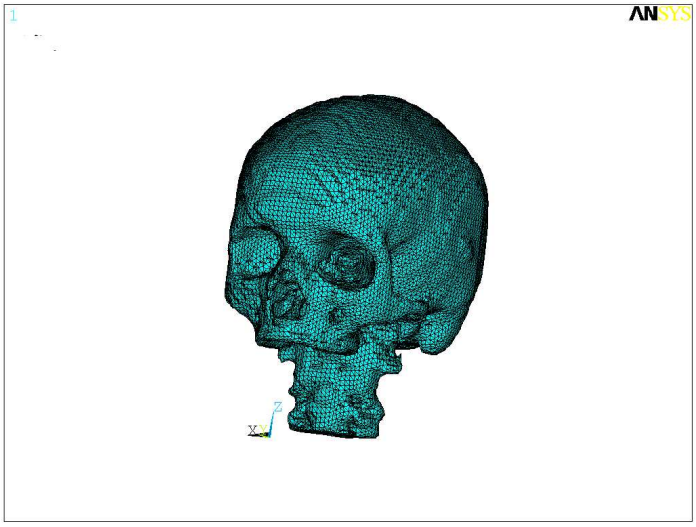

Figure 7.1 Preliminary human skull model generated using AMIRA.

Therefore, to improve the computational accuracy, an advanced ANSYS version with higher limits on the number of nodes and elements is required.

In order to understand better the physical requirements to conduct finite-element analysis on 3D human head in ANSYS, the computational cost is estimated on a simple spherical head FEA models (Figure 7.2) at different incident frequencies with different parameters in Table 7.1. The initiate plane wave location is at least 0.5λ away from the head, where λ is the acoustic wavelength in air. The distance $r - a$ (distance between the head and the absorbing boundary) is at least 1λ. For purposes of estimating computational costs, the radius of the head a is fixed at 9 cm; there are two cases (A1 and A2; see Table 7.1), however, for which the head is not included in the computational domain. Linear tetrahedral elements are used in all the models. All the estimations are conducted on NCSAs IBM p690 computer system using a single processor on a time-shared basis with other users. The p690 system has eleven 32-processor nodes available for batch jobs with processor speed of 1.3 GHz, 7 nodes with 64 GB memory and 4 nodes with 256 GB memory. The current memory limit for a single ANSYS batch job is 8 GB.

As shown in Table 7.1, the element and node limits of the current ANSYS version are easily exceeded for all the models with $\lambda/20$ requirements. In the future work,

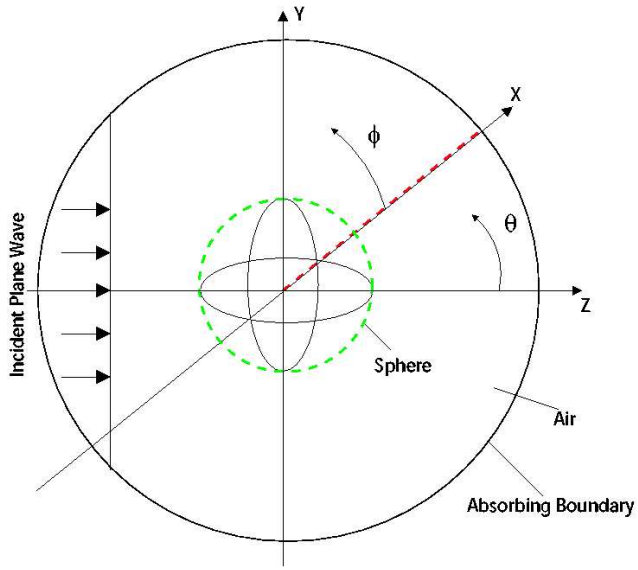

Figure 7.2 The schematic drawing of a simple 3D spherical head model

Table 7.1 Computational cost estimates

Case	f (kHz)	T (ms)	λ (cm)	a (cm)	$r-a$ (λ)	Elem. size in air (λ)	# of elems (10^3)	# of nodes (10^3)	Comp. time (T)	Memory (GB)	CPU time (hr)
A1	3	0.33	11	0	2	1/10	$\sim$ 100	$\sim$20	1	$\sim$0.8	$\sim$4
A2	3	0.33	11	0	2	1/20	$\sim$800	$\sim$160	1	$\sim$6.4	$\sim$32
B1	3	0.33	11	9	1	1/10	$\sim$120	$\sim$60	1	$\sim$ 1	$\sim$5
B2	3	0.33	11	9	1	1/20	$\sim$640	$\sim$150	1	$\sim$5	$\sim$25
C	10	0.1	3.4	9	2.5	1/20	$\sim$6000	$\sim$1200	1	$\sim$60	$\sim$300
D	6	0.17	5.7	9	1.5	1/20	$\sim$3000	$\sim$600	1	$\sim$30	$\sim$150
E	1	0.1	34	9	1	1/20	$\sim$600	$\sim$120	1	$\sim$4	$\sim$20
F	0.1	10	3.4 m	9	2	1/20	$\sim$800	$\sim$140	1	$\sim$ 6	$\sim$30
G	0.01	100	34 m	9	2	1/20	$\sim$1200	$\sim$200	1	$\sim$10	$\sim$50

even larger models with larger computational cost are expected for the following reasons. (1) Mesh sizes of $\lambda/20$ should be regarded as minimally necessary rather than a sufficient condition. If a finer mesh size like $\lambda/400$ is required, then the numbers of elements and nodes would increase at least by 23 times for frequencies less than about 1 kHz and more than 8 times for higher frequencies. (2) When more spatial details, such as skull, soft tissue, the ear, etc., are included in the head, a finer mesh and thus more elements and nodes will be needed for the head region. For

example, the skull has varying thickness, and thus a mesh size of 1 cm will be not fine enough for the thinnest temporal region. Furthermore, higher-order elements will be used to provide more accurate modeling of components with complicated shape, which will increase the numbers of nodes. Approximately $O(10^6)$ elements and nodes or possibly more will be needed for the human head region only. (3) The computation time will be longer than 1 T, which is used in the Table 1 estimates. Approximately, elements and nodes of up to $O(10^8)$, memory of up to $O(10^2)$ in GB, and CPU time of up to $O(10^3)$ in hours are expected in the future research.

Therefore, an ANSYS license with unlimited elements and nodes is necessary for the future research on a more detailed head. The parallel processing capability is also useful for the very high and very low frequency cases.

7.2.3 Computer visualization of the simulation results

Computer visualization is a very important task to interpret and comprehend the complex wave propagation around and into the human head. In this project, pressure/intensity-time waveforms have been a main method for visualization in both 2D scenario and 3D scenario, and contour plots and animation movies made in ANSYS are also used for visualization in 2D scenario. Furthermore, the propagation path evaluation was developed mainly for 3D visualizations. However, the path evaluation methodology still needs a lot of improvement and further application in the human head case. The possible reasons causing the problems were analyzed in Section 6.5.

In the future, unlimited license of ANSYS is needed to improve the computation accuracy. In the ray tracing process, element data could be included to evaluate the acoustic wave propagation paths in addition to the nodal solutions. Wavefront contours can be determined by linear interpolation within each element from the nodal values, which are averaged at a node whenever two or more elements connect to the same node. By including the element connectivity information, hopefully the discontinuity between adjacent elements can be minimized, and thereby improve the wavefront reconstruction and ray tracing. In addition, the importance of the time-step size and element size for ray tracing has not been fully evaluated and improvements are possible through careful choice of these parameters.

It is suggested that the improved ray tracing method should first be tested using planar surfaces as a function of incident angle, which is a well-studied phenomenon,

and then be further applied to hemisphere cases, and ultimately to the human head study.

7.2.4 Validation of the FEA model

In the future, there are two possible way to validate the developed 3D human head FEA model.

First, there is ample literature on the vibration characteristics of the head [37–39], and the ANSYS analysis can determine the vibration characteristics of the head model. It is reasonable to assure that the model matches the literature structurally.

Second, various subject testings are feasible through cautious experimental design. The REAT (real-ear attenuation at threshold) tests can be used to establish a bone conduction threshold for subjects, and ABR (auditory brainstem recording) tests can be used to relate force levels at various skull locations subjects to bone conduction. The FEA model can be used to predict intensity levels for air conducted sound in a sound field that produced by applying point force levels at specific skull locations to elicit ABR bone conduction responses. Then, a bone oscillator will be used to replicate the force and elicit the ABR, which can then be related to sound pressure level (SPL).

When disagreements between the FEA results and the experimental data, improvements could be made at the following areas: (1) enhance the spatial and temporal resolution of the FEA model to improve the computational accuracy; (2) update the FEA model to maximally match the real subject test environment by eliminating some of the initial assumptions, for example, including the nonlinearities into the model; and (3) modify subject test procedure correspondingly if it reaches the limits for the FEA model to match subject test environment.

REFERENCES

[1] L. E. Kinsler, A. R. Frey, A. B. Coppens, and J. V. Sanders, *Fundamentals of Acoustics.* New York: John Wiley & Sons, Inc., 2000.

[2] National Institute on Deafness and other Communication Disorders (NIDCD), "Noise-induced hearing loss," September 2002, http://www.nidcd.nih.gov /health/hearing/noise.asp.

[3] C. M. Harris, *Handbook of Acoustical Measurements and Noise Control*, 3rd ed. New York: McGraw-Hill, 1991.

[4] E. H. Berger and J. G. Casali, *Encyclopedia of Acoustics.* New York: John Wiley & Sons, Inc., 1997.

[5] S. M. Kuo and D. R. Morgan, "Active noise control: a tutorial review," *Proceedings of the IEEE*, vol. 87, pp. 943–973, 1999.

[6] D. Gauger, "Active noise reduction (anr) and hearing protection: where it's appropriate and why," *Spectrum Suppl.*, vol. 1, 2002.

[7] E. H. Berger, "Hearing protector performance: How they work and what goes wrong in the real world," Aearo Company, Tech. Rep., 1996.

[8] I. Kirikae, "An experimental study on the fundamental mechanism of bone conduction," *Acta Otolaryngol. Suppl.*, vol. 145, pp. 1–111, 1959.

[9] J. Tonndorf, "Bone conduction: Studies in experimental animals," *Acta Otolaryngol. Stockh.*, vol. 213, pp. 1–132, 1966.

[10] E. G. Wever and M. Lawrence, *Physiological Acoustics.* Princeton, N.J: Princeton University Press, 1954.

[11] J. Tonndorf, "New concept of bone conduction," *Acta Otolaryngol.*, vol. 87, p. 595, 1968.

[12] H. Sohmer and S. Freeman, "Bone conduction experiments in humans - a fluid pathway from bone to ear," *Hearing Research*, vol. 146, pp. 81–88, 2000.

[13] S. Freeman, J. Y. Sichel, and H. Sohmer, "Bone conduction experiments in animals - evidence for a non-osseous mechanism," *Hearing Research*, vol. 146, pp. 72–80, 2000.

[14] H. Sohmer and S. Freeman, "Further evidence for a fluid pathway during bone conduction auditory stimulation," *Hearing Research*, vol. 193, pp. 105–110, 2004.

[15] S. M. Khanna, J. Tonndorf, and J. Queller, "Mechanical parameters of hearing by bone conduction," *The Journal of the Acoustical Society of America*, vol. 60, pp. 139–154, 1976.

[16] S. Stenfelt and N. Hato, "Round window membrane motion with air conduction and bone conduction stimulation," *Hearing Research*, vol. 198, pp. 10–24, 2004.

[17] J. Zwislocki, "In search of the bone-conduction threshold in a free sound field," *The Journal of the Acoustical Society of America*, vol. 29, pp. 795–804, 1957.

[18] *ANSYS 6.1 Online Help*, ANSYS Inc., Canonsburg, PA, 2002, http://www1.ansys.com/customer/content/documentation.

[19] J. Jin, *The Finite Element Method in Electromagnetics.* New York: John Wiley & Sons, 2002.

[20] O. C. Zienkiewicz and R. E. Newton, "Coupled vibrations of a structure submerged in a compressible fluid," in *Proceedings of the Symposium on Finite Element Techniques*, University of Stuttgart, Germany, 1969.

[21] L. Rayleigh, *The Theory of Sound.* New York: Dover Publications, 1945.

[22] P. M. Morse and K. U. Ingard, *Theoretical Acoustics.* Boca Raton, FL: CRC Press, 1968.

[23] J. J. Faran, "Sound scattering by solid cylinder and spheres," *The Journal of the Acoustical Society of America*, vol. 23, pp. 405–418, July 1951.

[24] R. Hickling, "Analysis of echoes from a solid elastic sphere in water," *The Journal of the Acoustical Society of America*, vol. 34, pp. 1582–1592, October 1962.

[25] D. H. Johnson, R. B. Englund, B. C. McAnlis, K. C. Sari, and D. Colombet, "Three-dimensional modeling of a bolted connection," Penn State-Erie, Erie, PA, Tech. Rep., 2000.

[26] A. A. H. J. Sauren and M. H. A. Classens, "Finite element modeling of head impact: The second decade," in *Proceedings of the International IRCOBI, Conference on Biomechanics of Impact*, 1993, pp. 241–254.

[27] K. J. Bathe, *Finite Element Procedures in Engineering Analysis.* Englewood Cliff: Prentice-Hall, 1982.

[28] S. A. Goss, R. L. Johnston, and F. Dunn, "Comprehensive compilation of empirical ultrasonic properties of mammalian tissues," *The Journal of the Acoustical Society of America*, vol. 64, pp. 423–457, 1978.

[29] S. A. Goss, R. L. Johnston, and F. Dunn, "Compilation of empirical ultrasonic properties of mammalian tissues - II," *The Journal of the Acoustical Society of America*, vol. 68, pp. 93–108, 1980.

[30] F. A. Duck, *Physical Properties of Tissues: A Comprehensive Reference Book*. New York: Academic Press, 1990.

[31] R. Hickling, "Computer visualization of the scattering of sound by structures in water," *Acoustic Physics*, vol. 40, pp. 453–454, 1994.

[32] W. G. Neubauer and L. R. Dragonette, "A Schlieren system used for making movies of sound waves," *The Journal of the Acoustical Society of America*, vol. 48, pp. 1135–1149, 1970.

[33] V. W. Sparrow and D. A. Russell, "Animations created in Mathematica for acoustic education," *The Journal of the Acoustical Society of America*, vol. 103, p. 2987, 1998.

[34] C. Feuillade, "Animations for visualizing and teaching acoustic impulse scattering from spheres," *The Journal of the Acoustical Society of America*, vol. 115, pp. 1893–1904, May 2004.

[35] A. D. Pierce, *Acoustics: An Introduction to its Physical Principles and Applications.* New York: McGraw-Hill, 1981.

[36] W. D. O'Brien and Y. Liu, "Evaluation of acoustic propagation paths into the human head," presented at NATO sponsored Human Factors & Medicine Panel Symposium, Amersfoort, The Netherlands, 2005.

[37] E. H. J. F. Boezeman and A. W. Bronkhorst, "Phase relationship between bone and air conducted impulse signals in the human head," *The Journal of the Acoustical Society of America*, vol. 76, pp. 111–115, July 1984.

[38] B. Hakansson, A. Brandt, and P. Carisson, "Resonance frequencies of the human skull in vivo," *The Journal of the Acoustical Society of America*, vol. 95, pp. 1474–1481, March 1994.

[39] S. Stenfelt and T. Wild, "Vibration characteristics of bone conducted sound in vitro," *The Journal of the Acoustical Society of America*, vol. 107, pp. 422–431, 2000.